

Electromagnetic Wave Sensing in Complex Scenarios: Scattering Models and Applications

Lead Guest Editor: Pasquale Imperatore

Guest Editors: Antonio Iodice, Matteo Pastorino, and Nicolas Pinel



Electromagnetic Wave Sensing in Complex Scenarios: Scattering Models and Applications

International Journal of Antennas and Propagation

Electromagnetic Wave Sensing in Complex Scenarios: Scattering Models and Applications

Lead Guest Editor: Pasquale Imperatore

Guest Editors: Antonio Iodice and Matteo Pastorino



Copyright © 2018 Hindawi. All rights reserved.

This is a special issue published in "International Journal of Antennas and Propagation." All articles are open access articles distributed under the Creative Commons Attribution License, which permits unrestricted use, distribution, and reproduction in any medium, provided the original work is properly cited.

Editorial Board

Ana Alejos, Spain	Giuseppe Di Massa, Italy	Giuseppina Monti, Italy
Mohammod Ali, USA	Michele D'Urso, Italy	Giorgio Montisci, Italy
Jaume Anguera, Spain	Francisco Falcone, Spain	N. Nasimuddin, Singapore
Rodolfo Araneo, Italy	Miguel Ferrando Bataller, Spain	Mourad Nedil, Canada
Alexei Ashikhmin, USA	Flaminio Ferrara, Italy	Symeon Nikolaou, Cyprus
Herve Aubert, France	Vincenzo Galdi, Italy	Giacomo Oliveri, Italy
Paolo Baccarelli, Italy	Claudio Gennarelli, Italy	Ikmo Park, Republic of Korea
Xiulong Bao, Ireland	Farid Ghanem, Algeria	Josep Parrón, Spain
Toni Björninen, Finland	Sotirios K. Goudos, Greece	Matteo Pastorino, Italy
Stefania Bonafoni, Italy	Rocco Guerriero, Italy	Xianming Qing, Singapore
Paolo Burghignoli, Italy	Kerim Guney, Turkey	Ahmad Safaai-Jazi, USA
Shah Nawaz Burokur, France	Song Guo, Japan	Safieddin Safavi-Naeini, Canada
Giuseppe Castaldi, Italy	Tamer S. Ibrahim, USA	Magdalena Salazar-Palma, Spain
Luca Catarinucci, Italy	M. Ramlee Kamarudin, UK	Stefano Selleri, Italy
Felipe Cátedra, Spain	Slawomir Koziel, Iceland	Raffaele Solimene, Italy
Marta Cavagnaro, Italy	Luis Landesa, Spain	Gino Sorbello, Italy
Shih Yuan Chen, Taiwan	Ding-Bing Lin, Taiwan	Seong-Youp Suh, USA
Yu Jian Cheng, China	Angelo Liseno, Italy	Sheng Sun, Hong Kong
Renato Cicchetti, Italy	Pierfrancesco Lombardo, Italy	Larbi Talbi, Canada
Riccardo Colella, Italy	Lorenzo Luini, Italy	Luciano Tarricone, Italy
Laura Corchia, Italy	Atsushi Mase, Japan	Parveen Wahid, USA
Lorenzo Crocco, Italy	Diego Masotti, Italy	Chien-Jen Wang, Taiwan
Claudio Curcio, Italy	Ch. F. Mecklenbräuker, Austria	Wen-Qin Wang, China
Francesco D'Agostino, Italy	A. Toaha Mobashsher, Australia	Mustapha C E Yagoub, Canada
María Elena de Cos Gómez, Spain	Ananda S. Mohan, Australia	Shiwen Yang, China
Tayeb A. Denidni, Canada	J.-M. Molina-Garcia-Pardo, Spain	Yuan Yao, China

Contents

Electromagnetic Wave Sensing in Complex Scenarios: Scattering Models and Applications

Pasquale Imperatore , Antonio Iodice, Matteo Pastorino , and Nicolas Pinel
Volume 2018, Article ID 4616571, 2 pages

Replacement of Ensemble Averaging by the Use of a Broadband Source in Scattering of Light from a One-Dimensional Randomly Rough Interface between Two Dielectric Media

Alexei A. Maradudin and Ingve Simonsen 
Volume 2018, Article ID 6768306, 7 pages

Modelling Scattering of Electromagnetic Waves in Layered Media: An Up-to-Date Perspective

Pasquale Imperatore, Antonio Iodice, Matteo Pastorino, and Nicolas Pinel
Volume 2017, Article ID 7513239, 14 pages

Application of a Sparsity Pattern and Region Clustering for Near Field Sparse Approximate Inverse Preconditioners in Method of Moments Simulations

Carlos Delgado, Javier Moreno, and Felipe Cátedra
Volume 2017, Article ID 9845050, 8 pages

Electromagnetic Scattering of Electrically Large Ship above Sea Surface with SBR-SDFM Method

Lixin Guo and Tiantian Feng
Volume 2017, Article ID 2753794, 6 pages

Research on Spatial Channel Model for Vehicle-to-Vehicle Communication Channel in Roadside Scattering Environment

Xin Chen, Yong Fang, Weidong Xiang, and Liang Zhou
Volume 2017, Article ID 3098198, 12 pages

An Efficient Hybrid Method for 3D Scattering from Inhomogeneous Object Buried beneath a Dielectric Randomly Rough Surface

Hong-jie He, Li-xin Guo, and Wei Liu
Volume 2017, Article ID 2847094, 8 pages

Modeling and Characterization of the Uplink and Downlink Exposure in Wireless Networks

Anis Krayni, Abdelhamid Hadjem, Günter Vermeeren, Alain Sibille, Christophe Roblin, Wout Joseph, Luc Martens, and Joe Wiart
Volume 2017, Article ID 8243490, 15 pages

Editorial

Electromagnetic Wave Sensing in Complex Scenarios: Scattering Models and Applications

Pasquale Imperatore^{ID},¹ Antonio Iodice,² Matteo Pastorino^{ID},³ and Nicolas Pinel⁴

¹*Institute for Electromagnetic Sensing of the Environment (IREA), National Research Council (CNR), Napoli, Italy*

²*Department of Electrical Engineering and Information Technology, University of Naples Federico II, Napoli, Italy*

³*Department of Electrical, Electronic, Telecommunications Engineering and Naval Architecture (DITEN), University of Genoa, Genova, Italy*

⁴*Icam School of Engineering-Nantes Campus, Carquefou, France*

Correspondence should be addressed to Pasquale Imperatore; imperatore.p@irea.cnr.it

Received 23 October 2017; Accepted 24 October 2017; Published 11 February 2018

Copyright © 2018 Pasquale Imperatore et al. This is an open access article distributed under the Creative Commons Attribution License, which permits unrestricted use, distribution, and reproduction in any medium, provided the original work is properly cited.

Recent progress in wave sensing techniques and technologies has resulted in the development of applications in disparate fields, including radar imaging, remote sensing, and communication. Within this context, electromagnetic modeling plays an important role, since scattering models have explicitly or implicitly been used in wave sensing applications or integrated within the inherent signal processing schemes. Scattering models, as abstractions of the real world given in terms of computable mathematical functions, are effective according to their predictive capabilities in describing the wave interaction phenomenon under investigation. Depending on the adopted methodological approach, scattering models may be analytical or numerical, continuous or discrete, and either deterministic or stochastic, with some of them being more appropriate, in terms of accuracy and computational cost, for a specific application scenario. Scattering modeling, pertaining to either man-made or natural complex structures or environments, extends to the vast field of practical sensing applications, thus still posing challenging problems of theoretical, computational, and experimental relevance.

This special issue reports contribution to the research in the area of electromagnetic wave sensing, thus describing recent advancements, developments, and applications, with a special emphasis on the scattering modeling in complex scenarios.

The technical contributions in the accepted papers range from theoretical to numerical modeling, with application to remote sensing, optics, and wireless communications.

The paper titled “Replacement of Ensemble Averaging by the Use of a Broadband Source in Scattering of Light from a One-Dimensional Randomly Rough Interface between Two Dielectric Media”, by A.A. Maradudin and I. Simonsen, presents a theoretical investigation based on phase perturbation theory. Specifically, authors demonstrate that illuminating one realization of a rough interface by a broadband Gaussian beam produces an intensity profile of the scattered field that closely matches the one produced by averaging the intensity of the scattered field, produced by a monochromatic incident beam, over the ensemble of realizations of the random surface profile function.

A review of methodologies for the EM scattering in layered media has been presented in the paper titled “Modelling Scattering of Electromagnetic Waves in Layered Media: An Up-to-date Perspective” by P. Imperatore et al., thus covering the recent progress achieved with different approaches.

The goal of the paper titled “An Efficient Hybrid Method for 3D Scattering from Inhomogeneous Object Buried beneath a Dielectric Randomly Rough Surface” by H. He et al. is to develop an iterative analytical-numerical method. The proposed strategy encompasses both Kirchhoff

approximation (KA) and finite element method (FEM) combined with the boundary integral method (BIM).

The paper titled “Application of a Sparsity Pattern and Region Clustering for Near Field Sparse Approximate Inverse Preconditioners in Method of Moments Simulations” by C. Delgado et al. presents an improved preconditioning approach for method of moments (MoM) problems using multiple regions. More precisely, it presents a technique for the generation of sparse inverse preconditioners based on the near-field coupling matrices of MoM simulations, where the geometry has been partitioned in terms of regions.

A maritime application is considered in the paper by L. Guo and T. Feng, “Electromagnetic Scattering of Electrically Large Ship above Sea Surface with SBR-SDFM Method”. In particular, a hybrid method is proposed for predicting the electromagnetic scattering by electrically large ships above the sea surface.

The paper titled “Modeling and Characterization of the Uplink and Downlink Exposure in Wireless Networks”, by A. Krayni et al., combines FDTD simulations, a simplified propagation model and measurements to evaluate both global and local radio wave exposure induced by a wireless network.

A roadside scattering environment is considered by X. Chen et al. in the paper entitled “Research on Spatial Channel Model for Vehicle-to-Vehicle Communication Channel in Roadside Scattering Environment”. Impact on vehicle speed, traffic density, and other statistical performances of the proposed vehicle-to-vehicle communication channel is discussed.

We would like to thank all the authors for their important contributions, and all the anonymous reviewers who helped improve the quality of the published papers.

*Pasquale Imperatore
Antonio Iodice
Matteo Pastorino
Nicolas Pinel*

Research Article

Replacement of Ensemble Averaging by the Use of a Broadband Source in Scattering of Light from a One-Dimensional Randomly Rough Interface between Two Dielectric Media

Alexei A. Maradudin¹ and Ingve Simonsen^{2,3} 

¹Department of Physics and Astronomy, University of California, Irvine, CA 92697, USA

²Surface du Verre et Interfaces, UMR 125 CNRS/Saint-Gobain, 93303 Aubervilliers, France

³Department of Physics, NTNU—Norwegian University of Science and Technology, NO-7491 Trondheim, Norway

Correspondence should be addressed to Ingve Simonsen; ingve.simonsen@ntnu.no

Received 11 July 2017; Accepted 8 October 2017; Published 21 January 2018

Academic Editor: Pasquale Imperatore

Copyright © 2018 Alexei A. Maradudin and Ingve Simonsen. This is an open access article distributed under the Creative Commons Attribution License, which permits unrestricted use, distribution, and reproduction in any medium, provided the original work is properly cited.

By the use of phase perturbation theory we show that if a single realization of a one-dimensional randomly rough interface between two dielectric media is illuminated at normal incidence from either medium by a broadband Gaussian beam, it produces a scattered field whose differential reflection coefficient closely matches the result produced by averaging the differential reflection coefficient produced by a monochromatic incident beam over the ensemble of realizations of the interface profile function.

1. Introduction

In theoretical calculations of some property of monochromatic light scattered from, or transmitted through, a randomly rough surface, such as the angular or spatial dependence of its intensity, what is actually calculated is the average of that property over the ensemble of realizations of the random surface profile. This procedure averages over the speckles that would be produced if monochromatic light were scattered by or transmitted through a single realization of the random surface and produces a smooth angular or spatial dependence of the property of interest.

In an experiment, this property is measured for a single realization of the random surface. If the surface is illuminated by a monochromatic source, the resulting speckles have to be averaged in some way to produce the kind of smooth curve that ensemble averaging yields. This can be done by rotating or dithering the sample. However, in some cases, moving the surface is not an option. In such cases, one can exploit the fact that the speckle pattern depends on the wavelength of the incident light [1] to average over the speckles by using a broadband (polychromatic) beam to illuminate the surface instead of a monochromatic one. In an earlier paper [2], it

was demonstrated that illuminating one realization of a one-dimensional randomly rough perfectly conducting surface by an s-polarized broadband Gaussian beam produced an intensity profile of the scattered field that closely matched the one produced by averaging the intensity of the scattered field produced by a monochromatic incident beam over the ensemble of realizations of the random surface profile function.

In this paper, we explore the replacement of ensemble averaging by the use of an incident broadband Gaussian beam in the more realistic case where the one-dimensional rough interface between two dielectric media is illuminated at normal incidence from either medium and the differential reflection coefficient of the scattered light is sought.

2. Scattering Theory

The system we study consists of a dielectric medium whose dielectric constant is ϵ_1 in the region $x_3 > \zeta(x_1)$ and a dielectric medium whose dielectric constant is ϵ_2 in the region $x_3 < \zeta(x_1)$ (Figure 1). Both ϵ_1 and ϵ_2 are assumed to be real, positive, and frequency independent. The interface profile function $\zeta(x_1)$ is assumed to be a single-valued function of

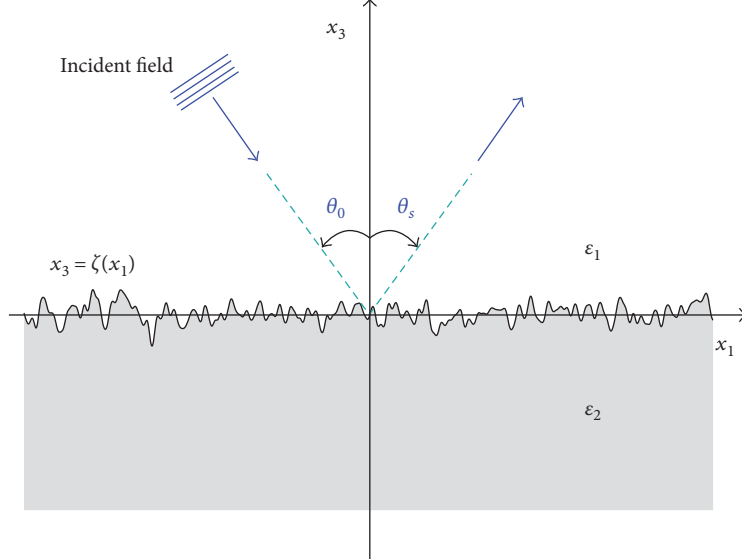


FIGURE 1: Schematics of the scattering geometry.

x_1 that is differentiable and constitutes a random process. This interface is illuminated at normal incidence from the region $x_3 > \zeta(x_1)$ by a p- or s-polarized broadband Gaussian beam of light of angular frequency ω , whose plane of incidence is the x_1x_3 plane. The single nonzero component of its electromagnetic field is a weighted superposition of incoming plane waves,

$$F_v(x_1, x_3; t)_{\text{inc}} = \int_{-\infty}^{\infty} \frac{d\omega}{2\pi} \int_{-\sqrt{\epsilon_1}\omega}^{\sqrt{\epsilon_1}\omega} \frac{dk}{2\pi} W(k, \omega) \exp[ikx_1 - i\alpha_1(k, \omega)x_3 - i\omega t], \quad (1)$$

where $F_v(x_1, x_3; t)_{\text{inc}}$ is $H_2(x_1, x_3; t)_{\text{inc}}$ when $v=p$ and is $E_2(x_1, x_3; t)$ when $v=s$. The function $\alpha_1(k, \omega)$ is defined by $\alpha_1(k, \omega) = [\epsilon_1(\omega/c)^2 - k^2]^{1/2}$ with $\text{Re}\alpha_1(k, \omega) > 0$ and $\text{Im}\alpha_1(k, \omega) > 0$, where c is the speed of light in vacuum. The weight function $W(k, \omega)$ has the factored form

$$W(k, \omega) = G(k) F(\omega), \quad (2)$$

where

$$G(k) = \frac{2\sqrt{\pi}}{\alpha_1(k, \omega)} \sqrt{\epsilon_1} \frac{w\omega}{2c} \exp\left[-\left(\sqrt{\epsilon_1} \frac{w\omega}{2c}\right)^2 \arcsin^2\left(\frac{kc}{\sqrt{\epsilon_1}\omega}\right)\right], \quad (3)$$

while $F(\omega)$ is a random function that possesses the properties

$$\begin{aligned} \langle F(\omega) F^*(\omega') \rangle_F &= 2\pi\delta(\omega - \omega') S_0(\omega), \\ \langle F(\omega) F(\omega') \rangle_F &= 0. \end{aligned} \quad (4)$$

The angle brackets $\langle \dots \rangle_F$ here denote an average over the ensemble of realizations of the field [3]. An incident field of this nature is produced by a superluminescent diode [4], for

example. We assume that the spectral density of the incident field $S_0(\omega)$ has a Gaussian form with a central frequency ω_0 and a $1/e$ halfwidth $\Delta\omega$,

$$S_0(\omega) = \frac{1}{\sqrt{\pi}\Delta\omega} \exp\left[-\left(\frac{\omega - \omega_0}{\Delta\omega}\right)^2\right]. \quad (5)$$

In the following, it will be assumed that the halfwidth is small enough that the spectral density of the incident light can be regarded as zero when $\omega < 0$. Moreover, for convenience, the function $F(\omega)$ will be regarded as zero when $\omega < 0$.

In the limit that $\sqrt{\epsilon_1}w\omega/2c \gg 1$, that will be assumed here, (1) represents a Gaussian beam of $1/e$ halfwidth w that is incident normally on the rough interface. To see this, one will make the change of variable $k = \sqrt{\epsilon_1}(\omega/c)\sin\theta$ in (1) which results in a Gaussian integral on the right-hand side of this equation that is evaluated analytically to produce

$$F_v(x_1, x_3; t)_{\text{inc}} = \int_{-\infty}^{\infty} \frac{d\omega}{2\pi} F(\omega) \exp\left[-\left(\frac{x_1}{w}\right)^2 - i\sqrt{\epsilon_1} \frac{\omega}{c} x_3 - i\omega t\right]. \quad (6)$$

Due to the linearity of the scattering problem, the scattered field can be written as

$$\begin{aligned} F_v(x_1, x_3; t)_{sc} &= \int_{-\infty}^{\infty} \frac{d\omega}{2\pi} F(\omega) \int_{-\sqrt{\epsilon_1}\omega}^{\sqrt{\epsilon_1}\omega} \frac{dk}{2\pi} G(k) \\ &\quad \cdot \int_{-\infty}^{\infty} \frac{dq}{2\pi} R_v(q|k) \exp[iqx_1 + i\alpha_1(q, \omega)x_3 - iq\omega t], \end{aligned} \quad (7)$$

where $R_v(q|k)$ is the scattering amplitude that is obtained when the incident field is given by $\exp[ikx_1 - i\alpha_1(k, \omega)x_3 - i\omega t]$ or

$$\begin{aligned} F_v(r, \theta_s; t)_{sc} &= \int_{-\infty}^{\infty} \frac{d\omega}{2\pi} F(\omega) \int_{-\sqrt{\varepsilon_1} \frac{\omega}{c}}^{\sqrt{\varepsilon_1} \frac{\omega}{c}} \frac{dk}{2\pi} G(k) \\ &\cdot \int_{-\infty}^{\infty} \frac{dq}{2\pi} R_v(q|k) \exp[iqr \sin \theta_s + ia_1(q, \omega)r \cos \theta_s - iwt], \end{aligned} \quad (8)$$

where $r = \sqrt{x_1^2 + x_3^2}$ and $x_1 = r \sin \theta_s$, $x_3 = r \cos \theta_s$. It can be calculated by any of the several approaches such as small amplitude perturbation theory [5], the Kirchhoff approximation [6], phase-perturbation theory [7], and by rigorous numerical solutions of the equations of scattering theory [8]. We will use here the first-order phase perturbation theory expression for $R_v(q|k)$, due to its simplicity and because it interpolates between small-amplitude perturbation theory and the Kirchhoff approximation.

In small-amplitude perturbation theory, the expression obtained for $R_v(q|k)$ to the lowest nonzero order in the interface profile function $\zeta(x_1)$ is

$$R_v(q|k) = R_v(k) \left[2\pi\delta(q-k) + i\Phi_v(q|k)\hat{\zeta}(q-k) + \dots \right], \quad (9)$$

where

$$\hat{\zeta}(Q) = \int_{-\infty}^{\infty} dx_1 \zeta(x_1) \exp(-iQx_1), \quad (10)$$

while

$$\begin{aligned} R_p(k) &= \frac{\varepsilon_2 \alpha_1(k, \omega) - \varepsilon_1 \alpha_2(k, \omega)}{\varepsilon_2 \alpha_1(k, \omega) + \varepsilon_1 \alpha_2(k, \omega)}, \\ \Phi_p(q|k) &= \frac{\varepsilon_2 - \varepsilon_1}{\varepsilon_2 \alpha_1(q, \omega) + \varepsilon_1 \alpha_2(q, \omega)} [\varepsilon_2 q k - \varepsilon_1 \alpha_2(q, \omega) \alpha_2(k, \omega)] \\ &\cdot \frac{2\alpha_1(k, \omega)}{\varepsilon_2 a_1(k, \omega) - \varepsilon_1 \alpha_2(k, \omega)}, \end{aligned} \quad (11)$$

and

$$\begin{aligned} R_s(k) &= \frac{\alpha_1(k, \omega) - \alpha_2(k, \omega)}{\alpha_1(k, \omega) + \alpha_2(k, \omega)}, \\ \Phi_s(q|k) &= [\alpha_2(q, \omega) - \alpha_1(q, \omega)] \frac{2\alpha_1(k, \omega)}{\alpha_1(k, \omega) - \alpha_2(k, \omega)}, \end{aligned} \quad (12)$$

with $\alpha_2(k, \omega) = [\varepsilon_2(\omega/c)^2 - k^2]^{1/2}$, $\text{Re } \alpha_2(k, \omega) > 0$, and $\text{Im } \alpha_2(k, \omega) > 0$. We can rewrite the right-hand side of (9) as a Fourier integral,

$$\begin{aligned} R_v(q|k) &= R_v(k) \int_{-\infty}^{\infty} dx_1 \exp[-i(q-k)x_1] [1 + i\Phi_v(q|k)\zeta(x_1) + \dots]. \end{aligned} \quad (13)$$

On exponentiating the expression in brackets in the integrand in this expression, we obtain the first-order phase perturbation theory expression for $R_v(q|k)$,

$$R_v(q|k) = R_v(k) \int_{-\infty}^{\infty} dx_1 \exp[-i(q-k)x_1] \exp[i\Phi_v(q|k)\zeta(x_1)]. \quad (14)$$

We will use this expression here due to its simplicity. After interchanging the order of the k and q integrations in (7), it follows that the scattering amplitude for a Gaussian monochromatic beam of frequency ω can be expressed as

$$R_v(q, \omega) = \int_{-\sqrt{\varepsilon_1} \frac{\omega}{c}}^{\sqrt{\varepsilon_1} \frac{\omega}{c}} \frac{dk}{2\pi} R_v(q|k) G(k), \quad (15)$$

so that the scattered field becomes

$$\begin{aligned} F_v(x_1, x_3; t)_{sc} &= \int_{-\infty}^{\infty} \frac{d\omega}{2\pi} F(\omega) \\ &\cdot \int_{-\infty}^{\infty} \frac{dq}{2\pi} R_v(q, \omega) \exp[iqx_1 + i\alpha_1(q, \omega)x_3 - iwt]. \end{aligned} \quad (16)$$

The scattering amplitude $R_v(q, \omega)$ enters the definition of the *differential reflection coefficient* which is defined as the fraction of the power flux incident onto the rough interface that is scattered into an angular interval of width $d\theta_s$ about the scattering angle θ_s [9]. For an illumination of the random interface by a normally incident Gaussian beam of frequency ω , the expression for the differential reflection coefficient in the wide beam limit $\sqrt{\varepsilon_1} w \omega / 2c \gg 1$ reads [8, 10]

$$\frac{\partial R_v}{\partial \theta_s}(\theta_s) = \frac{\sqrt{\varepsilon_1}}{\sqrt{2}\pi^{3/2}} \frac{\omega}{cw} \cos^2 \theta_s |R(q, \omega)|^2, \quad (17)$$

where $q = \sqrt{\varepsilon_1}(\omega/c) \sin \theta_s$. When the differential reflection coefficient from (17), for monochromatic illumination at frequency ω_0 , is averaged over an ensemble of realizations of the random interface, the *mean* differential reflection coefficient is obtained and we denote it $\langle \partial R_v / \partial \theta_s \rangle$ in the following. On the other hand, if the illumination of the random interface is done by a broadband source and characterized by the center frequency ω_0 and the halfwidth is $\Delta\omega$, the “broadband” differential reflection coefficient $\langle \partial R_v / \partial \theta_s \rangle_F$ is obtained.

We now turn to the calculation of a simple expression for the scattering amplitude $R_v(q, \omega)$. On substituting into (15), the results from (14) and (3) and making the change of variable $k = \sqrt{\varepsilon_1}(\omega/c) \sin \theta$ in the resulting expression, one gets

$$\begin{aligned} R_v(q, \omega) &= \frac{\sqrt{\varepsilon_1}}{\pi} \frac{w\omega}{2c} \int_{-\pi/2}^{\pi/2} d\theta \exp\left[-\left(\sqrt{\varepsilon_1} \frac{w\omega}{2c}\right)^2 \theta^2\right] R_v\left(\sqrt{\varepsilon_1} \frac{\omega}{c} \sin \theta\right) \\ &\times \int_{-\infty}^{\infty} dx_1 \exp\left[-iqx_1 + i\sqrt{\varepsilon_1} \frac{\omega}{c} \sin \theta x_1\right] \\ &\exp\left[i\Phi_v\left(q \sqrt{\varepsilon_1} \frac{\omega}{c} \sin \theta\right) \zeta(x_1)\right]. \end{aligned} \quad (18)$$

On passing to the limit $\sqrt{\varepsilon_1} (w\omega/2c) \gg 1$, corresponding to a wide Gaussian beam, one may take advantage of the

approximations $\sin \theta \approx 0$ and $\cos \theta \approx 1$, with the consequence that Φ_v becomes a *linear* function of the variable θ ,

$$\Phi_v\left(q|\sqrt{\varepsilon_1}\frac{\omega}{c} \sin \theta\right) \approx \phi_v^{(0)}(q, \omega) + \phi_v^{(1)}(q, \omega)\theta, \quad (19)$$

with

$$\phi_v^{(0)}(q, \omega) = \Phi_v(q|0), \quad (20)$$

and

$$\begin{aligned} \phi_p^{(1)}(q, \omega) &= 2\frac{\omega}{c}\sqrt{\varepsilon_1\varepsilon_2}(\sqrt{\varepsilon_1} + \sqrt{\varepsilon_2})\frac{q}{\varepsilon_2\alpha_1(q, \omega) + \varepsilon_1\alpha_2(q, \omega)} \\ \phi_s^{(1)}(q, \omega) &= 0. \end{aligned} \quad (21)$$

Moreover, in the limit $\sqrt{\varepsilon_1}(w\omega/2c) \gg 1$, the θ integral in (18) takes the Gaussian form, due to the results in (19)–(21) and can hence be evaluated analytically with the result that

$$\begin{aligned} R_v(q, \omega) &= R_v(0) \int_{-\infty}^{\infty} dx_1 \exp \left[- \left\{ \frac{x_1}{w} + \frac{\phi_v^{(1)}(q, \omega)\zeta(x_1)}{\sqrt{\varepsilon_1}(\omega/c)w} \right\}^2 \right. \\ &\quad \left. - iqx_1 + i\phi_v^{(0)}(q, \omega)\zeta(x_1) \right]. \end{aligned} \quad (22)$$

This is the simplified expression for the scattering amplitude derived from phase perturbation theory that we will use to produce the results to be presented later in this paper. It represents a significant simplification relative to, for instance, obtaining the scattering amplitude by rigorous means [8], which requires solving a linear system of equations that becomes time-consuming when the interface becomes long.

The interface profile function $\zeta(x_1)$ is assumed to be a single-valued function of x_1 that is differentiable and constitutes a zero-mean, stationary Gaussian random process defined by

$$\langle \zeta(x_1)\zeta(x'_1) \rangle = \delta^2 W(|x_1 - x'_1|). \quad (23)$$

The angle brackets here denote an average over the ensemble of realizations of $\zeta(x_1)$, $\delta = \langle \zeta^2(x_1) \rangle^{1/2}$ is the root mean-square height of the interface, and $W(|x_1|)$ is the normalized interface height auto-correlation function.

The power spectrum of the interface roughness, $g(|k|)$, is the Fourier transform of $W(|x_1|)$,

$$g(|k|) = \int_{-\infty}^{\infty} dx_1 W(|x_1|) \exp(-ikx_1). \quad (24)$$

In the calculations carried out in this work, $W(|x_1|)$, will be assumed to have the Gaussian form

$$W(|x_1|) = \exp\left(-\frac{x_1^2}{a^2}\right), \quad (25)$$

where the characteristic length a is the transverse correlation length if the interface roughness. The power spectrum $g(|k|)$ in this case also has the Gaussian form

$$g(|k|) = \sqrt{\pi}a \exp\left(-\frac{k^2 a^2}{4}\right). \quad (26)$$

A single realization of the interface profile function is given by [11]

$$\begin{aligned} \zeta(x_1) &= \delta \sqrt{\frac{2}{\mathcal{L}}} \sum_{m=1}^{\infty} \left[g\left(\frac{2\pi m}{L}\right) \right]^{1/2} \\ &\quad \cdot \left[\xi_{2m-1} \sin\left(\frac{2\pi mx_1}{\mathcal{L}}\right) + \xi_{2m} \cos\left(\frac{2\pi mx_1}{\mathcal{L}}\right) \right]. \end{aligned} \quad (27)$$

In this expression, the $\{\xi_m\}$ are independent Gaussian random deviates with zero mean and unit variance:

$$\langle \xi_m \rangle = 0, \quad \langle \xi_m^2 \rangle = 1. \quad (28)$$

The function defined by (27) is a periodic function of x_1 with a period \mathcal{L} . To avoid edge effects, only the portion of this function in the interval $-L/2 < x_1 < L/2$ where $L = \mathcal{L}/2$ is used in calculations.

3. Results and Discussion

In Figure 2(a), we present a plot of the speckle pattern of the scattered field as a function of the scattering angle θ_s produced by a monochromatic p-polarized Gaussian beam of frequency ω_0 , given by (6) with $F(\omega) = 2\pi\delta(\omega - \omega_0)$, incident on a single realization of a one-dimensional randomly rough interface generated with the use of (27). In Figure 2(b), we present the differential reflection coefficient of the scattered field given by (16) when the realization of the interface profile function used in obtaining Figure 2(a) is illuminated by a broadband Gaussian beam whose center frequency is ω_0 with a halfwidth $\Delta\omega = 0.2\omega_0$. To obtain this result, calculations of the differential reflection coefficient were carried out for several values of $\Delta\omega$, ranging from $0.2\omega_0$ to $0.4\omega_0$. The results did not differ in any significant way so we chose to use the smallest of these $\Delta\omega$ values. It should be remarked that when a different realization of the surface was illuminated by the same broadband beam used to produce the result in Figure 2(b), the result was essentially $\langle \partial R_p / \partial \theta_s \rangle_F$ from the same figure except for some small-amplitude fine details. Finally, in Figure 2(c), we plot the mean differential reflection coefficient $\langle \partial R_p / \partial \theta_s \rangle$ obtained by averaging the results from $N_p = 10,000$ realizations of the interface profile function generated by (27) when the interface is illuminated by the same monochromatic Gaussian beam of frequency ω_0 used in obtaining Figure 2(a). The values of the theoretical

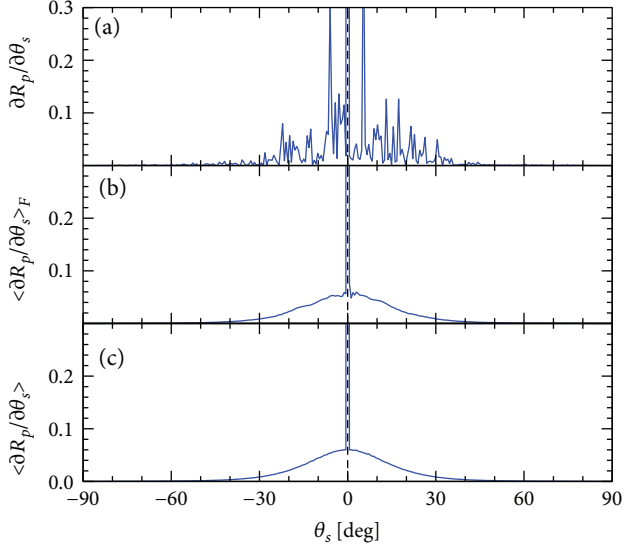


FIGURE 2: The differential reflection coefficient $\partial R_p/\partial\theta_s$ defined by (17) for a vacuum-glass system [$\varepsilon_1 = 1$ and $\varepsilon_2 = 2.25$] illuminated from the vacuum side by different p-polarized incident beams: (a) a Gaussian monochromatic beam of halfwidth w and frequency ω_0 ; (b) a *broadband* Gaussian beam of center frequency ω_0 and frequency bandwidth $\Delta\omega = 0.2\omega_0$; and (c) a monochromatic beam as in Figure 2(a) but with an average performed over an ensemble of $N_p = 10,000$ realizations of the interface profile function. The angle of incidence was $\theta_0 = 0^\circ$ and the wavelength was $\lambda_0 = 2\pi c/\omega_0 = 632.8$ nm. The randomly rough interface was characterized by the parameters $\delta = 0.15\lambda_0$, $a = 1.50\lambda_0$, and $L = 10^4\lambda_0$, and the sampling interval used to discretize the surface was $\Delta x_1 = \lambda_0/10$. For the width of the Gaussian beam, the value $w = L/4$ was used. The same random interface was used in producing the results of the first two panels of this figure.

and experimental parameters assumed in obtaining these results were $\varepsilon_1 = 1$, $\varepsilon_2 = 2.25$, $\lambda_0 = 2\pi c/\omega_0 = 632.8$ nm, and $w = L/4$ where L is the length of the surface. The parameters defining the interface roughness were $\delta = 0.15\lambda_0$, $a = 1.50\lambda_0$, and $L = 10^4\lambda_0$. The sampling interval used was $\Delta x_1 = \lambda_0/10$ so that the interface was discretized onto $N = 10^5$ points. Figure 3 presents corresponding results for s-polarized incident beams.

The results presented in Figures 2 and 3 show that the use of a broadband beam in illuminating a single realization of a one-dimensional randomly rough interface averages over the speckles produced by a monochromatic beam. It therefore produces a differential reflection coefficient that closely matches the one produced by a monochromatic beam when the resulting differential reflection coefficient is averaged over the ensemble of realizations of the interface profile function.

To facilitate the comparison of $\langle\partial R_v/\partial\theta_s\rangle_F$ and $\langle\partial R_v/\partial\theta_s\rangle$, in Figures 4(a) and 4(c), we plot simultaneously these quantities on a semilogarithmic scale. It is observed that the agreement between them is rather good even in the tails of the scattered intensity distributions.

The results presented in Figures 2 and 3 were, for convenience, all obtained under the assumption of phase

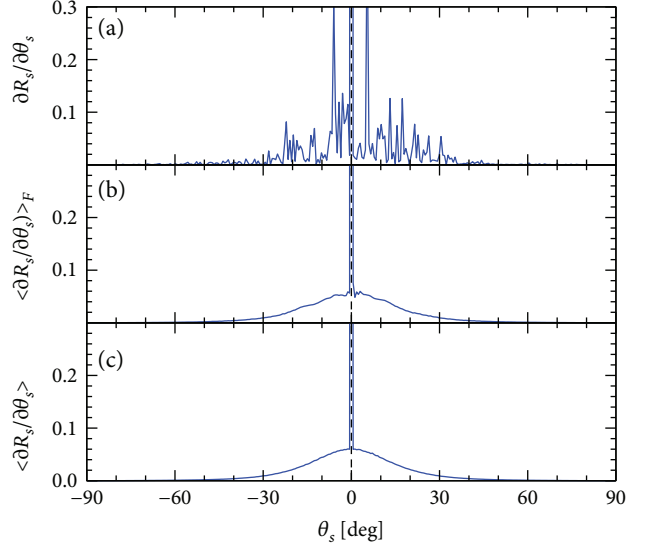


FIGURE 3: Same as Figure 2 but for s-polarized incident beams, the single realization of the rough interface used to obtain the results of the first two panels of this figure is the same one used in Figure 2.

perturbation theory. In Figure 4, we compare the mean differential reflection coefficients $\langle\partial R_v/\partial\theta_s\rangle$ from Figures 2(c) and 3(c) to rigorous computer simulation results obtained by solving the equations of scattering theory [8]. The agreement between the two sets of results is rather convincing. In passing, it should be noted that in performing the rigorous simulations the length used for the rough interface was $L' = 10^2\lambda_0$ and the width of the Gaussian beam was $L'/4$. This length of the rough interface is two orders of magnitude shorter than the length used in obtaining the results based on phase perturbation theory.

We now turn to a scattering geometry where the medium of incidence is the optically denser medium. Here, we assume a glass-vacuum system characterized by $\varepsilon_1 = 2.25$ and $\varepsilon_2 = 1$. Physically, this corresponds to the light being incident from the opposite side of the rough interface relative to the system we previously studied. The results for the differential reflection coefficients for the glass-vacuum system are presented in Figures 5, 6, and 7. In these figures, the angles for which $|\theta_s| \geq \theta_s^*$ have been indicated as shaded regions, where $\theta_s^* = \arcsin(\sqrt{\varepsilon_2/\varepsilon_1}) = 41.81^\circ$ denotes the critical angle for total internal reflection. Due to the assumptions underlying phase perturbation theory, it is expected not to work well when the angles of incidence and/or scattering in absolute value are larger than this critical angle. Hence, in Figures 5, 6, and 7, we have plotted the results obtained on the basis of phase perturbation theory only for $|\theta_s| < \theta_s^*$.

On the basis of the results presented in Figures 5, 6, and 7, it is concluded that also for systems where the medium of incidence is the optically denser medium, one finds that the differential reflection coefficients $\langle\partial R_v/\partial\theta_s\rangle_F$ and $\langle\partial R_v/\partial\theta_s\rangle$ match each other rather well in the angular interval $|\theta_s| < \theta_s^*$.

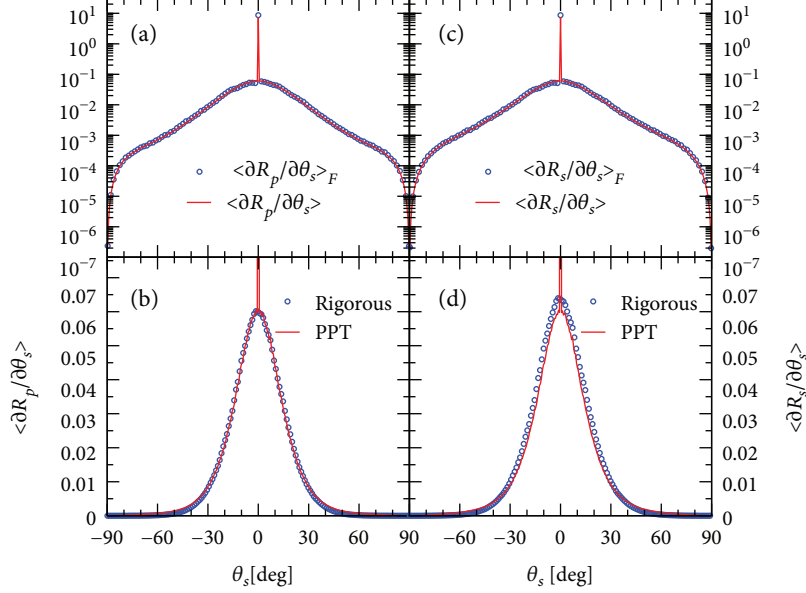


FIGURE 4: The quantities $\langle \partial R_\nu / \partial \theta_s \rangle_F$ and $\langle \partial R_\nu / \partial \theta_s \rangle$ obtained for a vacuum-glass system [$\epsilon_1 = 1$ and $\epsilon_2 = 2.25$] plotted on semilogarithmic scales for $\nu=p$ [Figure 4(a)] and $\nu=s$ [Figure 4(c)]. Comparison of the mean differential reflection coefficients $\langle \partial R_\nu / \partial \theta_s \rangle$ obtained by either a rigorous simulation approach or on the basis of phase perturbation theory (PPT) for p-polarized (Figure 4(b)) or s-polarized (Figure 4(d)) illumination. All ensemble averaged quantities were obtained on the basis of $N_p = 10,000$ realizations of the interface profile function. The remaining parameters are identical to those of Figure 2.

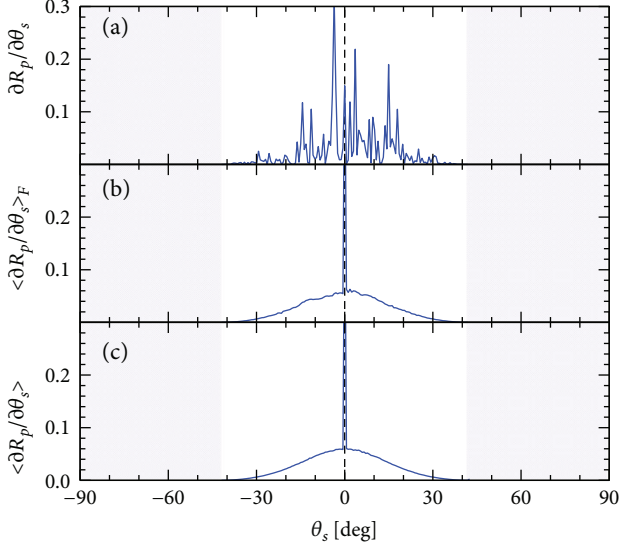


FIGURE 5: Same as Figure 2, that is, p-polarized illumination, but for a system where the medium of incidence is the optically denser medium ($\epsilon_1 = 2.25$ and $\epsilon_2 = 1$), the shaded regions correspond to $|\theta_s| \geq \theta_s^*$ where $\theta_s^* = \arcsin(\sqrt{\epsilon_2/\epsilon_1}) = 41.81^\circ$ denotes the critical angle for total internal reflection. The results are presented only for $|\theta_s| < \theta_s^*$.

4. Conclusions

The scattering of normally incident p- or s-polarized light from a one-dimensional randomly rough interface between two dielectric media is studied. Based on phase perturbation theory, it is demonstrated that using a broadband Gaussian

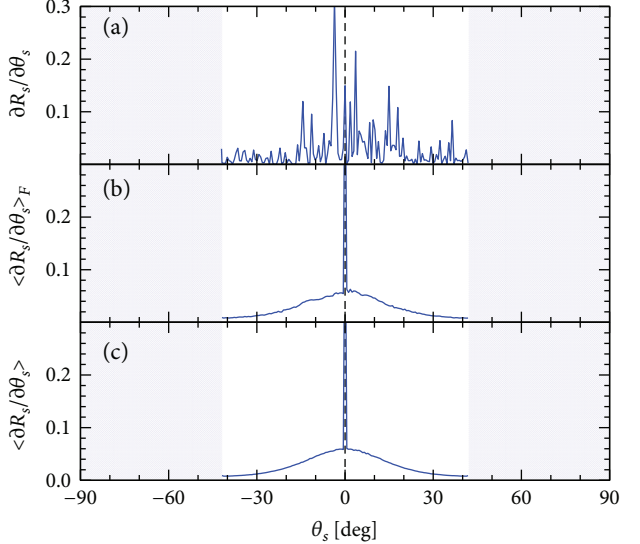


FIGURE 6: Same as Figure 5 ($\epsilon_1 = 2.25$ and $\epsilon_2 = 1$) but assuming s-polarized illumination.

beam to illuminate the surface produces a differential reflection coefficient that closely matches the one produced by a monochromatic Gaussian beam when the resulting differential reflection coefficient is averaged over the ensemble of realizations of the interface profile function. This result is obtained since the broadband beam averages over the speckles produced by a monochromatic beam.

The confirmation of the conjecture prompting the present work by these proof-of-concept calculations encourages

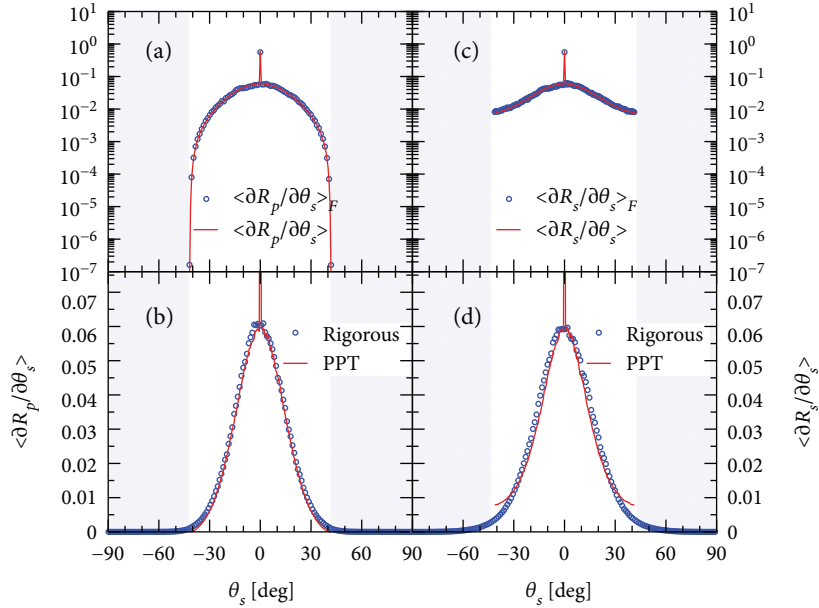


FIGURE 7: Same as Figure 4 but for a glass-vacuum system ($\epsilon_1 = 2.25$ and $\epsilon_2 = 1$).

additional calculations using rigorous computer simulation methods instead of the phase perturbation theory approach, to explore the efficacy of a broadband source in calculations of rough surface scattering phenomena and in experimental studies of them.

Conflicts of Interest

The authors declare that there are no conflicts of interest regarding the publication of this paper.

Acknowledgments

The research of Inge Simonsen was supported in part by the Research Council of Norway (contract 216699) and the French National Research Agency (ANR-15-CHIN-0003).

References

- [1] J. W. Goodman, "Some fundamental properties of speckle," *Journal of the Optical Society of America*, vol. 66, no. 11, pp. 1145–1150, 1976.
- [2] A. A. Maradudin, T. A. Leskova, and E. R. Méndez, "Replacement of ensemble averaging by the use of a broadband source in scattering from randomly rough surfaces," in *23rd Annual Review of Progress in Applied Computational Electromagnetics (ACES, University, MS)*, pp. 1915–1919, 2007.
- [3] J. M. Stone, *Radiation and Optics*, McGraw-Hill, New York, 1963, Sec. 12-6.
- [4] C. W. Tsai, Y. C. Chang, G. S. Shmavonyan, Y. S. Su, and C. F. Lin, "Extremely broadband superluminescent diodes/semitriconductor optical amplifiers in optical communications band," in *Proc. SPIE 4989, Optical Devices for Fiber Communication IV*, pp. 69–77, 2003.
- [5] F. Toigo, A. Marvin, V. Celli, and N. R. Hill, "Optical properties of rough surfaces: general theory and the small roughness limit," *Physical Review B*, vol. 15, pp. 5618–5626, 1977.
- [6] A. A. Maradudin, E. R. Méndez, and T. A. Leskova, *Designer Surfaces*, Elsevier Science & Technology, Oxford, UK, 2008, Sec. 2.2.
- [7] R. M. Fitzgerald and A. A. Maradudin, "A reciprocal phase-perturbation theory for rough-surface scattering," *Waves in Random Media*, vol. 4, pp. 275–296, 1994.
- [8] I. Simonsen, "Optics of surface disordered systems: a random walk through rough surface scattering phenomena," *The European Physical Journal Special Topics*, vol. 181, pp. 1–103, 2010.
- [9] A. A. Maradudin, T. Michel, A. R. McGurn, and E. R. Méndez, "Enhanced backscattering of light from a random grating," *Annals of Physics*, vol. 203, pp. 255–307, 1990.
- [10] A. A. Maradudin, E. R. Méndez, and T. A. Leskova, *Designer Surfaces*, Elsevier Science & Technology, Oxford, UK, 2008, Sec. 2.9.
- [11] V. Freilikher, E. Kanziiper, and A. A. Maradudin, "Coherent scattering enhancement in systems bounded by rough interfaces," *Physics Reports*, vol. 288, pp. 127–204, 1997, Appendix A.

Review Article

Modelling Scattering of Electromagnetic Waves in Layered Media: An Up-to-Date Perspective

Pasquale Imperatore,¹ Antonio Iodice,² Matteo Pastorino,³ and Nicolas Pinel⁴

¹*Institute for Electromagnetic Sensing of the Environment (IREA), National Research Council (CNR), Napoli, Italy*

²*Department of Electrical Engineering and Information Technology, University of Naples Federico II, Napoli, Italy*

³*Department of Electrical, Electronic, Telecommunications Engineering and Naval Architecture (DITEN), University of Genoa, Genova, Italy*

⁴*Icam, School of Engineering, Nantes Campus, Carquefou, France*

Correspondence should be addressed to Pasquale Imperatore; imperatore.p@irea.cnr.it

Received 8 July 2017; Accepted 13 September 2017; Published 5 November 2017

Academic Editor: N. Nasimuddin

Copyright © 2017 Pasquale Imperatore et al. This is an open access article distributed under the Creative Commons Attribution License, which permits unrestricted use, distribution, and reproduction in any medium, provided the original work is properly cited.

This paper addresses the subject of electromagnetic wave scattering in layered media, thus covering the recent progress achieved with different approaches. Existing theories and models are analyzed, classified, and summarized on the basis of their characteristics. Emphasis is placed on both theoretical and practical application. Finally, patterns and trends in the current literature are identified and critically discussed.

1. Introduction

The problem of electromagnetic (EM) wave scattering in layered or stratified media has become an extremely important subject with theoretical and practical relevance.

Indeed, most of the real structures of interest, both those occurring naturally and those fabricated artificially, can be reasonably assimilated to layered structures to some degree. As a matter of fact, the solution of Maxwell equations in such structures poses serious difficulties of a mathematical nature, and there is no general and uniform approach. In fact, methods of studying scattering phenomena in layered media are greatly diversified. They depend on the kind and description of structure (objects embedded in layers, inhomogeneities distributed in a continuous manner or in the form of randomly distributed discrete scattering elements, etc.), on the information at our disposal concerning the structure of the medium, and on the kind of information that is sought about the wave process in question. Depending on the application context, the investigation on wave phenomena in layered structure, in some cases, can be successfully conducted by resorting to deterministic description; however, as far as

natural scenarios are concerned, a stochastic description can provide a more adequate description of reality.

Within this framework, a clear understanding of the wave scattering processes taking place in the layered structures still poses great theoretical challenges. Accordingly, modelling EM scattering phenomena in stratified media is an active area of research with many practical applications, and there exists a very extensive literature on the subject. The inherent problem formulation can be treated from several viewpoints. As a first distinction, the existing techniques can be grouped into two main classes: direct and inverse approaches. Direct scattering models for layered structures have a practical relevance in a number of contexts, such as radio-wave propagation, optics, radar imaging, and microwave remote sensing. Direct modelling methods can generally be categorized in analytical and numerical methods. Some of them turn out more appropriate, in terms of accuracy and computational cost, in a specific application context. Stratified structures play a paramount role also in the solution of electromagnetic inverse scattering problems, which are involved in imaging of hidden or buried targets in multilayer media. Nondestructive testing and evaluations represent significant example, as well

as the modelling of layered structures in through-the-wall procedures for security applications and in the geophysical prospecting of buried cultural heritages.

Numerous recent publications, in the last decades, witness an increasing interest in the study of scattering interactions in layered structures, with advancements including both analytical and computational approaches. Nonetheless, the significant progress on this topic, which has also been driven by emerging applications, deserves to be framed and discussed in an organized way.

Therefore, this paper aims at providing a concise and organized exposition of the existing methods of analysis of EM scattering in layered media. Moreover, the emphasis is placed on conceptual advancements and novel methods that have been recently established, thus outlining important new research directions. The different methodologies are classified on the basis of their characteristics, also discussing pertinent basic principles, advantages, and disadvantages.

The paper is organized as follows. Section 2 focused on existing analytical formulations, with a particular emphasis on recently developed functional forms for rough multi-layer media scattering. Numerical methods of interest are addressed in Section 3, thus covering both well-established and innovative methods. Section 4 is devoted to EM inverse scattering problems in layered structures, also delineating current progress and trends.

2. Analytical Formulations

The analytical evaluation of the scattering in layered media has received considerable attention in last decades [1–56], due to its crucial role played in the different applications. Indeed, the analytical approach permits an understanding of the functional dependence of the scattering response on the structure parameters and, in some cases, an intelligible explanation of the underlying phenomenon.

Conversely, the regime of validity inherent to the approximate solutions implies a limited application domain. In the following, the emphasis is placed on scattering from layered media with rough interfaces. In particular, we consider the two main classical approaches for scattering from rough dielectric surface that have recently been extended to deal with layered configurations. The first classical approach is provided by the *perturbative theory*. At the end of 19th century, Lord Rayleigh originally proposed for the first time the *small perturbations method* (SPM) for the description of wave scattering from a surface separating two media. SPM has been further developed by a number of authors [1–3]. The second traditional approach is referred to as the *Kirchhoff approximation*, in which the tangent plane approximation is used to compute the tangential fields at the interfaces [1, 2]. For each approach, the corresponding extension to a layered configuration is extensively discussed in the following. Further approaches are also considered in Section 2.3.

2.1. Perturbative Methods. We refer to the 3D rough multilayered structure depicted in Figure 1. Each layer is assumed to be homogeneous and characterized by deterministic parameters: the dielectric relative permittivity ϵ_m and the thickness

$\Delta_m = d_m - d_{m-1}$. In general, the interfacial roughness is assumed to be described by a random function of the space coordinates.

In such a case, an approximated solution for the actual structure, which can be described by small changes with respect to an idealized (unperturbed) structure, is obtained by suitably taking advantage of the exact solution available for the associated unperturbed problem.

Within this framework, two different systematic formulations have recently been introduced to deal with the analysis of a layered structure with an arbitrary number of rough interfaces. Specifically, the results of the *boundary perturbation theory* (BPT) [4–6] lead to polarimetric, formally symmetric, and physically revealing closed-form analytical solutions. In this case, a suitable perturbation pertinent to the structure geometry is concerned. The *volumetric-perturbative reciprocal theory* (VPRT) for the evaluation of the scattering from a layered structure with an arbitrary number of rough interfaces considers a perturbation pertinent to the dielectric properties of the structure [7–9]. It is important to note that both BPT and VPRT lead to formally identical expressions of the first-order scattered field. The BPT/VRPT fist-order solution is hereinafter detailed for a monostatic configuration in terms of *normalized radar scattering cross section* (NRCS). Assuming a p -polarized incident wave impinging on the structure from the upper half space (see Figure 1), the NRCS of the layered medium with N corrugated interfaces can be expressed in compact closed-form as follows:

$$\begin{aligned} \tilde{\sigma}_{\text{pp}}^0 = & \pi k_0^4 \sum_{n=0}^{N-1} |\tilde{\alpha}_{\text{pp}}^{n,n+1}(k_\perp^i)|^2 W_n(-2k_\perp^i) \\ & + \pi k_0^4 \sum_{n \neq m} \operatorname{Re} \left\{ \tilde{\alpha}_{\text{pp}}^{n,n+1}(k_\perp^i) (\tilde{\alpha}_{\text{pp}}^{m,m+1}(k_\perp^i))^* \right\} \\ & \cdot W_{nm}(-2k_\perp^i), \end{aligned} \quad (1)$$

wherein $\tilde{\alpha}_{\text{pp}}^{m,m+1}$ denotes the polarimetric coefficient pertinent to the rough interface between the layers m and $m+1$, whose expressions are

$$\begin{aligned} \tilde{\alpha}_{\text{hh}}^{m,m+1}(k_\perp^i) = & -(\epsilon_{m+1} - \epsilon_m) (\xi_{0 \rightarrow m}^{+h}(k_\perp^i))^2 \\ \tilde{\alpha}_{\text{vv}}^{m,m+1}(k_\perp^i) = & (\epsilon_{m+1} - \epsilon_m) \left[\frac{\epsilon_m}{\epsilon_{m+1}} \left(\frac{k_\perp^i}{k_0 \epsilon_m} \xi_{0 \rightarrow m}^{+v}(k_\perp^i) \right)^2 \right. \\ & \left. + \left(\frac{k_{zm}^i}{k_0 \epsilon_m} \xi_{0 \rightarrow m}^{-v}(k_\perp^i) \right)^2 \right], \end{aligned} \quad (2)$$

where $k_{zm}^i = \sqrt{k_m^2 - (k_\perp^i)^2}$, and the following notation has been used:

$$\xi_{0 \rightarrow m}^{\pm p}(k_\perp^i) = \mathcal{T}_{0|m}^p(k_\perp^i) e^{jk_{zm}^i \Delta_m} [1 \pm \mathcal{R}_{m|m+1}^p(k_\perp^i)], \quad (3)$$

with $\mathcal{R}_{m|m+1}^p$ and $\mathcal{T}_{0|m}^p$ denoting the *generalized reflection coefficient* at the interface between the regions m and $m+1$ and the *generalized transmission coefficient* in downward

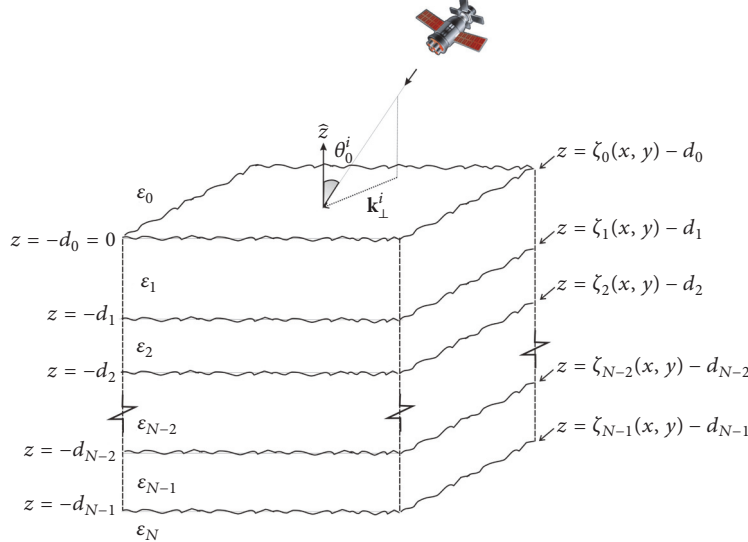


FIGURE 1: Schematic rough multilayer structure. The interfacial roughness of the i th interface is described by the 2D random process $\zeta_i(x, y)$.

direction through the regions 0 and m , respectively. They can be expressed by recursive relations in terms of the *ordinary* transmission and reflection coefficients, like in [6, 10]. Moreover, in (1)–(3) the adopted notation is as follows: the asterisk symbolizes the complex conjugated operator; $\text{Re}\{\}$ denotes the real part operator; $p \in \{v, h\}$ indicates the incident (vertical or horizontal) polarization; \mathbf{k}_\perp^i represents the 2D projection of incident wavenumber vector on the plane $z = 0$ (superscript i referring to the incident field direction); and $k_\perp^i = |\mathbf{k}_\perp^i|$. Finally, $W_n(\boldsymbol{\kappa})$ and $W_{nm}(\boldsymbol{\kappa})$ denote the (spatial) *power spectral density* of n th corrugated interface and the *cross power spectral density* (between the interfaces n and m), respectively [1, 4].

We stress that (1)–(3) represent the backscattering solution; a more general expression valid for a bistatic configuration can be found in [4, 6, 7]. As far as the backscattering case is concerned, it is should be noted that the BPT/VPRT cross-polarized scattering coefficients ($\tilde{\sigma}_{pq}^0$ with $p \neq q$) evaluated in the plane of incidence vanish, in full accordance with the classical first-order SPM method for a rough surface between two different media. Moreover, the dual solution concerning the scattering through the rough multilayer has also been obtained in [5, 6].

The domain of validity of the perturbative solution is defined as follows: the height deviation of the rough interfaces, about the unperturbed interface, is everywhere small compared to the wavelength of the incoming wave and the gradient of the interface is small in comparison to unity [11]. A comprehensive discussion on the relevant domain of applicability is provided in [12, 13]. Concerning the considered BPT/VPRT solutions, several comments are in order.

First, we discuss the inherent functional form. The closed-form solution (1)–(3) makes the functional dependence of scattering properties on layered structure (geometric and electromagnetic) parameters explicit. Specifically, the analytical solution permits the evaluation of the backscattering from the layered rough structure, once the 3D layered structure

parameters (shape of the roughness spectra, layer thickness, and complex permittivity) and the incident field parameters (frequency, polarization, and direction of incidence) have been specified. Therefore, the considered perturbative solution provides a forward solver whose recursive formulation results in effective computational time. Furthermore, the NRCS of the layered media is sensitive to the correlation between rough profiles of different interfaces. In particular, when completely uncorrelated random interfaces are concerned ($W_{nm}(\boldsymbol{\kappa}) = 0$), scattered intensity (in the first-order approximation) arises from the incoherent superposition of the field contributions scattered from each rough interface [see (1)]. Interface roughness description (and the corresponding spectral representation) is typically provided in terms of classical parameters (height standard deviation and correlation length); however, it can also be expressed in terms of the fractal parameters [14, 15]. Indeed, fractal description for the interfacial roughness has also been adopted for evaluating scattering from multilayered structures (see also Section 2.2.3). A *fractional Brownian motion* (fBm) process based description has been used in conjunction with the BPT scattering solution in [16].

Second, we provide a perspective on the interpretability of the perturbative solutions. The physical meaning of the perturbative solutions for the scattering *from* and *through* the 3D layered structure has been investigated in [17, 18], where a physically revealing interpretation involving *ray-series* representation is obtained by rigorously establishing a functional decomposition of the first-order scattering solutions in terms of basic single-scattering local processes. Accordingly, the fundamental interactions in the multilayer contemplated by the mathematical solutions can be revealed, thus gaining a neat picture of the physical meaning of the theoretical construct. Furthermore, the VPRT procedure can also be reformulated in a more physically sound way by avoiding use of Dirac delta function and distribution theory. Such VPRT reformulation also enables an interesting interpretation in

terms of *internal field* approximation, which is consistent with the gently rough assumption, thus providing an additional insight into the first-order approximation (which is slightly different from the usual *Born* approximation) [1, 12]. Another interesting interpretation of the scattering solution can be given in terms of multireaction, by exploiting the fundamental concept of *Rumsey* reaction [7, 10].

Third, the theoretical and experimental consistencies of the perturbative solution deserve to be discussed. Regarding the former, it is important to highlight that all the previous existing perturbative scattering models, introduced by different authors to deal with some simplified layered geometry, with one [19–21] or two [22] rough interfaces, can be all rigorously regarded as a special cases of the general BPT/VPRT solutions [4, 7, 23]. Accordingly, BPT/VPRT results can be regarded as the generalization of the classical first-order SPM for rough surface to the case of rough multilayer. As a matter of fact, the validity of a mathematical model resides in the concordance of model-based predictions with experimental observations. In this regard, it is worth mentioning that a first assessment of the BTP solution validity in a real scenario has been provided in [24], thus showing that theoretical predictions are in good accordance with the experimental evidence.

Second and higher-order perturbative developments have also been investigated [9, 26–29]. It is worth highlighting that pertinent analytical developments following a boundary perturbation approach can be particularly cumbersome [27]; conversely, rigorous second-order volumetric-perturbative developments demand for an appropriate mathematical playground (the distribution theory for discontinuous test functions) [9]. In particular, in [27] the predictions of the fourth-order perturbation have been examined for scattering from two rough surfaces in a layered geometry. Accordingly, the interaction effects between the two surfaces can, in some cases, be the dominant contribution to cross-pol returns. Notice that the first-order solution for the scattered field does not predict the cross-polarized intensity in the incidence plane. In [29] it has been demonstrated that there exists a “strong” condition of energy conservation in that the kernel functions multiplying the spectral density of each interface obey energy conservation exactly. Accordingly, the energy is conserved independent of the roughness spectral densities of the rough surfaces. Finally, we observe that the development of perturbative approaches enabling systematical evaluation of both interfacial and volumetric inhomogeneity in layered media is a main challenge.

2.2. Kirchhoff Approach/PO. Here, focus is made on the so-called Kirchhoff-tangent plane approximation, often called Kirchhoff approximation (KA) for short, in which the tangent plane approximation is used to calculate the tangential fields at the interfaces. It is often rather called physical optics (PO) approximation by numericians or in the radar community [30, 31]. This approximation is valid for surfaces that can be considered as locally flat. Thus, at moderate angles, the validity domain is such that the mean surface curvature radius is significantly greater than the EM wavelength. It may then be considered as a high-frequency approximation.

As a consequence, at each surface point, the surface can be replaced by its tangent plane, which is a flat surface whose local slope vector is that of the original random rough surface at considered surface point. Then, each ray of the incident wave is reflected/transmitted in the appropriate local specular direction.

However, it must be emphasized that this model becomes less valid for angles becoming lowly grazing (in particular, for low-grazing incidence): it is due to the phenomenon of shadowing of the surface. In such configurations, it is necessary to introduce a corrective parameter called shadowing function (or illumination function) to overcome this issue [32]. Besides, unless the process of scattered field calculation is iterated, the KA does not take the phenomenon of multiple scattering into account. This reduces the validity of the model to surfaces having small to moderate slopes, typically RMS slopes less than about 0.3–0.5 [33].

Starting from the calculation of the scattered field, we are usually interested in calculating a mean scattered intensity. Then, the KA is often not used as such, as it is usually desired to further simplify the mathematical expression of the average scattered intensity, in order to get faster numerical results. It is particularly true here when we are interested in analytical formulations. Usually, two opposite solutions are elected: the first one considers very rough surfaces (the geometric optics (GO) approximation) and the other one slightly rough surfaces (the scalar Kirchhoff approximation (SKA)). Then, the GO calculates only the incoherent scattered intensity, whereas the SKA generally focuses on the calculation of the coherent scattered intensity.

2.2.1. GO Model. Let us first focus on the GO model. The classical GO model for single reflection onto a rough surface uses the so-called method of stationary phase (MSP) to simplify the expression of the scattered field (or intensity). This method assumes that only the surface points that specularly reflect/transmit the incident wave into the observation direction contribute to the scattering process. This restricts the contribution to surface slopes checking $\gamma = -Q_H/Q_z$, with $Q = k^r - k^i$ called the Ewald vector (k^i and k^r being the incidence and reflection wave vectors, resp.), Q_H and Q_z being the horizontal and vertical components of Q , respectively. From the MSP, the GO model further simplifies the scattered intensity by retaining only the surface points that are highly correlated. Thus, the NRCS under the GO is only incoherent and can be expressed as follows [34]:

$$\sigma_{r,1}^0(k^r, k^i) = \left| \frac{\mathbb{K}(k^r, k^i)}{Q_z} \right|^2 p_s \left(\gamma = -\frac{Q_H}{Q_z} \right) S(k^i, k^r | \gamma) \quad (4)$$

with \mathbb{K} being the so-called Kirchhoff kernel, which is a polarization-dependent term proportional to the Fresnel reflection coefficient and related to the projection of the incident wave vector onto the normal to the surface. S is the shadowing function [32].

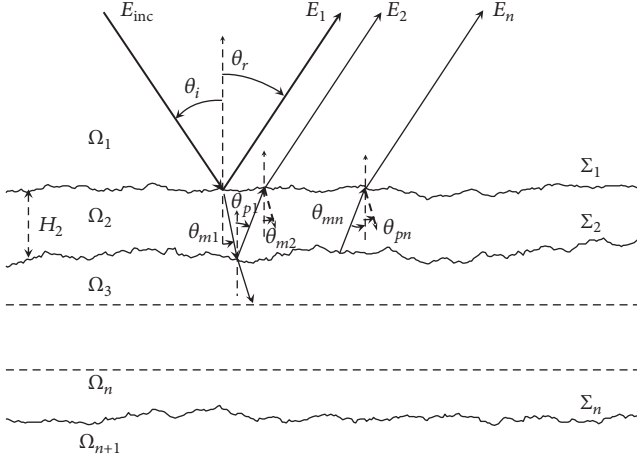


FIGURE 2: Configuration of the different orders of reflection from a multilayer, focus on the upper layer Ω_2 .

The extension of the GO to a layer of two random rough interfaces has been first led for 2D problems [35, 36]. By doing so, the NRCS associated with a given order of reflection from the layer (see Figure 2) has the great advantage of being proportional to the product of elementary NRCS corresponding to each scattering in reflection or transmission at a given interface. It may be written in the following form for the second-order NRCS (associated with the field E_2 in Figure 2) [35, 36]:

$$\sigma_{r,2}^0(\theta_r, \theta_i) \propto \iint d\theta_{m1} d\theta_{p1} \sigma_{t21}^0(\theta_r, \theta_{p1}) \\ \cdot \sigma_{r23}^0(\theta_{p1}, \theta_{m1}) \sigma_{t12}^0(\theta_{m1}, \theta_i) \quad (5)$$

with σ_{t12}^0 being the NRCS associated with the transmission of the incident wave into the inner layer Ω_2 , σ_{r23}^0 the NRCS associated with the reflection of this wave onto the lower interface Σ_2 , and σ_{t21}^0 the NRCS associated with the transmission of this wave back into the incidence medium Ω_1 . Then, it has been shown that this approach can be generalized to any order n of reflection from the layer (associated with the field E_n in Figure 2) as [36]

$$\sigma_{r,n}^0(\theta_r, \theta_i) \propto \int \cdots \int d\theta_{m1} d\theta_{pn} \sigma_{t21}^0(\theta_r, \theta_{pn}) \sigma_{r23}^0(\theta_{pn}, \theta_{m1}) \\ \cdot \sigma_{t12}^0(\theta_{m1}, \theta_i) \\ \times \prod_{k=2}^{n-1} [d\theta_{p(k-1)} d\theta_{mk} \sigma_{r21}^0(\theta_{p(k-1)}, \theta_{mk}) \\ \cdot \sigma_{r23}^0(\theta_{mk}, \theta_{pk})]. \quad (6)$$

Then, the number of numerical integrations to be computed is equal to $n - 1$. For the more general case of 3D problems, unfortunately it is not possible to write the NRCS in such a compact way of a product between NRCS, owing to the

fact that the polarization terms are not scalar anymore but become square matrices of length 2. This is due to the co- and cross-polarization terms that must be considered for having a correct computation of the physical contributions to the scattering process [37, 38]. This approach has been validated by a reference numerical method based on the method of moments [37, 38].

2.2.2. SKA Model. Starting from the KA for calculating the scattered field, the scalar Kirchhoff approximation [39], also called zero-order KA [40], is an alternative to the GO model. This approximation is valid for calculating the scattered field around nadir for slightly rough surfaces. It is generally used for evaluating the coherent scattered intensity.

In the context of scattering from random rough layers, each order contribution must be calculated, or at least the first orders. The first order is well known and corresponds to the scattering from a single rough interface. Under this model, it has been shown that taking the interface roughness into account is simple and consists in replacing the Fresnel reflection coefficient r_{12} by a modified reflection coefficient \tilde{r}_{12} checking [39, 40]

$$\tilde{r}_{12} = r_{12} \exp(-2\kappa_{1z}^2 \sigma_{h1}^2) \quad (7)$$

with σ_{h1} being the RMS height of the upper interface Σ_1 and κ_{1z} the vertical component of the propagation vector inside Ω_1 (see Figure 2). The term $\kappa_{1z}\sigma_{h1}$ is sometimes referred to as the Rayleigh roughness parameter, which accounts for the attenuation of the field amplitude due to the interface roughness. The extension to the calculation of the second-order contribution leads to an attenuation of [39, 40]

$$\exp(-2\kappa_{2z}^2 \sigma_{h2}^2) \exp(-(\kappa_{1z} - \kappa_{2z})^2 \sigma_{h1}^2) \quad (8)$$

with σ_{h2} being the RMS height of the interface Σ_2 and κ_{2z} the vertical component of the propagation vector inside Ω_2 . Then, by calculating each order contribution, it is possible to obtain a new equivalent reflection coefficient \tilde{R}_{eq} of the form [40]

$$\tilde{R}_{eq} = \tilde{r}_{12} + \frac{(1 - \tilde{r}_{12}^2)\tilde{r}_{23} \exp(i2\kappa_{2z}H_2)}{1 + \tilde{r}_{12}\tilde{r}_{23} \exp(i2\kappa_{2z}H_2)} \quad (9)$$

with $\tilde{r}_{23} = r_{23} \exp(-2\kappa_{2z}^2 \sigma_{h2}^2)$ and H_2 being the mean thickness of the layer Ω_2 . For perfectly flat interfaces $\sigma_{h1} = \sigma_{h2} = 0$, this reduces to the classical formula of generalized reflection coefficient $\mathcal{R}_{1|2}^P$ [4, 10, 40]:

$$\mathcal{R}_{1|2}^P = \frac{r_{12} + r_{23} \exp(i2\kappa_{2z}H_2)}{1 + r_{12}r_{23} \exp(i2\kappa_{2z}H_2)}. \quad (10)$$

This approach has been validated by comparison with numerical methods [39, 40].

2.2.3. KA Model and Fractal Surfaces. It is finally worth mentioning that the KA can be adapted to evaluate electromagnetic scattering from fractal surfaces. Fractal geometry was introduced by Mandelbrot in the '70s of the last century

to provide a mathematical tool for the complex and irregular shapes of natural objects [14]. Effectiveness of fractals to describe natural surfaces has been demonstrated in a very impressive way by producing surprisingly realistic computer-generated synthetic landscapes [14]. Accordingly, fractal models, and in particular the *fractional Brownian motion* (fBm) model, have been extensively used in different fields to describe natural surfaces. The reason of this success is the ability of fractal models to properly account for the statistical scale invariance properties (self-affinity) of natural surfaces. We recall that a set is *self-similar* if it is invariant (possibly in a statistical sense) with respect to a transformation in which all the coordinates are scaled down by the same factor, whereas it is *self-affine* if it is invariant (possibly in a statistical sense) with respect to a transformation in which coordinates are scaled down by factors not all equal. Self-affinity of fractal sets is the key property that makes them particularly useful in describing natural surfaces. However, while fractal sets maintain their self-affinity at any (arbitrarily small or large) observation scale, natural surfaces have characteristic inner and outer scales. In other words, they exhibit fractal characteristics only on a wide but limited range of scale lengths (*range of fractalness*). When an electromagnetic wave impinges on a natural surface, the range of scale lengths involved in the scattering mechanism is limited on one side by the finite dimension of the illuminated surface and on the other by the electromagnetic wavelength. If this range of scales is included in the surface range of fractalness, then the fractal description is appropriate (and can be used) to evaluate the scattered field. This is often the case at microwave frequencies [41].

First studies on application of KA to fBm surfaces (sometimes approximated by Weierstrass-Mandelbrot functions [42]) date back to the last decades of last century [15, 41, 43, 44]. To summarize the obtained results, we have to preliminarily recall that an fBm surface is a 2D random process whose increments over a fixed distance τ are zero-mean Gaussian with variance

$$S(\tau) = T^{(2-2H)} \tau^{2H}, \quad (11)$$

where H is the Hurst coefficient, linked to the surface fractal dimension D by the relation $D = 3 - H$, and T is the surface topography. According to KA, the mean square value of the modulus of the field scattered by an fBm surface is [41]

$$\begin{aligned} \langle |E_{pq}|^2 \rangle &= \frac{k^2 |E_p^{(i)}|^2 |\mathbf{K}(k^i, k^r)|^2}{(4\pi R_0)^2} \\ &\cdot 2\pi A \int_0^\infty J_0(|\mathbf{Q}_H| \tau) \exp\left[-\frac{1}{2} Q_z^2 S(\tau)\right] \tau d\tau. \end{aligned} \quad (12)$$

The integral in (12) can be evaluated via two different series expansions: one is an asymptotic expansion of the scattering integral for near-specular directions or high frequency and the other for far-from-specular direction or low frequency. The behavior of these series and their practical evaluation are analyzed in detail in [45]. It has been also highlighted that the

integral in (12) is in the form of the PDF of an alpha-stable process [46–48], and a physical interpretation of this result was provided in [48].

2.3. Other Analytical Approaches. For the sake of completeness, in the following we briefly consider further approaches adopting different schematizations and/or approximations, which deserve to be discussed.

The *small-slope approximation* (SSA) was originally proposed by Voronovich [30, 49]. SSA exhibits an extended domain of applicability, which is aimed at including the domain of the small-perturbation method and the domain of the Kirchhoff approximation. SSA extended to the fourth-order terms of the perturbative development has been considered in [50] for studying slab with uncorrelated rough 2D interfaces. A first-order SSA method applied to an arbitrary number of 1D interfaces has been presented in [51]. In particular, the scattering amplitudes under the first-order small-slope approximation are deduced from results derived from the first-order SPM.

Generally speaking, modelling techniques for describing electromagnetic scattering in a random layered medium can be categorized in two main classes: continuous and discrete. For the continuous case, exact equations for the mean and correlation of the electric field are referred to as the Dyson and Bethe-Salteeper equations, respectively [1]. These equations are difficult to be solved even under ideal conditions, thus simplified assumptions have to be introduced in order to achieve tractable forms. Discrete scattering models, for describing the response of a layer containing a random collection of discrete scatters (e.g., dielectric cylinders or disks), have also been developed (see, e.g., [52–56]). In particular, the scattering coefficients of the layer can be computed using a distorted Born approximation, with the mean wave evaluated according to the Foldy-Lax approximation [1].

However, the consistent treatment of interfacial and volumetric inhomogeneity in layered media is still posing a challenge.

3. Numerical Methods

In this section, the focus is on the main numerical methods of interest, which exhibit different degrees of approximation and computational complexity [57–87]. In particular, we first consider the rigorous numerical techniques referred to as the method of moments (MoM), and then efficient approaches are discussed.

3.1. Method of Moments (MoM). As already mentioned, the electromagnetic field scattered by the rough interfaces of a layered medium can be computed from knowledge of the tangential components of the electric and magnetic fields at the interfaces (i.e., equivalent magnetic and electric surface currents, resp.). To compute such tangential field components, integral equations must be solved [82]. For the complete equations to be solved in the single interface case, the reader is referred to [82] for full 3D problems and to [83] for 2D cylindrical problems; for the equations that apply to the case of two or more interfaces, see Section 3.3 and

references therein. Here, to simplify the notation, we report the scalar version of those integral equations, which is a *Fredholm* equation:

$$\iint_S g(\mathbf{r}, \mathbf{r}') f(\mathbf{r}') d\mathbf{r}' = i(\mathbf{r}) \quad (13)$$

in which S is the interface (or a set of interfaces), \mathbf{r} and \mathbf{r}' are two points over S , $i(\mathbf{r})$ is known (it is a component of the incident field), $g(\mathbf{r}, \mathbf{r}')$ is an element of the dyadic Green function, and $f(\mathbf{r}')$ is the unknown (a component of the tangential fields). This integral equation can be solved numerically by using the method of moments (MoM). The unknown function is expanded by using a finite set of N basis functions $f_n(\mathbf{r}')$

$$f(\mathbf{r}') = \sum_{n=1}^N x_n f_n(\mathbf{r}') \quad (14)$$

and the inner product of both sides of (13) with N test, or weighting, functions $w_m(\mathbf{r})$ is evaluated:

$$\begin{aligned} & \sum_{n=1}^N x_n \iint_S w_m(\mathbf{r}) \iint_S g(\mathbf{r}, \mathbf{r}') f_n(\mathbf{r}') d\mathbf{r}' d\mathbf{r} \\ &= \iint_S w_m(\mathbf{r}) i(\mathbf{r}) d\mathbf{r}. \end{aligned} \quad (15)$$

We then get the system of linear algebraic equations

$$\underline{\underline{A}} \underline{x} = \underline{y} \quad (16)$$

in which

$$\begin{aligned} A_{mn} &= \iint_S w_m(\mathbf{r}) \iint_S g(\mathbf{r}, \mathbf{r}') f_n(\mathbf{r}') d\mathbf{r}' d\mathbf{r}, \\ y_m &= \iint_S w_m(\mathbf{r}) i(\mathbf{r}) d\mathbf{r}, \end{aligned} \quad (17)$$

and x_n are the unknowns. Once the system is solved for x_n , the solution of the original integral equation can be obtained from (14).

If $w_n(\mathbf{r}) = f_n(\mathbf{r})$, that is, the sets of basis and test functions coincide, then we get the *Galerkin* method. A usual choice is to use rectangular pulse basis functions and Dirac pulse test functions, so obtaining the so-called point-matching method. This choice simplifies evaluations of matrix and vector elements, but it requires a high number of unknowns N . Different choices of basis and test functions may lead to a smaller number of unknowns and/or to a sparser matrix. In the framework of the problem of scattering from rough interfaces, the point-matching method is the most used [64–70, 72, 74, 83], but a very popular choice is also the Rao-Wilton-Glisson (RWG) basis [84]. More recently, use of Haar [85], B-spline [85], and Coifman [62, 86, 87] wavelets as basis and test functions in the Galerkin method has also been demonstrated to lead to efficient evaluation of scattered field.

3.2. Iterative Methods. As shown above, by using the MoM, integral equations to be solved to evaluate induced (real or equivalent) surface currents over the (possibly) rough interfaces are converted into a system of linear algebraic equations, whose general form is given by (16). However, direct methods for the solution of linear systems have a high computational cost. In fact, they require a number of computer operations asymptotically increasing as N^3 (i.e., $O(N^3)$), where N is the (usually very large) number of unknowns (i.e., for the point-matching method, of surface points). To reduce computational complexity to $O(N^2)$, iterative methods can be used. Linear iterative methods can be cast in the following general form:

$$\underline{x}^{(n)} = \underline{\underline{G}}^{(n)} \underline{x}^{(n-1)} + \underline{c}^{(n)}, \quad (18)$$

where $\underline{\underline{G}}^{(n)}$ and $\underline{c}^{(n)}$ are linear functions of $\underline{\underline{A}}$ and \underline{y} . If they actually depend on n , that is, they are adaptively changed at each iteration, the iterative method is called *nonstationary*. Different nonstationary methods have been applied to rough interface scattering problem, namely, the conjugate gradient squared (CGS), biconjugate gradient-stable (BICGSTAB), quasiminimum residual (QMR), general minimal residual (GMRES), and conjugate gradient-normal equation (CGNR) [58–62]. Conversely, if $\underline{\underline{G}}$ and \underline{c} do not depend on n , the iterative method is said to be *stationary*. In addition, if we let

$$\begin{aligned} \underline{\underline{G}} &= \underline{\underline{I}} - \underline{\underline{Q}}^{-1} \underline{\underline{A}}, \\ \underline{c} &= \underline{\underline{Q}}^{-1} \underline{y}, \end{aligned} \quad (19)$$

then it can be shown that the iterative procedure (19) converges to the exact solution of (16) if and only if all the eigenvalues of $\underline{\underline{G}}$ lie within the unit circle on the complex plane [63]. Different choices for the “splitting matrix” $\underline{\underline{Q}}$ define the different iterative stationary methods. For instance, $\underline{\underline{Q}} = \underline{\underline{D}}$, where $\underline{\underline{D}}$ is the diagonal part of $\underline{\underline{A}}$, defines the Jacobi (or simple iteration) method. In addition, for

$$\underline{\underline{Q}} = (\underline{\underline{D}} - \underline{\underline{L}}) \underline{\underline{D}}^{-1} (\underline{\underline{D}} - \underline{\underline{U}}), \quad (20)$$

$$\underline{\underline{Q}} = (\underline{\underline{D}}^{(\pi)} - \underline{\underline{L}}^{(\pi)}) \underline{\underline{D}}^{(\pi)-1} (\underline{\underline{D}}^{(\pi)} - \underline{\underline{U}}^{(\pi)}), \quad (21)$$

we get the symmetric successive overrelaxation (SSOR) and the 2×2 -block-SSOR methods (with unitary relaxation parameter ω), respectively. In (20)–(21), $-\underline{\underline{L}}$ and $-\underline{\underline{U}}$ are the lower and upper triangular parts of $\underline{\underline{A}}$, and $\underline{\underline{D}}^{(\pi)}$, $-\underline{\underline{L}}^{(\pi)}$, and $-\underline{\underline{U}}^{(\pi)}$ are the 2×2 block-diagonal, block-lower triangular, and block-upper triangular parts of $\underline{\underline{A}}$ [63]. It turns out that nonstationary methods are in general more robust, meaning that they converge for a wider range of roughness conditions. However, stationary methods have the advantage of having a physical interpretation when applied to the problem of scattering from rough surfaces, so that it is easier to predict interface roughness conditions under which they rapidly converge. In fact, the Jacobi method coincides with the

iterative (or “extended”) Kirchhoff approach (IKA) [64] for perfectly conducting surfaces, whereas SSOR and block-SSOR methods are equivalent to the forward-backward (FB) (or the differently formulated, but equivalent, method of ordered multiple interactions, MOMI) for perfectly conducting [65, 66] and dielectric [67] interfaces, respectively. It is interesting to note that IKA, FB, and MOMI were first devised in [64–66] based on physical considerations, and only subsequently it was shown that they are equivalent to already available stationary methods (in [61] for perfectly conducting surfaces and in [68] for dielectric interfaces).

To illustrate the physical meaning of FB, we need to recall that, as shown in [68], (18)–(19) with (21) can be recast as

$$\left(\underline{\underline{D}}^{(\pi)} - \underline{\underline{L}}^{(\pi)}\right) \underline{x}^{f,(n)} = \underline{y} + \underline{\underline{L}}^{(\pi)} \underline{x}^{b,(n-1)}, \quad (22)$$

$$\left(\underline{\underline{D}}^{(\pi)} - \underline{\underline{U}}^{(\pi)}\right) \underline{x}^{b,(n)} = \underline{\underline{U}}^{(\pi)} \underline{x}^{f,(n)}, \quad (23)$$

with $\underline{x}^{b,(0)} = \underline{0}$, where $\underline{x} = \underline{x}^f + \underline{x}^b$. It can be shown [67] that solution of (22)–(23) does not involve any matrix inversion, except for the inversion of $N 2 \times 2$ matrices. Analysis of these equations shows that, at the first step ($n = 1$), (22) allows calculating the surface currents \underline{x} due to forward scattered waves and (23) based on these currents computes the new currents that are due to both forward and backward scattered waves. Accordingly, computed currents after the first step include all orders of multiple scattering which involve no backward-forward change of direction and no more than one forward-backward change of direction. By iterating the reasoning, it is not difficult to realise that computed currents after the n -th step include all orders of multiple scattering which involve no more than $n - 1$ backward-forward changes of direction and no more than n forward-backward changes of direction. Since scattered energy is not expected to change direction more than a few times (except that for extremely rough surfaces), we conclude that the iterative procedure should converge very rapidly. This expectation is experimentally confirmed for 1D nonreentrant rough profiles [67–69]; for 2D rough surfaces, proper ordering of matrix elements must be performed to obtain convergence of the method [70], even for moderate roughness.

Extension of FB to layered structures with rough interfaces is illustrated in [74] and can be possibly coupled with methods presented in the next subsection. Both stationary and nonstationary iterative techniques can be further accelerated by identifying a strong-interaction region (A_{ij} elements with $|i-j|$ smaller than a prescribed threshold) and a weak-interaction region (all other elements of $\underline{\underline{A}}$) and using some form of approximation when summing up terms corresponding to the weak-interaction region in (18). In this way, it is possible to reduce computational complexity up to $O(N \log N)$ or even $O(N)$. This class of algorithms includes, for instance, the banded-matrix iterative approach/canonical grid method (BMIA/CG) [71], the spectrally accelerated (SA) BCGSTAB [60], and SA-FB [72]. An approach with some analogies with algorithms of this class is the BIE/SDIM (Boundary Integral Equation/Subdomain Decomposition Iterative Method), which has been recently proposed [77]. It is a rigorous method based on MoM, which splits the problem

into subdomains. Similar to the PILE method (see the description in Section 3.3), the diagonal blocks of the global impedance matrix correspond to the subdomain impedance matrices, whereas the off-diagonal blocks correspond to coupling matrices accounting for the interactions between two different subdomains. The principle of SDIM is to invert the impedance matrix by blocks, which significantly reduces the complexity by comparison with a direct LU. In addition, to accelerate the matrix-vector products and to reduce the memory requirement, the adaptive cross approximation (ACA) is applied to compress the subdomain coupling matrices.

Finally, convergence properties of iterative methods can be in some cases improved by using proper preconditioning, that is, by left-multiplying both sides of (16) by the inverse of a preconditioner matrix; see, for example, [73].

3.3. Efficient Approaches. Resolving the scattering by a multilayered medium with a MoM-based method may be time consuming for large surfaces and/or high frequencies, in particular for several interfaces. Then, it is of interest to apply efficient approaches that accelerate the computing process. Most approaches have been described in previous subsection. Here, we will focus on the so-called PILE (Propagation Inside Layer Expansion) method [79, 80] for dealing with surfaces Σ_1 and Σ_2 , as well as its generalized version, GPILE [81], for dealing with surfaces $\Sigma_1, \Sigma_2, \dots, \Sigma_n$ in Figure 2.

Based on the MoM, the main feature of PILE is its ability to split the total scattered field into the contribution of each order of reflection from a layer (see E_1, E_2, \dots, E_n in Figure 2). It has the great advantage of being able to be coupled with acceleration methods existing for scattering from single interfaces, like the BMIA/CG or the FB [76, 77].

We start from the linear system in (16), where \underline{x} is a vector of length $2(N_1 + N_2)$ representing the unknown total field on the surfaces Σ_1 and Σ_2 (N_1 and N_2 are the number of surface samples for the MoM calculation on Σ_1 and Σ_2 , resp.). Then, \underline{x} can be expressed as

$$\underline{x} = \begin{pmatrix} x_1 \\ x_2 \end{pmatrix} \quad (24)$$

with x_1 and x_2 being vectors of length N_1 and N_2 , respectively, containing the unknown fields and their normal derivatives on Σ_1 and Σ_2 , respectively. \underline{y} is a source term vector of length $2(N_1 + N_2)$ such that

$$\underline{y} = \begin{pmatrix} y_1 \\ y_2 \end{pmatrix} \quad (25)$$

where y_1 and y_2 are vectors of length $2N_1$ and $2N_2$, respectively, containing information of the incident field on Σ_1 and Σ_2 , respectively (inside Ω_1 and Ω_2 , resp.; see Figure 2). Here, there is no incident field inside Ω_2 ; hence $y_2 = \underline{0}$. This also holds for the last N_1 terms of y_1 . $\underline{\underline{A}}$ is a square impedance matrix of size $2(N_1 + N_2)$, with

$$\underline{\underline{A}} = \begin{pmatrix} Z_1 & Z_{21} \\ Z_{12} & Z_2 \end{pmatrix}. \quad (26)$$

Z_i is the impedance matrix of size $2N_i \times 2N_i$ of surface Σ_i (with $i = \{1, 2\}$), and Z_{21} of size $2N_1 \times 2N_2$ (for the propagation from Σ_2 to Σ_1) and Z_{12} of size $2N_2 \times 2N_1$ (for the propagation from Σ_1 to Σ_2) are coupling matrices between the two surfaces.

To effectively solve the system $\underline{\underline{A}} \underline{x} = \underline{y}$, the PILE method has been developed [79]. It is based on an inversion by blocks of the impedance matrix, by making a decomposition of domains from the Taylor series expansion of the inverse of the Schur complement. This leads to

$$x_1 = \left[\sum_{p=0}^{P_{\text{PILE}}} M_{c1}^p \right] Z_1^{-1} y_1 = \sum_{p=0}^{P_{\text{PILE}}} Y_1^{(p)}, \quad (27)$$

where $Y_1^{(0)} = Z_1^{-1} y_1$ and $Y_1^{(p)} = M_{c1} Y_1^{(p)}$, with

$$M_{c1} = Z_1^{-1} Z_{21} Z_2^{-1} Z_{12} \quad (28)$$

and $x_1 = -Z_2^{-1} Z_{12} x_1$.

The above series expansion is then valid if $\|M_{c1}^p\| < 1$, with $\|\cdot\|$ the norm operator, which is also here a so-called spectral radius, that is, the modulus of the highest modulus eigenvalue. Physically, the total currents x_1 on the upper surface are the sum of the contributions $Y_1^{(p)}$, which correspond to successive iterations p , corresponding to each order of reflection from the layer $k = p + 1$ (with $k \in \{1, 2, \dots, n\}$ in Figure 2). Thus, by construction, PILE computes the scattered field associated with each order of reflection from the upper layer.

By following the same principle, an extension to 3 interfaces and even a generalization to any number of interfaces have been developed [81]. For more details, the reader is referred to Appendix A of [81].

4. Inverse Scattering Approaches

Layered structures have been widely considered in the solution of electromagnetic inverse scattering problems for imaging purposes. Buried and concealed targets can be inspected by using inverse scattering concepts in several application areas, ranging from nondestructive evaluation and testing to civil engineering, security and military applications, geophysical prospecting, and biomedical diagnostics [88–90].

A possible imaging configuration is sketched in Figure 3, where a target is buried in a stratified medium and is illuminated by a source located in the upper half space (noninvasive imaging). One or more antennas or sensors are used to receive the field scattered by the target. It should be considered that several works have been focused on the detection of the dielectric properties of the various layers (stratified media) [10, 91, 92], whereas for the imaging of concealed targets, the propagating structure is usually assumed to be made of known layers (e.g., in most through-the-wall inspection techniques [93]). The reconstruction process can be performed in time-domain [94] or in the spatial-domain [95]. Time-reversal approaches have also been adopted. In most cases, however, time-harmonic fields are used, with reference to both single- and multifrequency processing [96]. From a

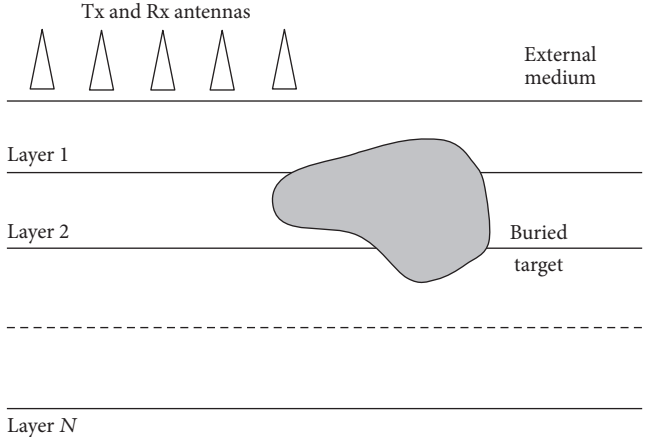


FIGURE 3: Schematic representation of an imaging system for buried object detection in a stratified medium.

general point of view, another classification holds: approaches based on radar and beamforming concepts [97, 98], such as those adopted in breast cancer imaging, and methods based on inverse scattering [90]. In geophysical applications, both methods can be used to inspect shallow buried targets in order to extend the diagnostic capabilities of the so-called ground penetrating radar [99]. Moreover, the inversion procedure can be based on deterministic [100] or stochastic concepts [101].

Considering approaches based on inverse scattering in harmonic fields, the following electric field integral equation (EFIE) can be considered [90] (it is worth noting that other approaches can be followed, e.g., those based on the so-called contrast source formulation [102]):

$$\mathbf{E}_s = \mathbf{E}_t - \mathbf{E}_i = \int_V \gamma \mathbf{E}_t \cdot \mathbf{G}_{\text{str}} dV; \quad (29)$$

in this equation, \mathbf{E}_i , \mathbf{E}_s , and \mathbf{E}_t denote the incident, scattered, and total electric field vectors, respectively. The *scattering potential* is indicated by γ and contains the information about the dielectric properties of the unknown target. Finally, \mathbf{G}_{str} is proper Green's dyadic function for the considered buried or stratified configuration [103].

As it is well known, this equation is nonlinear and severely ill-posed [90]. It can be linearized in the case of presence of weakly scattering targets. One of the most used approximations is the Born one [104], for which the scattered field due to the targets inside the investigation area is expressed in terms of the incident field only. In some case, the use of the second-order Born approximation has been proposed, too [105]. Also the Rytov approximation, which is applied to the complex phase of the field, has been used [106].

It should be mentioned that the Born approximation can be combined with a numerical evaluation of Green's function resulting in a very effective iterative reconstruction procedure, called the distorted-wave Born approximation [107], which is widely used with a great success in several imaging approaches.

Methods based on certain approximations on the considered model can be called qualitative methods [108, 109].

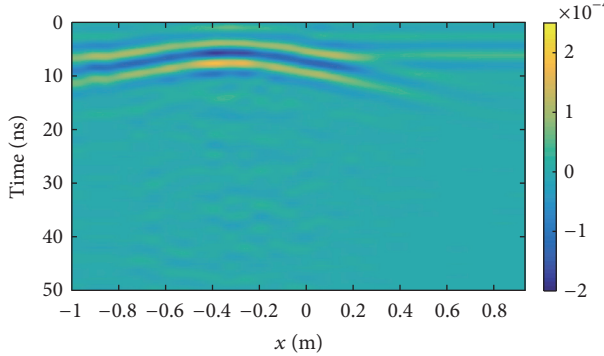


FIGURE 4: B-scan reporting the estimated field scattered by the buried object [96].

They are aimed at retrieving some fundamental properties of a target (e.g., position and shape inside the test area), without providing complete maps of the dielectric properties of the targets.

So far, we mentioned approaches for the imaging of penetrable targets. Different approaches can be adopted for conducting objects [110, 111].

Gauss-Newton methods seem to be very effective deterministic techniques for inspecting buried or stratified targets. Recently, they have been developed also with reference to Lp Banach spaces [112, 113], where the oversmoothing effects usually associated with regularization procedures developed in the common Hilbert space seem to be mitigated. It should be also noticed that sparsity concepts and compressive sensing can be successfully adopted [114, 115].

An example of reconstruction results is reported in the following. The inexact-Newton procedure developed in [96] has been used. It refers to the detection of a two-dimensional buried object in a half space configuration (under transverse magnetic illumination conditions). The considered cross-sectional investigation test domain D_{inv} has height $L_y = 1$ m and width $L_x = 2$ m. The region D_{inv} has been partitioned into 40×20 square cells for solving the forward problem (by means of the method of moments) and 30×15 subdomains for the inversion process. The lower half space medium has dielectric properties $\epsilon_r = 4$ and $\sigma = 0.01$ S/m. The upper half space is air (modelled as vacuum). A dielectric circular cylinder is buried inside D_{inv} . In particular, it has center at $\mathbf{r}_{c1} = (0.35, -0.3)$ m, diameter $d_{c1} = 0.16$ m, dielectric permittivity $\epsilon_r = 8$, and electric conductivity $\sigma = 0.02$ S/m. A GPR B-scan has been simulated by considering $M = 30$ equally spaced measurement positions on a line at height $h = 0.05$ m from the soil level, $S = 2$ m long, and horizontally centered at the origin. The offset between the transmitter and the receiver is $s_{\text{TX}} = 0.3$ m. An additive white Gaussian noise with zero-mean value and signal-to-noise ratio SNR = 10 dB has been used for corrupting the scattered electric field data.

Figure 4 reports the B-scan of the estimated field scattered by the buried cylinder. In the qualitative step, 21 frequency samples equally spaced in the band from 150 MHz to 350 MHz have been used. In the quantitative inversion, a subset of $F = 5$ equally spaced frequencies in the same

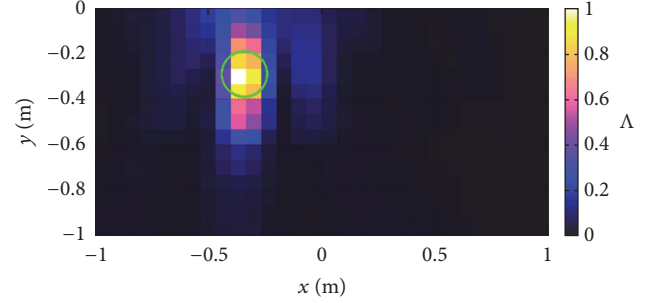


FIGURE 5: Spatial distribution of the normalized object function Λ in the investigation domain D_{inv} , for SNR = 10 dB [96].

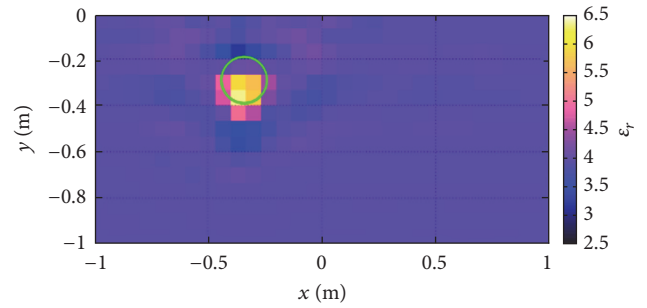


FIGURE 6: Reconstructed distributions of the relative dielectric permittivity in the investigation domain D_{inv} for SNR = 10 dB, obtained considering five frequencies in the considered band [96].

band has been considered. In the inexact-Newton algorithm, $I_{\text{IN}} = 20$ and $K_{\text{LW}} = 10$ maximum Gauss-Newton and Landweber iterations, respectively, have been considered. The distribution of the normalized qualitative object function Λ inside the investigation domain is presented in Figure 5. In Figure 6, the quantitative reconstruction of the relative dielectric permittivity ϵ_r in D_{inv} is shown.

The scientific literature on electromagnetic inverse problem is now very wide and the reader can refer to the mentioned papers and the references therein. A significant interest has also been focused on the use of canonical multilayer objects, since they allow analytical or quasianalytical solutions that can be used for fast computations when dealing with configurations that approximate real imaging cases [116]. In addition, they can be used in the validation phase of inversion procedures. Just as an example, in [117] a two-step inversion procedure for detecting the dielectric permittivity and the velocity of multilayer axially moving targets has been developed, with particular emphasis to cylinders with elliptical cross sections, for which related Green's function has been deduced in [118].

5. Conclusion

Layered structure modelling is an important topic in modern applied electromagnetics. A review of methodologies for the EM scattering in layered media has been presented in this paper. Different techniques in the literature have been

examined and discussed, by emphasizing their basic principles, advantages, and disadvantages. Particularly, special attention has been given to direct methods for modelling scattering in layered rough structure that have been recently established. The role of stratified media in the solution of electromagnetic inverse scattering problems has been discussed, too. In particular, the current trend in the development of inverse procedures for target detection in half spaces and in multilayer materials has been delineated. We emphasize that the model selection generally represents a compromise between accuracy and computational complexity, with the best compromise that may significantly change, depending on the application contexts.

Therefore, our review has been aimed at providing a current perspective on the subject, also highlighting innovative research directions. However, we make no claim to cover all the many topics pertinent to layered media. Indeed, with the rapid growth of the field, such a task would be almost impossible in a single paper.

The list of publications included in the paper is representative for our discussion and will hopefully prove useful to any researcher active in the area. Nonetheless, it does not exhaust the very extensive literature on the subject, which indeed covers several disciplines (optics, applied mathematics, etc.).

Conflicts of Interest

The authors declare that there are no conflicts of interest regarding the publication of this paper.

References

- [1] L. Tsang, J. A. Kong, and R. T. Shin, *Theory of Microwave Remote Sensing*, Wiley, New York, NY, USA, 1985.
- [2] F. G. Bass and I. M. Fuks, *Wave Scattering from Statistically Rough Surfaces*, Pergamon, New York, NY, USA, 1979.
- [3] A. Ishimaru, *Wave Propagation and Scattering in Random Media*, Academic, New York, NY, USA, 1978.
- [4] P. Imperatore, A. Iodice, and D. Riccio, "Electromagnetic wave scattering from layered structures with an arbitrary number of rough interfaces," *IEEE Transactions on Geoscience and Remote Sensing*, vol. 47, no. 4, pp. 1056–1072, 2009.
- [5] P. Imperatore, A. Iodice, and D. Riccio, "Transmission through layered media with rough boundaries: first-order perturbative solution," *IEEE Transactions on Antennas and Propagation*, vol. 57, no. 5, pp. 1481–1494, 2009.
- [6] P. Imperatore, A. Iodice, and D. Riccio, "Boundary perturbation theory for scattering in layered rough structures," in *Passive Microwave Components and Antennas*, V. Zhurbenko, Ed., pp. 1–25, INTECH, 2010.
- [7] P. Imperatore, A. Iodice, and D. Riccio, "Volumetric-perturbative reciprocal formulation for scattering from rough multilayers," *IEEE Transactions on Antennas and Propagation*, vol. 59, no. 3, pp. 877–887, 2011.
- [8] P. Imperatore, A. Iodice, and D. Riccio, "Reciprocity, coupling and scattering: a new look at SPM for rough surface," in *Proceedings of the European Microwave Conference (EuMC '09)*, pp. 994–997, Rome, Italy, September–October 2009.
- [9] P. Imperatore, A. Iodice, and D. Riccio, "Second-order volumetric-perturbative reciprocal scattering theory," *IEEE Transactions on Antennas and Propagation*, vol. 60, no. 3, pp. 1505–1520, 2012.
- [10] W. C. Chew, *Waves and Fields in Inhomogeneous Media*, Van Nostrand Reinhold, 1990, Reprinted IEEE Press, 1995.
- [11] E. I. Thorsos and D. R. Jackson, "The validity of the perturbation approximation for rough surface scattering using a Gaussian roughness spectrum," *The Journal of the Acoustical Society of America*, vol. 86, no. 1, pp. 261–277, 1989.
- [12] P. Imperatore, A. Iodice, and D. Riccio, "Consistency and validity of the perturbative formulations for scattering from rough multilayers," *IEEE Transactions on Antennas and Propagation*, vol. 60, no. 4, pp. 2019–2027, 2012.
- [13] A. Tabatabaeenejad and M. Moghaddam, "Study of validity region of small perturbation method for two-layer rough surfaces," *IEEE Geoscience and Remote Sensing Letters*, vol. 7, no. 2, pp. 319–323, 2010.
- [14] B. B. Mandelbrot, *The Fractal Geometry of Nature*, Freeman, New York, NY, USA, 1983.
- [15] D. L. Jaggard, "On fractal electrodynamics," in *Recent Advances in Electromagnetic Theory*, H. N. Kritikos and D. L. Jaggard, Eds., pp. 183–223, Springer-Verlag, Berlin, Germany, 1990.
- [16] P. Imperatore, A. Iodice, and D. Riccio, "Backscattering from fractal rough multilayer," in *Proceedings of the 2012 32nd IEEE International Geoscience and Remote Sensing Symposium, IGARSS 2012*, pp. 610–613, Munich, Germany, July 2012.
- [17] G. Franceschetti, P. Imperatore, A. Iodice, D. Riccio, and G. Ruello, "Scattering from layered structures with one rough interface: A unified formulation of perturbative solutions," *IEEE Transactions on Geoscience and Remote Sensing*, vol. 46, no. 6, pp. 1634–1643, 2008.
- [18] P. Imperatore, A. Iodice, and D. Riccio, "Physical meaning of perturbative solutions for scattering from and through multilayered structures with rough interfaces," *IEEE Transactions on Antennas and Propagation*, vol. 58, no. 8, pp. 2710–2724, 2010.
- [19] K. Sarabandi and T. Chiu, "Electromagnetic scattering from slightly rough surfaces with inhomogeneous dielectric profiles," *IEEE Transactions on Antennas and Propagation*, vol. 45, no. 9, pp. 1419–1430, 1997.
- [20] A. G. Yarovoy, R. V. De Jongh, and L. P. Ligthart, "Scattering properties of a statistically rough interface inside a multilayered medium," *Radio Science*, vol. 35, no. 2, pp. 455–462, 2000.
- [21] I. M. Fuks, "Wave diffraction by a rough boundary of an arbitrary plane-layered medium," *IEEE Transactions on Antennas and Propagation*, vol. 49, no. 4, pp. 630–639, 2001.
- [22] A. Tabatabaeenejad and M. Moghaddam, "Bistatic scattering from dielectric structures with two rough boundaries using the small perturbation method," *IEEE Transactions on Geoscience and Remote Sensing*, vol. 44, no. 8, 2006.
- [23] P. Imperatore, *Perturbation theory for electromagnetic wave scattering in random layered structures [Ph.D. thesis]*, Dipartimento di Ingegneria Biomedica, Elettronica e delle Telecomunicazioni, Università di Napoli Federico II, Naples, Italy, 2010.
- [24] N. Firoozy, A. S. Komarov, J. Landy, D. G. Barber, P. Mojabi, and R. K. Scharien, "Inversion-based sensitivity analysis of snow-covered sea ice electromagnetic profiles," *IEEE Journal of Selected Topics in Applied Earth Observations and Remote Sensing*, vol. 8, no. 7, pp. 3643–3655, 2015.
- [25] S. Afifi and R. Dusseaux, "On the co-polarized phase difference of rough layered surfaces: formulae derived from the small

- perturbation method," *IEEE Transactions on Antennas and Propagation*, vol. 59, no. 7, pp. 2607–2618, 2011.
- [26] C.-A. Guérin and A. Sentenac, "Second-order perturbation theory for scattering from heterogeneous rough surfaces," *Journal of the Optical Society of America A: Optics and Image Science, and Vision*, vol. 21, no. 7, pp. 1251–1260, 2004.
- [27] M. A. Demir, J. T. Johnson, and T. J. Zajdel, "A study of the fourth-order small perturbation method for scattering from two-layer rough surfaces," *IEEE Transactions on Geoscience and Remote Sensing*, vol. 50, no. 9, pp. 3374–3382, 2012.
- [28] H. Zamani, A. Tavakoli, and M. Dehmollaian, "Second-Order Perturbative Solution of Cross-Polarized Scattering From Multilayered Rough Surfaces," *IEEE Transactions on Antennas and Propagation*, vol. 64, no. 5, pp. 1877–1890, 2016.
- [29] M. Sanamzadeh, L. Tsang, J. T. Johnson, R. J. Burkholder, and S. Tan, "Scattering of electromagnetic waves from 3D multi-layer random rough surfaces based on the second-order small perturbation method: Energy conservation, reflectivity, and emissivity," *Journal of the Optical Society of America A: Optics and Image Science, and Vision*, vol. 34, no. 3, pp. 395–409, 2017.
- [30] G. Voronovich, *Wave Scattering from Rough Surfaces*, Springer, Berlin, Germany, 1994.
- [31] F. T. Ulaby, R. K. Moore, and A. K. Fung, *Microwave Remote Sensing: Active and Passive*, Artech House, Dedham, MA, USA, 1982.
- [32] B. G. Smith, "Geometrical shadowing of a random rough surface," *IEEE Transactions on Antennas and Propagation*, vol. 15, no. 5, pp. 668–671, 1967.
- [33] A. Ishimaru, "Experimental and theoretical studies on enhanced backscattering from scatterers and rough surfaces," in *Scattering in Volumes and Surfaces*, Elsevier, North-Holland, 1990.
- [34] N. Pinel and C. Bourlier, *Electromagnetic Wave Scattering from Random Rough Surfaces – Asymptotic Models*, Wiley – Focus Series, 2013.
- [35] N. Pinel, N. Déchamps, C. Bourlier, and J. Saillard, "Bistatic scattering from one-dimensional random rough homogeneous layers in the high-frequency limit with shadowing effect," *Waves in random and complex media*, vol. 17, no. 3, pp. 283–303, 2007.
- [36] N. Pinel and C. Bourlier, "Scattering from very layers under the geometric optics approximation: further investigation," *Journal of the Optical Society of America A: Optics, Image Science & Vision*, vol. 25, no. 6, pp. 1293–1306, 2008.
- [37] N. Pinel, J. T. Johnson, and C. Bourlier, "A geometrical optics model of three dimensional scattering from a rough surface over a planar surface," *IEEE Transactions on Antennas and Propagation*, vol. 57, no. 2, pp. 546–554, 2009.
- [38] N. Pinel, J. T. Johnson, and C. Bourlier, "A geometrical optics model of three dimensional scattering from a rough layer with two rough surfaces," *IEEE Transactions on Antennas and Propagation*, vol. 58, no. 3, pp. 809–816, 2010.
- [39] N. Pinel, C. Le Bastard, C. Bourlier, and M. Sun, "Asymptotic modeling of coherent scattering from random rough layers: Application to road survey by GPR at nadir," *International Journal of Antennas and Propagation*, vol. 2012, Article ID 874840, 2012.
- [40] A. Tabatabaeenejad, X. Duan, and M. Moghaddam, "Coherent scattering of electromagnetic waves from two-layer rough surfaces within the kirchhoff regime," *IEEE Transactions on Geoscience and Remote Sensing*, vol. 51, no. 7, pp. 3943–3953, 2013.
- [41] G. Franceschetti, A. Iodice, M. Migliaccio, and D. Riccio, "Scattering from natural rough surfaces modeled by fractional Brownian motion two-dimensional processes," *IEEE Transactions on Antennas and Propagation*, vol. 47, no. 9, pp. 1405–1415, 1999.
- [42] D. Riccio and G. Ruello, "Synthesis of Fractal Surfaces for Remote-Sensing Applications," *IEEE Transactions on Geoscience and Remote Sensing*, vol. 53, no. 7, pp. 3803–3814, 2015.
- [43] M. V. Berry and T. M. Blackwell, "Diffraction echoes," *Journal of Physics A: Mathematical and General*, vol. 14, no. 11, pp. 3101–3110, 1981.
- [44] O. I. Yordanov and K. Ivanova, "Kirchhoff diffractals," *Journal of Physics A: Mathematical and General*, vol. 27, no. 17, pp. 5979–5993, 1994.
- [45] S. Perna and A. Iodice, "On the use of series expansions for Kirchhoff diffractals," *IEEE Transactions on Antennas and Propagation*, vol. 59, no. 2, pp. 595–610, 2011.
- [46] I. Simonsen, D. Vandembroucq, and S. Roux, "Electromagnetic wave scattering from conducting self-affine surfaces: an analytic and numerical study," *Journal of the Optical Society of America A: Optics, Image Science & Vision*, vol. 18, no. 5, pp. 1101–1111, 2001.
- [47] K. F. Warnick, F. W. Millet, and D. V. Arnold, "Physical and geometrical optics for 2-D rough surfaces with power-law height spectra," *IEEE Transactions on Antennas and Propagation*, vol. 53, no. 3, pp. 922–932, 2005.
- [48] A. Iodice, A. Natale, and D. Riccio, "Kirchhoff scattering from fractal and classical rough surfaces: physical interpretation," *IEEE Transactions on Antennas and Propagation*, vol. 61, no. 4, part 2, pp. 2156–2163, 2013.
- [49] A. Voronovich, "Small-slope approximation for electromagnetic wave scattering at a rough interface of two dielectric half-spaces," *Waves in Random and Complex Media*, vol. 4, no. 3, pp. 337–367, 1994.
- [50] G. Berginc and C. Bourrelly, "The small-slope approximation method applied to a three-dimensional slab with rough boundaries," *Progress in Electromagnetics Research*, vol. 73, pp. 131–211, 2007.
- [51] A. Berrouk, R. Dusséaux, and S. Affif, "Electromagnetic wave scattering from rough layered interfaces: Analysis with the small perturbation method and the small slope approximation," *Progress in Electromagnetics Research B*, no. 57, pp. 177–190, 2014.
- [52] R. H. Lang, "Electromagnetic backscattering from a sparse distribution of lossy dielectric scatterers," *Radio Science*, vol. 16, no. 1, pp. 15–30, 1981.
- [53] R. H. Lang and J. S. Sidhu, "Electromagnetic Backscattering From a Layer of Vegetation: A Discrete Approach," *IEEE Transactions on Geoscience and Remote Sensing*, vol. GE-21, no. 1, pp. 62–71, 1983.
- [54] D. M. LeVine, R. Meneghini, R. H. Lang, and S. S. Seker, "Scattering from arbitrarily oriented dielectric disks in the physical optics regime," *Journal of the Optical Society of America*, vol. 73, no. 10, pp. 1255–1262, 1983.
- [55] R. H. Lang, S. S. Seker, and D. M. LeVine, "Vector solution for the mean electromagnetic fields in a layer of random particles," *Radio Science*, vol. 21, no. 5, pp. 771–786, 1986.
- [56] S. Seker, "EM propagation and backscattering discrete model for medium of sparsely distributed lossy random particles," *AEÜ - International Journal of Electronics and Communications*, vol. 61, no. 6, pp. 377–387, 2007.
- [57] L. Tsang, J. A. Kong, K. Ding, and C. O. Ao, *Scattering of Electromagnetic Waves: Numerical Simulations*, vol. 2, Wiley, New York, NY, USA, 1st edition, 2001.

- [58] C. F. Smith, A. F. Peterson, and R. Mittra, "The Biconjugate Gradient Method for Electromagnetic Scattering," *IEEE Transactions on Antennas and Propagation*, vol. 38, no. 6, pp. 938–940, 1990.
- [59] F. Chen, "The numerical calculation of two-dimensional rough surface scattering by the conjugate gradient method," *International Journal of Remote Sensing*, vol. 17, no. 4, pp. 801–808, 1996.
- [60] B. Babaoglu, A. Altintas, and V. B. Ertürk, "Spectrally accelerated biconjugate gradient stabilized method for scattering from and propagation over electrically large inhomogeneous geometries," *Microwave and Optical Technology Letters*, vol. 46, no. 2, pp. 158–162, 2005.
- [61] J. C. West and J. M. Sturm, "On iterative approaches for electromagnetic rough-surface scattering problems," *IEEE Transactions on Antennas and Propagation*, vol. 47, no. 8, pp. 1281–1288, 1999.
- [62] L. Zhang, G. G. Pan, and J. A. Jones Jr, "On unified numerical algorithm for 3-d scattering from dielectric and pec random rough surfaces," *IEEE Transactions on Antennas and Propagation*, vol. 65, no. 5, pp. 2615–2623, 2017.
- [63] D. M. Young, *Iterative Solution of Large Linear Systems*, Academic Press, New York, NY, USA, 1971.
- [64] E. G. Liszka and J. J. McCoy, "Scattering at a rough boundary—extensions of the Kirchhoff approximation," *The Journal of the Acoustical Society of America*, vol. 71, no. 5, pp. 1093–1100, 1982.
- [65] D. A. Kapp and G. S. Brown, "A new numerical method for rough-surface scattering calculations," *IEEE Transactions on Antennas and Propagation*, vol. 44, no. 5, pp. 711–721, 1996.
- [66] D. Holliday, L. L. Deraad Jr., and G. J. St-Cyr, "Forward-backward: A new method for computing low-grazing angle scattering," *IEEE Transactions on Antennas and Propagation*, vol. 44, no. 5, pp. 722–729, 1996.
- [67] A. Iodice, "Forward-backward method for scattering from dielectric rough surfaces," *IEEE Transactions on Antennas and Propagation*, vol. 50, no. 7, pp. 901–911, 2002.
- [68] A. Iodice, "Scattering from natural soils modeled by dielectric fractal profiles: The forward-backward approach," *IEEE Transactions on Geoscience and Remote Sensing*, vol. 42, no. 1, pp. 77–85, 2004.
- [69] K. Inan and V. B. Ertürk, "Application of iterative techniques for electromagnetic scattering from dielectric random and reentrant rough surfaces," *IEEE Transactions on Geoscience and Remote Sensing*, vol. 44, no. 11, pp. 3320–3329, 2006.
- [70] P. Tran, "Calculation of the scattering electromagnetic waves from a two-dimensional perfectly conducting surface using the method of ordered multiple interactions," *Waves Random Media*, vol. 7, no. 3, pp. 295–302, 1997.
- [71] L. Tsang, C. H. Chan, K. Pak, and H. Sangani, "Monte Carlo simulations of large-scale problems of random rough surface scattering and applications to grazing incidence with the BMIA/canonical grid method," *IEEE Transactions on Antennas and Propagation*, vol. 43, no. 8, pp. 851–859, 1995.
- [72] H.-T. Chou and J. T. Johnson, "A novel acceleration algorithm for the computation of scattering from rough surfaces with the forward-backward method," *Radio Science*, vol. 33, no. 5, pp. 1277–1287, 1998.
- [73] J. Von Hagen and W. Wiesbeck, "Physics-based preconditioner for iterative algorithms in MoM-problems," *IEEE Transactions on Antennas and Propagation*, vol. 50, no. 9, pp. 1315–1316, 2002.
- [74] C. D. Moss, T. M. Grzegorczyk, H. . Han, and J. A. Kong, "Forward-backward method with spectral acceleration for scattering from layered rough surfaces," *IEEE Transactions on Antennas and Propagation*, vol. 54, no. 3, pp. 1006–1016, 2006.
- [75] Y. Ren, Y. Chen, Q. Zhan, J. Niu, and Q. H. Liu, "A higher order hybrid SIE/FEM/SEM method for the flexible electromagnetic simulation in layered medium," *IEEE Transactions on Geoscience and Remote Sensing*, vol. 55, no. 5, pp. 2563–2574, 2017.
- [76] C.-H. Kuo and M. Moghaddam, "Scattering from multilayer rough surfaces based on the extended boundary condition method and truncated singular value decomposition," *IEEE Transactions on Antennas and Propagation*, vol. 54, no. 10, pp. 2917–2929, 2006.
- [77] N. Déchamps and C. Bourlier, "Electromagnetic scattering from a rough layer: propagation-inside-layer expansion method combined to an updated BMIA/CAG approach," *IEEE Transactions on Antennas and Propagation*, vol. 55, no. 10, pp. 2790–2802, 2007.
- [78] N. Déchamps and C. Bourlier, "Electromagnetic scattering from a rough layer: Propagation-inside-layer expansion method combined to the forward-backward novel spectral acceleration," *IEEE Transactions on Antennas and Propagation*, vol. 55, no. 12, pp. 3576–3586, 2007.
- [79] N. Déchamps, N. de Beaujoudrey, C. Bourlier, and S. Toutain, "Fast numerical method for electromagnetic scattering by rough layered interfaces: propagation-inside-layer expansion method," *Journal of the Optical Society of America A: Optics, Image Science & Vision*, vol. 23, no. 2, pp. 359–369, 2006.
- [80] C. Bourlier, N. Pinel, and G. Kubické, *Method of Moments for 2-D Scattering Problems. Basic Concepts and Applications*, Wiley – Focus Series, 2013.
- [81] C. Bourlier, C. Le Bastard, and V. Baltazart, "Generalization of PILE Method to the em Scattering from Stratified Subsurface with Rough Interlayers: Application to the Detection of Debondings Within Pavement Structure," *IEEE Transactions on Geoscience and Remote Sensing*, vol. 53, no. 7, pp. 4104–4115, 2015.
- [82] A. J. Poggio and E. K. Miller, "Integral equation solution of three-dimensional scattering problems," in *Computer Techniques for Electromagnetics*, chapter 4, Pergamon, New York, NY, USA, 1973.
- [83] M. F. Chen and S. Y. Bai, "Computer simulation of wave scattering from a dielectric random surface in two dimensions-cylindrical case," *Journal of Electromagnetic Waves and Applications*, vol. 4, no. 10, pp. 963–982, 1990.
- [84] S. M. Rao, D. R. Wilton, and A. W. Glisson, "Electromagnetic scattering by surfaces of arbitrary shape," *IEEE Transactions on Antennas and Propagation*, vol. 30, no. 3, pp. 409–412, 1982.
- [85] D. Zahn, K. Sarabandi, K. F. Sabet, and J. F. Harvey, "Numerical simulation of scattering from rough surfaces: A wavelet-based approach," *IEEE Transactions on Antennas and Propagation*, vol. 48, no. 2, pp. 246–253, 2000.
- [86] G. W. Pan, K. Wang, and D. Cochran, "Coifman wavelets in 3-D scattering from very rough random surfaces," *IEEE Transactions on Antennas and Propagation*, vol. 52, no. 11, pp. 3096–3103, 2004.
- [87] G. G. Pan, M. Jin, L. Zhang, M. Bai, and J. Miao, "An efficient scattering algorithm for smooth and sharp surfaces: Coiflet-based scalar MFIE," *IEEE Transactions on Antennas and Propagation*, vol. 62, no. 8, pp. 4241–4250, 2014.
- [88] D. J. Daniels, *EM Detection of Concealed Targets*, John Wiley & Sons, 2010.
- [89] R. Zoughi, *Microwave Nondestructive Testing and Evaluation*, Kluwer Academic, Amsterdam, The Netherlands, 2000.

- [90] M. Pastorino, *Microwave Imaging*, John Wiley & Sons, Hoboken, NJ, USA, 2010.
- [91] T. M. Habashy and R. Mittra, "On Some Inverse Methods in Electromagnetics," *Journal of Electromagnetic Waves and Applications*, vol. 1, no. 1, pp. 25–58, 1987.
- [92] A. Kumar and M. J. Akhtar, "Microwave imaging of stratified media from band-limited reflection coefficient data," *IEEE Geoscience and Remote Sensing Letters*, vol. 11, no. 7, pp. 1255–1259, 2014.
- [93] M. G. Amin, *Through-the-Wall Radar Imaging*, CRC Press, 2010.
- [94] T. G. Papadopoulos and I. T. Rekanos, "Time-domain microwave imaging of inhomogeneous Debye dispersive scatterers," *IEEE Transactions on Antennas and Propagation*, vol. 60, no. 2, part 2, pp. 1197–1202, 2012.
- [95] A. Franchois and C. Pichot, "Microwave imaging-complex permittivity reconstruction with a levenberg-marquardt method," *IEEE Transactions on Antennas and Propagation*, vol. 45, no. 2, pp. 203–215, 1997.
- [96] C. Estatico, A. Fedeli, M. Pastorino, and A. Randazzo, "A multi-frequency inexact-Newton method in L^p banach spaces for buried objects detection," *IEEE Transactions on Antennas and Propagation*, vol. 63, no. 9, pp. 4198–4204, 2015.
- [97] E. J. Bond, X. Li, S. C. Hagness, and B. D. Van Veen, "Microwave imaging via space-time beamforming for early detection of breast cancer," *IEEE Transactions on Antennas and Propagation*, vol. 51, no. 8, pp. 1690–1705, 2003.
- [98] X. Li, E. J. Bond, B. D. Van Veen, and S. C. Hagness, "An overview of ultra-wideband microwave imaging via space-time beamforming for early-stage breast-cancer detection," *IEEE Antennas and Propagation Magazine*, vol. 47, no. 1, pp. 19–34, 2005.
- [99] I. Catapano, A. Randazzo, E. Slob, and R. Solimene, "GPR imaging via qualitative and quantitative approaches," in *Civil Engineering Applications of Ground Penetrating Radar*, A. Benedetto and L. Pajewski, Eds., pp. 239–280, Springer, Cham, Switzerland, 2015.
- [100] L. Guo and A. M. Abbosh, "Microwave stepped frequency head imaging using compressive sensing with limited number of frequency steps," *IEEE Antennas and Wireless Propagation Letters*, vol. 14, pp. 1133–1136, 2015.
- [101] M. Pastorino, "Stochastic optimization methods applied to microwave imaging: A review," *IEEE Transactions on Antennas and Propagation*, vol. 55, no. 3 I, pp. 538–548, 2007.
- [102] P. M. van den Berg and A. Abubakar, "Contrast source inversion method: State of art," *Progress in Electromagnetics Research*, vol. 34, pp. 189–218, 2001.
- [103] C. Tai, *Dyadic Green Functions in Electromagnetic Theory*, IEEE Press, Piscataway, NJ, USA, 1994.
- [104] R. Maini, M. F. Iskander, and C. H. Durney, "On the electromagnetic imaging using linear reconstruction techniques," *Proceedings of the IEEE*, vol. 68, no. 12, pp. 1550–1552, 1980.
- [105] C. Estatico, M. Pastorino, and A. Randazzo, "An inexact-Newton method for short-range microwave imaging within the second-order born approximation," *IEEE Transactions on Geoscience and Remote Sensing*, vol. 43, no. 11, pp. 2593–2605, 2005.
- [106] S. Caorsi, A. Massa, and M. Pastorino, "Rytov approximation: Application to scattering by two-dimensional weakly nonlinear dielectrics," *Journal of the Optical Society of America A: Optics and Image Science, and Vision*, vol. 13, no. 3, pp. 509–516, 1996.
- [107] W. C. Chew and Y. M. Wang, "Reconstruction of two-dimensional permittivity distribution using the distorted Born iterative method," *IEEE Transactions on Medical Imaging*, vol. 9, no. 2, pp. 218–225, 1990.
- [108] D. Colton and R. Kress, *Inverse Acoustic and Electromagnetic Scattering Theory*, Springer, New York, NY, USA, 2013.
- [109] M. Brignone, G. Bozza, A. Randazzo, M. Piana, and M. Pastorino, "A hybrid approach to 3D microwave imaging by using linear sampling and ant colony optimization," *IEEE Transactions on Antennas and Propagation*, vol. 56, no. 10, pp. 3224–3232, 2008.
- [110] M. N. Stevanović, L. Crocco, A. R. Djordjević, and A. Nehorai, "Higher order sparse microwave imaging of PEC scatterers," *IEEE Transactions on Antennas and Propagation*, vol. 64, no. 3, pp. 988–997, 2016.
- [111] J. Shen, Y. Zhong, X. Chen, and L. Ran, "Inverse scattering problems of reconstructing perfectly electric conductors with TE illumination," *IEEE Transactions on Antennas and Propagation*, vol. 61, no. 9, pp. 4713–4721, 2013.
- [112] C. Estatico, M. Pastorino, and A. Randazzo, "A Novel Microwave Imaging Approach Based on Regularization in L^p Banach Spaces," *IEEE Transactions on Antennas and Propagation*, vol. 60, no. 7, pp. 3373–3381, 2012.
- [113] C. Estatico, A. Fedeli, M. Pastorino, and A. Randazzo, "Buried object detection by means of a L^p Banach-space inversion procedure," *Radio Science*, vol. 50, no. 1, pp. 41–51, 2015.
- [114] M. Bevacqua, L. Crocco, L. Di Donato, T. Isernia, and R. Palmeri, "Exploiting sparsity and field conditioning in subsurface microwave imaging of nonweak buried targets," *Radio Science*, vol. 51, no. 4, pp. 301–310, 2016.
- [115] A. Massa, P. Rocca, and G. Oliveri, "Compressive sensing in electromagnetics—a review," *IEEE Antennas and Propagation Magazine*, vol. 57, no. 1, pp. 224–238, 2015.
- [116] J. J. Bowman, T. B. A. Senior, and P. L. E. Uslenghi, *Electromagnetic and Acoustic Scattering by Simple Shapes*, North-Holland, Amsterdam, The Netherlands, 1969.
- [117] M. Pastorino, M. Raffetto, and A. Randazzo, "Electromagnetic inverse scattering of axially moving cylindrical targets," *IEEE Transactions on Geoscience and Remote Sensing*, vol. 53, no. 3, pp. 1452–1462, 2015.
- [118] M. Pastorino, M. Raffetto, and A. Randazzo, "Two-dimensional Green's function for scattering and radiation problems in elliptically-layered media," *IEEE Transactions on Antennas and Propagation*, vol. 62, no. 4, part 2, pp. 2071–2080, 2014.

Research Article

Application of a Sparsity Pattern and Region Clustering for Near Field Sparse Approximate Inverse Preconditioners in Method of Moments Simulations

Carlos Delgado,¹ Javier Moreno,² and Felipe Cátedra¹

¹Computer Science Department, University of Alcalá, Madrid, Spain

²NewFasant S.L., Guadalajara, Spain

Correspondence should be addressed to Carlos Delgado; carlos.delgado@uah.es

Received 18 May 2017; Revised 28 September 2017; Accepted 8 October 2017; Published 31 October 2017

Academic Editor: Nicolas Pinel

Copyright © 2017 Carlos Delgado et al. This is an open access article distributed under the Creative Commons Attribution License, which permits unrestricted use, distribution, and reproduction in any medium, provided the original work is properly cited.

This document presents a technique for the generation of Sparse Inverse Preconditioners based on the near field coupling matrices of Method of Moments simulations where the geometry has been partitioned in terms of regions. A distance parameter is used to determine the sparsity pattern of the preconditioner. The rows of the preconditioner are computed in groups at a time, according to the number of unknowns contained in each region of the geometry. Two filtering thresholds allow considering only the coupling terms with a significant weight for a faster generation of the preconditioner and storing only the most significant preconditioner coefficients in order to decrease the memory required. The generation of the preconditioner involves the computation of as many independent linear least square problems as the number of regions in which the geometry is partitioned, resulting in very good scalability properties regarding its parallelization.

1. Introduction

Many of the modern approaches for electromagnetic analysis based on the Method of Moments (MoM) [1] rely on the idea of only storing the near field coupling terms of the impedance matrix, which typically extends about one-quarter of the wavelength under analysis. The coupling effects between distant parts of the geometry are taken into account in the matrix-vector product computation as a part of the iterative solution process, and the specific manner in which this is carried out depends on each approach. Some popular schemes are based on the use of the Multilevel Fast Multipole Algorithm (MLFMA) [2], which includes the processes of aggregation, translation, and disaggregation of multipole expansions in the computation of such products. Other schemes use matrix compression techniques [3, 4] to compute these multiplications efficiently. All these methods circumvent the burden of storing the full MoM matrix, which would easily surpass the memory capacity and cripple the efficiency for the analysis of even moderately sized problems.

Since the full coupling matrix is no longer to be calculated and due to the size of the system to be computed, iterative solvers play a major role in modern simulation methods, although it is worthwhile to mention that some approaches extend the range in which direct solvers can be applied, such as those based on the use of Macro Basis functions [5], which reduce the number of unknowns of the original problem. The necessity of iteration, however, is unavoidable for electrically large or very large problems and with the use of iterative solvers arises the problem of slow convergence for some cases, due to reasons of different nature, such as geometrical features of the model, multiscale problems, or to the intrinsic electromagnetic behavior, such as the presence of resonant regions within the geometry. In any case the use of preconditioners is very important in order to ease the iterative process, which, in many cases, accounts for most of the total simulation time.

It is noteworthy to mention a family of preconditioners that are based on the physical properties of the problem and more specifically on the idea that inverse matrix that is approximately represented by the preconditioner is

essentially an approximate solution of the electromagnetic problem. Previous works have been published for the efficient generation of physical-based preconditioners considering quasiplanar structures [6] or exploiting the quasiplanar electromagnetic behavior of conducting rough surfaces [7]. A method for the generation of a preconditioner for problems involving multiple scatterers, based on splitting the system matrix according to the types of material of the subdomains as well as currents on different parts, is shown in [8].

Another group of preconditioners that are also commonly used in the context mentioned above rely on the numerical manipulation of the system matrix rather than on physical properties of the problem under analysis. The Incomplete LU (ILU) decomposition [9–11] and the Sparse Approximate Inverse (SAI) [12–14] show a good behavior and are extensively used at the present time. The ILU preconditioner is considered slightly more efficient for the same amount of data [15], although the SAI approach is much more scalable, since it can be computed by solving independent linear least square (LLS) systems that generate the rows of the preconditioner. This property renders the SAI preconditioner very well suited to be used in very large problems that require a fair number of processing nodes. It should be noted, however, that modern ILU preconditioners based on multifrontal/multilevel schemes allow better performance than the conventional ILU approach while offering a good compromise between robustness and efficiency [16–18]. The application of multilevel ILU preconditioning techniques applied to electromagnetic problems involving the Electric Field Integral Equation has been documented in [19].

The preconditioners based on the ILU and SAI approaches are often generated considering only the near field part of the coupling matrix, which includes the strongest interactions between basis and testing functions. This allows a fast generation and reasonably reduced size, although the performance of such preconditioners may be lacking in the analysis of problems in which there are strong interactions between parts of the geometry that are physically distant, like the interaction between the feed of a reflector antenna and the main reflector or between parts of certain cavities.

The most common approach in the application of the SAI preconditioner involves the definition of a sparsity pattern, understood as the pattern of the elements of the preconditioner that are not null, which is the same as that of the near field coupling matrix [12]. In this work we propose an improved strategy based on the clustering of the least squares systems that fall under each near field region as well as a distance threshold parameter that allows a finer control of the sparsity pattern of the SAI preconditioner. We have obtained noticeable improvements on the convergence properties of the conventional use of the SAI preconditioner compared to the approach described here. Illustrative examples are given in the Numerical Results.

2. Description of the Approach

The application of the MoM is based on the solution of a linear system of equations as follows:

$$[Z][J] = [V], \quad (1)$$

where $[J]$ and $[V]$ are the current coefficient and the excitation vectors, respectively, and matrix $[Z]$ contains the coupling terms between each basis function and each testing function of the problem. The expression of term (i, j) of $[Z]$ can be written as

$$Z_{i,j} = \langle L(B_j), T_i \rangle, \quad (2)$$

where it is computed as the inner product of the i th testing function T_i and the field radiated by the j th active basis function B_j over the i th subdomain. This field is given by the operator $L(B_j)$. Consequently, each row of matrix $[Z]$ represents the coupling terms between all the active basis functions of the geometry and one passive testing function and, in turn, a column of $[Z]$ contains the coupling terms between one active basis function and all the passive testing functions. Since $[Z]$ is dense and unmanageable for many realistic problems it is very common to compartmentalize the original geometry into regions and only calculate and store the coupling terms of the basis and testing functions contained within the same region, as well as those contained within adjacent regions. The typical region size is about $\lambda/4$, which makes the matrix containing such terms, denoted as $[Z_{\text{NF}}]$ in this work, sparse and with a much more manageable size even for large problems. The rest of the coupling terms, noticeably weaker, are contained in the far field coupling matrix $[Z_{\text{FF}}]$. Many modern efficient numerical methods do not require calculating the far field coupling matrix [2–4] and consider those interactions using alternative approaches.

In order to incorporate the near field preconditioning scheme proposed in the present work, it is useful to write the MoM equation separating the coupling matrix into the near field term ($[Z_{\text{NF}}]$) and the far field term ($[Z_{\text{FF}}]$) as shown as follows:

$$[M]([Z_{\text{NF}}] + [Z_{\text{FF}}])[J] = [M][V], \quad (3)$$

where $[M]$ is the preconditioner. This matrix should ideally be as close as possible to the inverse of $[Z] = [Z_{\text{NF}}] + [Z_{\text{FF}}]$. However, it is very important to keep the generation procedure scalable and efficient both in terms of size and CPU time.

Under the assumption that the near field part of the coupling matrix is stronger than the far field term, it is possible to rewrite (3) in the following fashion:

$$[M][Z_{\text{NF}}][J] \approx [M][V]. \quad (4)$$

2.1. Region Clustering in the Generation of the Preconditioner. A commonly used SAI preconditioner relies on the generation of $[M]$ by minimizing the *Frobenius norm* of $\{|I| - [M][Z_{\text{NF}}]\}$, where $|I|$ is the identity matrix. The scalability properties of this preconditioner arise from the possibility of decomposing such expression into the minimization of the norm of the difference between each row of the identity

matrix and the preconditioner multiplied by the near field coupling matrix as follows:

$$\min \| [I] - [M] [Z_{\text{NF}}] \|_F^2 = \sum_{k=1}^n \min \| \mathbf{e}_k - \mathbf{m}_k [Z_{\text{NF}}] \|_2^2, \quad (5)$$

where n indicates the total number of basis functions of the problem, \mathbf{e}_k stands for the k th row of the identity matrix, and \mathbf{m}_k denotes the k th row of the preconditioner $[M]$.

It should be remarked that the technique described in this work relies on the compartmentalization of the computational space in terms of *regions*, so that only the coupling terms between subdomain functions located in the same or in adjacent regions are to be computed. This is a widely adopted scheme by many modern methods. Under this context, it is possible to take advantage of the reutilization of the same LLS matrix to obtain as many rows of the preconditioner as the number of the unknowns contained in each region. This can be illustrated by rewriting (5) in the following manner:

$$\begin{aligned} & \sum_{k=1}^n \min \| \mathbf{e}_k - \mathbf{m}_k [Z_{\text{NF}}] \|_2^2 \\ &= \sum_{r=1}^R \min \| [I_r] - [M_r] [Z_{\text{NF}}] \|_F^2, \end{aligned} \quad (6)$$

where R indicates the total number of regions of the problem. Considering at this point that N_i is the number of subdomain functions contained in region i and that S_i^r represents the absolute index of the i th subdomain contained in region r , the $[I_r]$ matrix in (6) consists of N_r rows of the unit matrix

$$[I_r] = \begin{bmatrix} \mathbf{e}_{S_1^r} \\ \vdots \\ \mathbf{e}_{S_{N_r}^r} \end{bmatrix} \quad (7)$$

and, analogously, $[M_r]$ contains N_r rows of the preconditioner:

$$[M_r] = \begin{bmatrix} \mathbf{m}_{S_1^r} \\ \vdots \\ \mathbf{m}_{S_{N_r}^r} \end{bmatrix}. \quad (8)$$

2.2. Parametric Sparsity Pattern. Noting that $[M_r]$ will be generally a full matrix it is necessary to define a sparsity pattern that enforces null values for some of its coefficients.

It is common to see approaches in the literature that consider such a sparsity pattern to be identical as that of the original near field coupling matrix [12]. We introduce an alternative approach by defining in this context the *sparsity distance parameter* ξ as the distance threshold that determines whether the subdomains contained in a region are to be included in the sparsity pattern. Let us denote for this purpose R_i as the region in which subdomain i is contained and $D(R_i, R_j)$ as the distance between the centres of regions R_i and R_j , where i and j are two arbitrary subdomains. The sparsity mask matrix for region r is defined as

$$[\Omega]_r^\xi = \begin{bmatrix} \Omega_{1,1} & \cdots & \Omega_{1,n} \\ \vdots & \ddots & \vdots \\ \Omega_{n,1} & \cdots & \Omega_{n,n} \end{bmatrix},$$

where $\Omega_{i,j} = \begin{cases} 1, & \text{if } D(R_i, R_j) \leq \xi \\ 0, & \text{if } D(R_i, R_j) > \xi. \end{cases}$

The $[\Omega]_r^\xi$ matrix, applied for all the regions, defines the sparsity pattern used to generate the preconditioner. With this consideration, the right hand side of expression (6) can be approximated as

$$\begin{aligned} & \sum_{r=1}^R \min \| [I_r] - [M_r] [Z_{\text{NF}}] \|_F^2 \\ & \cong \sum_{r=1}^R \min \| [\tilde{I}_r] - [\widetilde{M}_r] [\widetilde{Z}_{\text{NF}}] \|_F^2, \end{aligned} \quad (10)$$

where $[\widetilde{M}_r]$ is an approximation of $[M_r]$ obtained as the solution of the LLS where the matrices marked with the tilde overscore denote the application of the sparsity pattern by computing the Hadamard product with the *sparsity mask* and eliminating the null rows and columns of the result:

$$\begin{aligned} [\widetilde{I}_r] &= \mathbb{N} \left([\Omega]_r^\xi \odot [I_r] \right), \\ [\widetilde{Z}_{\text{NF}}] &= \mathbb{N} \left([\Omega]_r^\xi \odot \square_r^\tau ([Z_{\text{NF}}]) \right). \end{aligned} \quad (11)$$

In this expression \odot denotes the element-wise matrix multiplication operator and $\mathbb{N}([A])$ represents the matrix that results from the elimination of the null rows and columns of $[A]$. The term $\square_r^\tau([Z_{\text{NF}}])$, in turn, is an operator that returns a filtered version of $[Z_{\text{NF}}]$ discarding the coefficients with a module lower than τ times the largest self-impedance in the region where they belong. The τ parameter, named *preprocessing threshold parameter* through the rest of this document, allows a reduction of the size of the LLS problems to be solved for the generation of the preconditioner by eliminating low-magnitude rows and columns, resulting in faster computation. Considering these comments $\square_r^\tau([Z_{\text{NF}}])$ can be written as follows:

$$\Xi_r^\tau([Z_{\text{NF}}]) = \begin{bmatrix} \Xi_{1,1} & \cdots & \Xi_{1,n} \\ \vdots & \ddots & \vdots \\ \Xi_{n,1} & \cdots & \Xi_{n,n} \end{bmatrix},$$

with $0 \leq \tau \leq 1$, where $\Xi_{i,j} = \begin{cases} 0, & \text{if } |[Z_{\text{NF}}]_{i,j}| \leq \tau \cdot \max(|[Z_{\text{NF}}]_{k,k}|) \text{ with } k \in \text{Region } r \\ [Z_{\text{NF}}]_{i,j}, & \text{if } |[Z_{\text{NF}}]_{i,j}| > \tau \cdot \max(|[Z_{\text{NF}}]_{k,k}|) \text{ with } k \in \text{Region } r. \end{cases}$

(12)

The preconditioner, therefore, can be computed by calculating the result of R independent LLS problems, which can be distributed among an arbitrary number of processing nodes, and assembling the preconditioner using the partial $[\widetilde{M}_r]$ matrices. It is convenient, however, to filter these results to retain only the elements that pose a significant weight for each row of the preconditioner. Experimental results have shown that for typical applications the size of the preconditioner can be reduced at least by an order of magnitude without a compromise in the convergence performance. Expression

$$\Psi^\zeta([\widetilde{M}_r]) = \begin{bmatrix} \Psi_{1,1} & \cdots & \Psi_{1,n} \\ \vdots & \ddots & \vdots \\ \Psi_{n,1} & \cdots & \Psi_{n,n} \end{bmatrix}, \quad \text{where } \Psi_{i,j} = \begin{cases} 0, & \text{if } |[\widetilde{M}_r]_{i,j}| \leq \zeta \cdot \max(|[\widetilde{M}_r]_{i,j}|) \text{ within row } i \\ [\widetilde{M}_r]_{i,j}, & \text{if } |[\widetilde{M}_r]_{i,j}| > \zeta \cdot \max(|[\widetilde{M}_r]_{i,j}|) \text{ within row } i. \end{cases}$$
(14)

The sparsity distance parameter ξ introduced in this section allows a fine control of the size of the preconditioning matrix. Large values (similar to the size of the geometry) imply no restrictions in the sparsity pattern of the resulting preconditioner, which can lead to the computation of the exact inverse of $[Z_{\text{NF}}]$ with a prohibitive computational cost. Low values, around the size of the regions in which the geometry has been previously partitioned, render an approximate inverse with the same size as $[Z_{\text{NF}}]$ that can be computed fast. These sizes can then be modified by the filtering threshold ζ that discards the least significant terms. Our experience, as shown in the next section, shows that sparsity distance parameter values ranging from 0.5λ to λ present a good tradeoff between size and performance.

3. Numerical Results

Some test cases have been selected in this section in order to illustrate the performance of the approach described in the present document. All the simulations have been run on an HP Z820 workstation using 16 Intel Xeon E5-2660 2.2 GHz processing cores and 128 GB of RAM. In all the cases we have applied the Method of Moments combined with the Multilevel Fast Multipole Algorithm using 0.25λ as the region size unless otherwise indicated. The SAI preconditioners have been obtained distributing the computation of $[\widetilde{M}_r]$ shown in expression (13) for all the regions of the

(12) illustrates the row filtering of $[\widetilde{M}_r]$ introducing the *postprocessing threshold parameter* ζ :

$$[\widetilde{\widetilde{M}}_r] = \Psi^\zeta([\widetilde{M}_r]), \quad \text{with } 0 \leq \zeta \leq 1,$$
(13)

where $\Psi^\zeta([\widetilde{M}_r])$ retains the elements with an absolute value over ζ times the largest element in each row of the preconditioner:

problem between the computing nodes using the OpenMP paradigm [20]. The Generalized Minimal Residual (GMRES) iterative solver [21] with a restart parameter of 300 has been used for all the simulations presented in this section. The parallelization scheme of the SAI preconditioner followed in the simulations shown in this section consists of a loop that iterates over the regions in which the geometry has been previously partitioned. For each iteration the corresponding LLS matrix is assembled and the LAPACK numerical library [22] is used to obtain the solution. Since we use OpenMP to merely distribute the iterations of this loop over all the processing nodes, it is extremely important that the iterations are independent of each other, as is the case for the proposed preconditioner.

In the results presented in this section θ represents the polar angle measured from the z -axis and ϕ denotes the azimuthal angle measured from the x -axis, with $0^\circ \leq \theta \leq 180^\circ$, $0^\circ \leq \phi < 360^\circ$. These angular coordinates have been illustrated in Figure 1 for the sake of clarification.

Figure 2 depicts the geometry of the PLACYL case, originally proposed for the JINA EM 2006 workshop [23], consisting of a cylinder with a radius of 0.2 m and a length of 1 m connected to a semispherical surface on one side and located on top of a plane plate that extends 1.8 m along the X direction and 1.2 m along the Y direction. The gap between the cylinder and the plate is 0.02 m. The monostatic RCS of this setup has been computed at a frequency of 10 GHz for

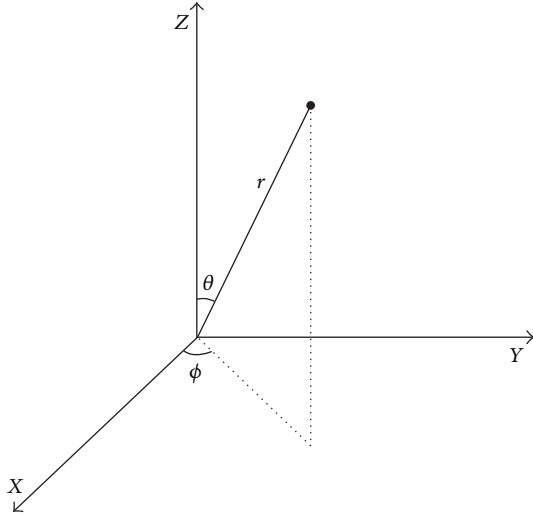


FIGURE 1: Depiction of the spherical coordinates considered.

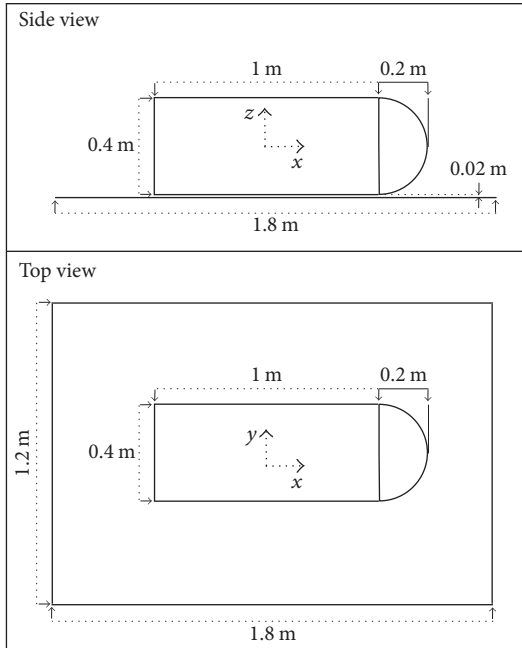
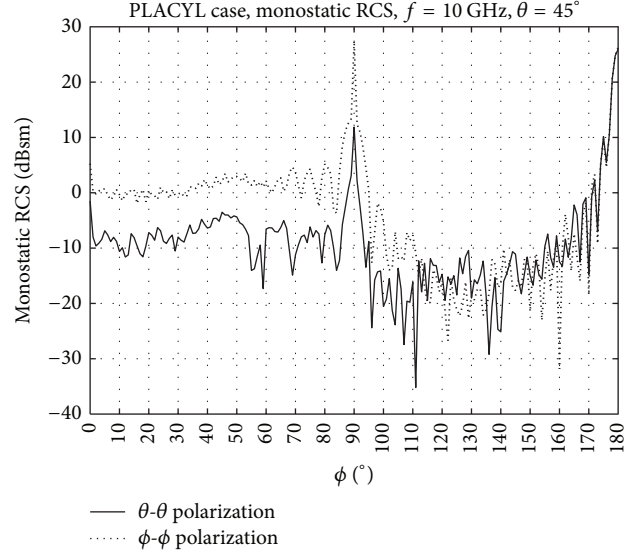


FIGURE 2: Geometrical model of the PLACYL case.

a set of 181 theta polarized incident waves corresponding to the directions given by $\theta = 45^\circ$ and ϕ ranging from 0° to 180° . The electrical length of the cylinder at this frequency is 40λ and the radius is 6.67λ , while the plate is 60λ long and 40λ wide. The Electric Field Integral Equation (EFIE) formulation has been considered for all the surfaces of this case instead of the Combined Field Integral Equation (CFIE) in order to obtain a moderately ill-conditioned problem useful to test the performance of the preconditioners. The geometry has been meshed using a sampling rate of 10 divisions per wavelength, resulting 831,734 unknowns, and the compartmentalization of the geometry has generated 73,590 regions. The iteration error threshold of the GMRES solver has been 10^{-3} . Figure 3

FIGURE 3: Monostatic RCS results for the PLACYL case, $f = 10$ GHz.

shows the results obtained for this case. Table 1 shows the CPU time required for the generation of the preconditioner as well as the memory for its storage considering different configurations and the average number of iterations per monostatic direction necessary to compute the solution. The values of the SAI parameters (sparsity distance ξ , preprocessing threshold τ , and postprocessing threshold ζ) defined in the approach presented in this work are also included in the table.

The results plotted in Figure 3 show that there is a certain amount of specular reflection on the hemisphere and between the hemisphere and the plate at $\phi = 0^\circ$ that provides a RCS level that fades in a very narrow angular margin. The convergence for this direction is not especially slow because of the predominant specular effect over the high-order coupling reflections between plate and hemisphere. From $\phi = 0^\circ$ to $\phi = 90^\circ$ the backscattering RCS contributions are due to diffuse reflections on the plate, cylinder, and high-order effects between both bodies, leading to slow convergence due to the low RCS levels and strong coupling. The RCS increases very noticeably for angular values around $\phi = 90^\circ$, due to the larger cross section of the cylinder that provides specular reflection, as well as the high-order specular reflections between the side of the cylinder and the plate and creeping effects on the cylinder. From $\phi = 90^\circ$ to $\phi = 180^\circ$ the contribution of the interaction between the flat part of the cylinder and the plate becomes increasingly stronger and for the angular margin around $\phi = 180^\circ$ the double reflection between the plate and the flat cap of the cylinder is overwhelmingly predominant, yielding high RCS values and easing the convergence rate.

It can be seen in Table 1 that the memory requirements for the storage of the preconditioner have a weak dependency on the sparsity distance parameter ξ . This is due to the use of the postprocessing threshold ζ that eliminates the least significant terms of the preconditioner. In general, it is normal to see a mild increase of the size of the preconditioner as ξ increases

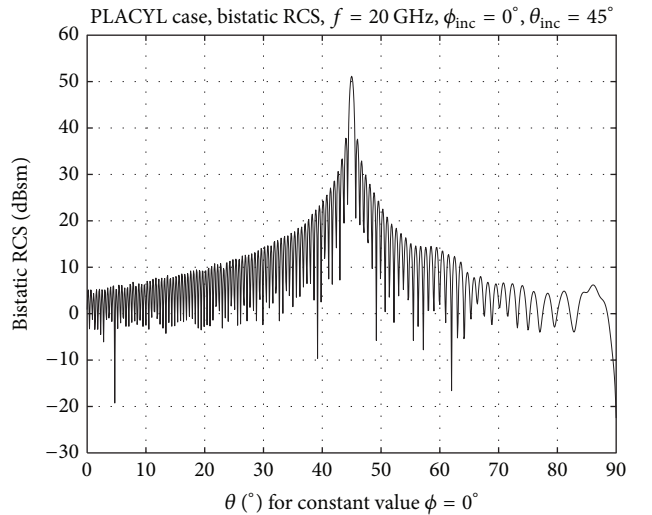
TABLE 1: Convergence performance for several SAI parameters.

	Precond. generation time (s)	Precond. size (MB)	Avg. number of iterations per direction (θ pol.)	Avg. number of iterations per direction (ϕ pol.)
No preconditioner	—	—	394.15	332.42
Conventional SAI	189	378.43	192.00	172.05
Proposed SAI	43	284.57	181.94	158.73
Sparsity distance (ξ) = 0.25λ				
Preprocessing threshold (τ) = 0.03				
Postprocessing threshold (ς) = 0.03				
Proposed SAI	192	281.78	129.81	115.98
Sparsity distance (ξ) = 0.5λ				
Preprocessing threshold (τ) = 0.03				
Postprocessing threshold (ς) = 0.03				
Proposed SAI	1208	304.33	111.78	103.21
Sparsity distance (ξ) = λ				
Preprocessing threshold (τ) = 0.03				
Postprocessing threshold (ς) = 0.03				

because, as more coefficients are included in the sparsity pattern of the preconditioner, a number of them are probably going to have a magnitude that exceeds the threshold, adding information to the computed preconditioner.

In addition to the monostatic results shown above, it is interesting to test the behavior of the convergence of the proposed approach for a different number of configurations. For the next example we have considered the PLACYL geometry increasing the frequency to 20 GHz, resulting in an electrical length of 80λ for the cylinder with a radius of 13.35λ and a plate size of $120\lambda \times 80\lambda$. Now the CFIE formulation with parameter $\alpha = 0.5$ has been applied for the closed body (cylinder and semisphere), and the EFIE formulation has been applied for the plane plate. In this case, meshing with the standard rate of 10 samples per wavelength, we obtain 3,358,631 unknowns and 297,132 regions. A bistatic RCS analysis has been performed for the excitation incidence given by $\theta = 45^\circ$ and $\phi = 0^\circ$ with observation directions separated by 0.1° steps between $\theta = 0^\circ$ and $\theta = 90^\circ$. The sparsity distance parameter considered in this case has been $\xi = 0.5\lambda$, and the preprocessing and postprocessing thresholds have been, respectively, $\tau = 0.05$ and $\varsigma = 0.03$. Figure 4 shows the results obtained for the θ -polarized incident field considering an iteration error threshold of 10^{-3} . Figure 5 shows the convergence analysis of this case considering the use of the conventional SAI approach (with the same sparsity pattern as the near field coupling matrix), the SAI approach proposed in this document and without any preconditioner.

For the next example, the RCS of a realistic model of an Opel Astra car has been simulated at a frequency of 5.9 GHz. The geometry is shown in Figure 6 and has been modeled using 282 NURBS surfaces. This case consists of 2,255,500 unknowns and 200,936 regions using a sampling rate of 10 samples per wavelength. In order to analyze a more realistic problem, several surfaces have been treated as dielectric layers, defining their relative permeability ε_r . The windows and lights have been modeled using a thin layer

FIGURE 4: Bistatic RCS results of the PLACYL case, $f = 20$ GHz.

approximation with $\varepsilon_r = 4$. The wheels have been modeled by means of a thin layer approximation using $\varepsilon_r = 7$, and dielectric losses have been introduced by assigning the loss tangent $\tan(\delta) = 0.04$, considering these values as a realistic approach for the rubber compound of the tires [24]. The size of the car is approximately 4.14 meters long, 1.64 meters wide, and 1.35 meters tall, which at the working frequency corresponds to 81.5λ tall, 32.25λ wide, and 26.55λ high. The bistatic RCS has been computed for a θ -polarized plane wave impinging from $\theta = 80^\circ$ and $\phi = 45^\circ$. The observation directions are contained in the $\phi = 45^\circ$ angular cut θ ranging from 0° to 90° in 0.1° steps. The EFIE formulation has been applied, due to the geometrical and material features of this problem. Figure 7 shows the computed results. Convergence has been obtained for an error of 10^{-3} in 281 iterations. Realistic cases often offer a slow convergence due to the more

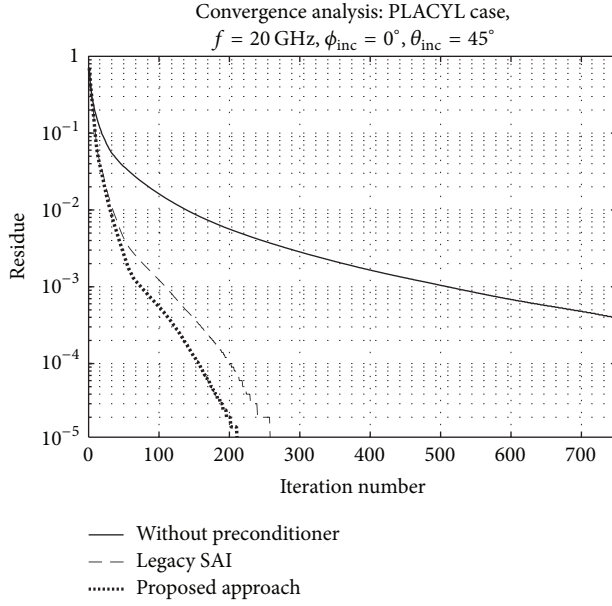
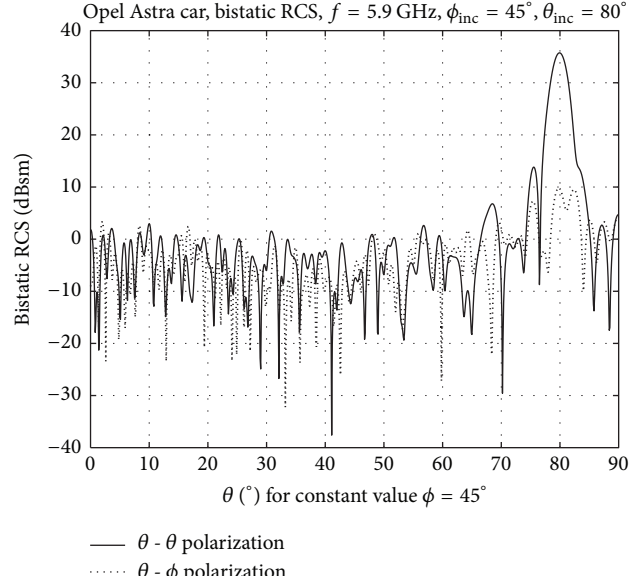
FIGURE 5: Convergence analysis for the PLACYL case, $f = 20 \text{ GHz}$.

FIGURE 6: Geometrical model of an Opel Astra car.

complex geometrical models. The inclusion of very small patches, degenerate surfaces, and other sublambda details produces an irregular mesh that favors slower convergence rates. In addition, the use of dielectric materials assigned to some of the surfaces of the model combined with PEC surfaces in the rest of the body also poses a burden to the convergence properties of the problem. In this case the conventional SAI approach did not reach convergence and stalled with an error value of $2.2 \cdot 10^{-2}$. The conventional SAI preconditioner uses the same sparsity pattern as the near field coupling matrix, which is in essence equivalent to generating the preconditioner using a sparsity distance of $\xi = 0.25 \lambda$ in this case. However, due to the features of this geometrical model the resulting preconditioner does not adequately resemble the inverse of $[Z_{\text{NF}}]$. The extended value of the sparsity distance used with the proposed approach ($\xi = 0.75 \lambda$) allows the computation of a denser preconditioner that provides better convergence. The total simulation time

FIGURE 7: Bistatic RCS results for the Opel Astra car, $f = 5.9 \text{ GHz}$.

has been 18,976 seconds. The preconditioner in this case has been generated with a sparsity distance parameter $\xi = 0.75 \lambda$, a preprocessing threshold $\tau = 5 \cdot 10^{-3}$, and the postprocessing threshold $\zeta = 2 \cdot 10^{-2}$ in 2,220 s and has required 5.9 GB of RAM.

4. Conclusion

A new sparsity pattern and filtering approach that can be used to generate Sparse Approximate Inverse preconditioners considering the near field part for computations based on the Method of Moments have been presented in this document. The rows of the preconditioner are generated as groups that result from the solution of similar least squares problems. In addition, a parametric distance sparsity parameter allows a fine control of the amount of data to be used. The scalability properties of this preconditioner are excellent and make it well suited to solve large and realistic problems with a moderate computing time and RAM footprint. Some illustrative examples have been provided in order to test the performance of the proposed approach.

From the experience gathered by the authors, some recommended typical values of the parameters of the proposed preconditioner can be a sparsity distance ranging between 0.5λ and λ , as well as preprocessing and postprocessing thresholds between 0.01 and 0.03. For those cases with an especially difficult convergence the sparsity distance can be raised up to 2λ at the expense of higher CPU time and memory consumption. In cases where the memory consumption is a critical issue the postprocessing threshold can be increased to values around 0.05 in order to reduce the size of the preconditioner, with the possible consequence of a slightly slower convergence.

Conflicts of Interest

The authors declare that they have no conflicts of interest.

Acknowledgments

This work has been partially supported by the Spanish Ministry of Economy and Competitiveness (Project Ref. TEC 2013-46587-R and Grant Ref. PTQ-14-07060) and by the University of Alcalá (Project Ref. CCG2016/EXP-082).

References

- [1] R. F. Harrington, *Field Computation by Moment Methods*, McMillan, New York, NY, USA, 1968.
- [2] J. M. Song and W. C. Chew, "Multilevel fast-multipole algorithm for solving combined field integral equations of electromagnetic scattering," *Microwave and Optical Technology Letters*, vol. 10, no. 1, pp. 14–19, 1995.
- [3] M. Bebendorf and S. Rjasanow, "Adaptive low-rank approximation of collocation matrices," *Computing: Archives for Scientific Computing*, vol. 70, no. 1, pp. 1–24, 2003.
- [4] K. Zhao, M. N. Vouvakis, and J.-F. Lee, "The adaptive cross approximation algorithm for accelerated method of moments computations of EMC problems," *IEEE Transactions on Electromagnetic Compatibility*, vol. 47, no. 4, pp. 763–773, 2005.
- [5] V. V. S. Prakash and R. Mittra, "Characteristic basis function method: a new technique for efficient solution of method of moments matrix equations," *Microwave and Optical Technology Letters*, vol. 36, no. 2, pp. 95–100, 2003.
- [6] P. Naenna and J. T. Johnson, "A physically-based preconditioner for quasi-planar scattering problems," *Institute of Electrical and Electronics Engineers. Transactions on Antennas and Propagation*, vol. 56, no. 8, part 1, pp. 2421–2426, 2008.
- [7] S. Tournier, P. Borderies, and J.-R. Poirier, "Integral equations physically-based preconditioner for two-dimensional electromagnetic scattering by rough surfaces," *Institute of Electrical and Electronics Engineers. Transactions on Antennas and Propagation*, vol. 59, no. 10, pp. 3764–3771, 2011.
- [8] J. Von Hagen and W. Wiesbeck, "Physics-based preconditioner for iterative algorithms in MoM-problems," *IEEE Transactions on Antennas and Propagation*, vol. 50, no. 9, pp. 1315–1316, 2002.
- [9] J. Lee, J. Zhang, and C.-C. Lu, "Incomplete LU preconditioning for large scale dense complex linear systems from electromagnetic wave scattering problems," *Journal of Computational Physics*, vol. 185, no. 1, pp. 158–175, 2003.
- [10] Y. Saad, "ILUT: A dual threshold incomplete LU factorization," *Numerical Linear Algebra with Applications*, vol. 1, no. 4, pp. 387–402, 1994.
- [11] T. Malas and L. Gürel, "Incomplete LU preconditioning with the multilevel fast multipole algorithm for electromagnetic scattering," *SIAM Journal on Scientific Computing*, vol. 29, no. 4, pp. 1476–1494, 2007.
- [12] J. Lee, J. Zhang, and C.-C. Lu, "Sparse inverse preconditioning of multilevel fast multipole algorithm for hybrid integral equations in electromagnetics," *Institute of Electrical and Electronics Engineers. Transactions on Antennas and Propagation*, vol. 52, no. 9, pp. 2277–2287, 2004.
- [13] E. Chow, "A priori sparsity patterns for parallel sparse approximate inverse preconditioners," *SIAM Journal on Scientific Computing*, vol. 21, no. 5, pp. 1804–1822, 2000.
- [14] B. Carpentieri, I. S. Duff, L. Giraud, and G. Sylvand, "Combining fast multipole techniques and an approximate inverse preconditioner for large electromagnetism calculations," *SIAM Journal on Scientific Computing*, vol. 27, no. 3, pp. 774–792, 2005.
- [15] M. Benzi and M. Tuna, "A comparative study of sparse approximate inverse preconditioners," *Applied Numerical Mathematics*, vol. 30, no. 2-3, pp. 305–340, 1999.
- [16] R. E. Bank and C. Wagner, "Multilevel ILU decomposition," *Numerische Mathematik*, vol. 82, no. 4, pp. 543–576, 1999.
- [17] Y. Saad and J. Zhang, "BILUM: Block Versions of Multilevel Elimination and Multilevel ILU Preconditioner for General Sparse Linear Systems," *SIAM Journal on Scientific Computing*, vol. 20, no. 6, pp. 2103–2121, 1999.
- [18] M. Bollhöfer and Y. Saad, "Multilevel preconditioners constructed from inverse-based ILUs," *SIAM Journal on Scientific Computing*, vol. 27, no. 5, pp. 1627–1650, 2006.
- [19] B. Carpentieri and M. Bollhöfer, "Symmetric inverse-based multilevel ilu preconditioning for solving dense complex non-hermitian systems in electromagnetics," *Progress in Electromagnetics Research*, vol. 128, pp. 55–74, 2012.
- [20] R. Chandra, R. Menon, L. Dagum, D. Kohr, D. Maydan, and J. McDonald, *Parallel Programming in OpenMP*, Morgan Kaufmann, 2000.
- [21] Y. Saad and M. H. Schultz, "GMRES: a generalized minimal residual algorithm for solving nonsymmetric linear systems," *SIAM Journal on Scientific and Statistical Computing*, vol. 7, no. 3, pp. 856–869, 1986.
- [22] E. Anderson, Z. Bai, C. Bischof et al., *LAPACK Users Guide*, SIAM, Philadelphia, PA, USA, 1999.
- [23] E. Kemptner and Erich, "Results to test case PLACYL at Workshop EM JINA," in *Proceedings of the Workshop Journées Internationales de Nice sur les Antennes (EM JINA)*, Nice, France, 2006.
- [24] M. D. Brzeska, *RF Modelling and Characterization of Tyre Pressure Sensors and Vehicle Access Systems*, KIT Scientific Publishing, 2015.

Research Article

Electromagnetic Scattering of Electrically Large Ship above Sea Surface with SBR-SDFM Method

Lixin Guo and Tiantian Feng

School of Physics and Optoelectronic Engineering, Xidian University, Xi'an 710071, China

Correspondence should be addressed to Tiantian Feng; titife037@163.com

Received 7 July 2017; Accepted 25 September 2017; Published 26 October 2017

Academic Editor: Matteo Pastorino

Copyright © 2017 Lixin Guo and Tiantian Feng. This is an open access article distributed under the Creative Commons Attribution License, which permits unrestricted use, distribution, and reproduction in any medium, provided the original work is properly cited.

Hybrid scheme combining shooting and bouncing ray with semi-deterministic facet model is proposed to analyze composite scattering from ship-ocean scene in this study. This model can deal with complex electromagnetic interaction between ship and sea surface. Thus, scattering properties of composite ship-ocean scenes with influence of various parameters (such as incident angle and wind speed) can be studied and analyzed efficiently. Studying such properties is of significance for target detection and high-resolution radar imaging in sea environments. Accuracy and performance of this method are validated and evaluated by comparing with multilevel fast multipole method of FEKO for electrically small objects. All simulation results indicate that the proposed method is suitable for providing preliminary radar cross section prediction of electrically large composite model.

1. Introduction

Electromagnetic scattering of electrically large targets above rough sea surface is common military scene in target detection and tracking [1–3]. In recent years, extensive endeavors have been devoted to simulation of such complex composite scattering. Method of Moment (MoM) [4] is widely used numerical algorithm, which is adequately developed into fast algorithms, such as Generalized Forward-Backward Method (GFBM) [5, 6] and multilevel fast multipole algorithm (MLFMA) [7, 8]. However, such methods require considerable computational time when dealing with electrically large targets. Asymptotic methods such as Iterative Physical Optics (IPO) which contains a large number of iterations to ensure the accuracy also face poor computing efficiency. Traditional four-path model [9] uses complex reflection coefficient to evaluate coupling interaction of ship-ocean. However, actual sea surface is usually assumed to be two-scale rough surface model [10]: capillary waves modulated by gravity wave in large scale. Thus, scattering field is not only concentrated on specular direction. Besides, four-path model cannot consider mutual shade between ship and ocean. Shooting and Bouncing Ray (SBR) [11, 12] seems more flexible and suitable for such issue. With ray tracing capacity of SBR method, multiple

interactions between ship and ocean can be determined. Nevertheless, SBR method requires more refined meshes involving capillary waves on the sea surface. This requirement enormously increases computing burden. For large-scope sea surfaces, semi-deterministic facet scattering model (SDFM) [13, 14] was developed in relevant publications. In this model, elementary radar echoes from respective facets are computed by a semideterministic scheme considering both specular and diffuse configurations.

This paper aims to establish feasible scheme that conforms to sea surface two-scale model by combining SDFM and SBR method. With SDFM considering Bragg scattering from capillary waves, sea surface can be meshed into larger triangle patches, which adapt well to SBR method for ray tracing between the ship and ocean. Additionally, based on improved backward SBR tracing process and kd-tree acceleration treatment mentioned in [15], computation time rapidly decreases. In the proposed composite scattering model, SBR method is used to calculate scattering from multiple interactions of ship-ocean and scattering from ship, whereas scattering from sea surface is calculated by SDFM. Hybrid SBR-SDFM method should be time-saving and highly efficient to handle radar cross section calculation of electrically large ship-ocean composite model.

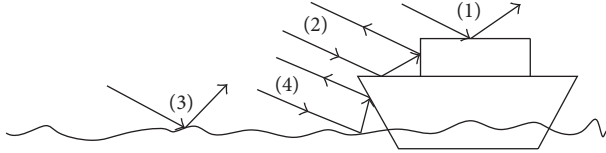


FIGURE 1: Illustration of composite scattering model.

2. SBR-SDFM Method for Composite Scattering

2.1. Composite Scattering Model of Ship-Ocean. Figure 1 shows simplified composite scattering model of ship above rough sea surface. Under framework of the SBR-SDFM method, composite scattering model is divided into four major parts.

(1) *Single Scattering from Ship.* This part is calculated equivalently by physical optics. During the computation, not only self-shade of ship but also shade to ship by sea surface should be taken into consideration. As shown in Figure 1, scattering calculation does not involve part of ship submerged in sea surface.

(2) *Multiple Scattering from Ship.* This part is calculated by SBR. Ship model usually contains numerous dihedral structures; these structures can generate large number of multiple reflections, which develop into major components of backscattered field. Hence, multiple scattering of ship should be considered.

(3) *Single Scattering from Sea Surface.* SDFM method is adopted to calculate scattering contribution of sea surface. In the theory of SDFM, sea wave is envisaged as a superposition of gravity wave configuration approximated by planar facets and capillary wave configuration added on the planar facets at resonant wavenumber. This assumption better conforms to the sea surface two-scale model than PO or SBR. Then, with Bragg scattering from capillary waves being considered separately, sea surface can be meshed into larger triangle patches, which can adapt well to the SBR method for ray tracing between ship and ocean. Thus, computing time is comparatively reduced. Furthermore, visibility of facets on the sea surface should be checked to eliminate shade from ship and other facets on the sea surface.

(4) *Coupling Scattering between Ship and Sea Surface.* This part will be discussed in Section 2.2 in detail.

Then, scattered field of composite model \vec{E}^{total} can be developed by creating superposition of obtained scattered fields:

$$\vec{E}^{\text{total}} = \vec{E}^{\text{ship},1} + \vec{E}^{\text{ship},2,3,\dots} + \vec{E}^{\text{sea},1} + \vec{E}^{\text{sea-ship},1,2,3,4}, \quad (1)$$

where $\vec{E}^{\text{ship},1}$, $\vec{E}^{\text{ship},2,3,\dots}$, $\vec{E}^{\text{sea},1}$, and $\vec{E}^{\text{sea-ship},1,2,3,4}$ are scattering field of four parts mentioned above, respectively.

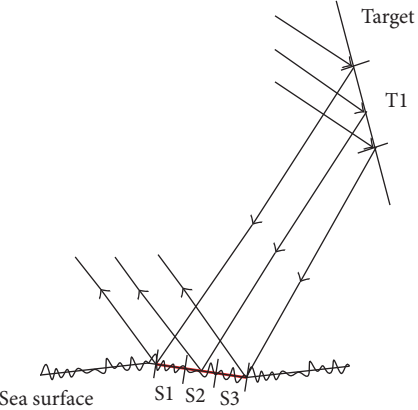


FIGURE 2: Illustration of ray tracing for coupling interaction of ship-ocean.

2.2. Coupling Scattering between Ship and Ocean. SBR method is applied to describe coupling of ship and sea surface (see Figure 2). There are four main ray paths included: ship-sea, sea-ship, ship-sea-ship, and sea-ship-sea. First, the ship and the sea surface are meshed into triangle patches, which are numbered and stored into kd-trees, respectively. Taking ray path ship-sea as an example, given the incident wave direction, patches on the ship model illuminated directly by the incident wave will be identified (i.e., triangle T1) and stored into computer memory as an array. Then the ray starts from illuminated patches on the ship and propagates along the reflected direction, implementing intersection tests with previously built kd-tree of sea surface to determine illuminated patches on the sea surface. Once one patch is found to be illuminated (i.e., triangle S2), backward ray tracing will be performed on its neighbors (i.e., triangles S1 and S3; their IDs are always adjacent to illuminated patches) to check their visibility. Finally, calculation will be performed on far field scattering of all illuminated patches on the sea surface.

In this study, scattering field from sea surface is computed based on SDFM. Bragg scattering field from each facet can be obtained by Fuks' model, with fair approximation that Bragg wave is a single frequency sinusoidal wave to simplify computation, and the polarization factor is modulated by gravity wave. The Bragg scattering field can be expressed as follows:

$$\vec{E}_{pq}^{\text{facet}}(\hat{k}_i, \hat{k}_s) = 2\pi \frac{\exp(ikR)}{iR} S_{pq}(\hat{k}_i, \hat{k}_s), \quad (2)$$

where \hat{k}_i and \hat{k}_s represent the combined vectors of incident and scattered wave number, respectively; R is the distance from the observation to the facet centers; k is the electromagnetic wave number; p and q are the polarization of the incident and scattered wave; S_{pq} denotes the scattering amplitude that can be expressed as

$$S_{pq}(\hat{k}_i, \hat{k}_s) = \frac{k^2(1-\varepsilon)}{8\pi^2} F_{pq} \iint \xi(\vec{r}) \exp(-i\vec{q} \cdot \vec{r}) d\vec{r}, \quad (3)$$

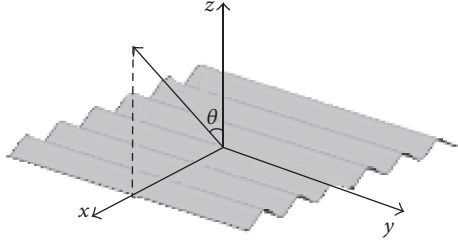


FIGURE 3: Illustration of a single frequency sinusoidal wave model.

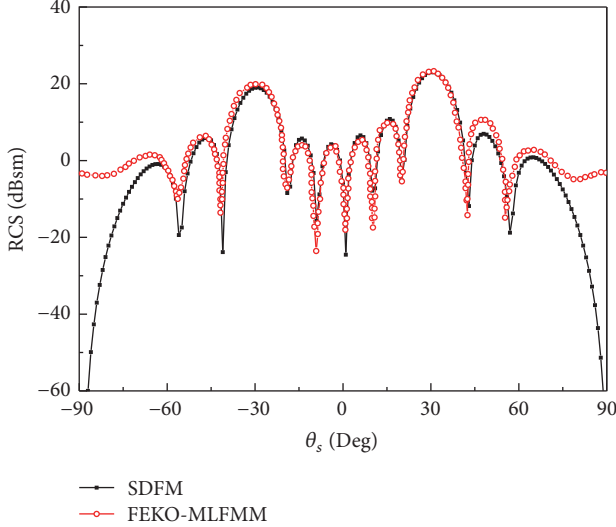


FIGURE 4: Bistatic RCS results for the facet (HH-polarization).

where ϵ is the relative permittivity of the sea water. \vec{q} is defined by $\vec{q} = k(\hat{k}_i - \hat{k}_s)$, and k is the electromagnetic wave number. F_{pq} is the polarization factor.

$\xi(\vec{r})$ in (3) represents the fluctuations of the capillary on the facet, which is envisaged to be a sinusoidal wave that can result in the Bragg resonance and it can be written as

$$\xi(\vec{r}, t) = B(\vec{k}_c) \sin(\vec{k}_c \cdot \vec{\rho}_c - \omega_c t), \quad (4)$$

where \vec{k}_c, ω_c are the wavenumber and circle frequency of the Bragg resonance and $\vec{\rho}_c$ is the coordinate of the respective point on the facet. $B(\vec{k}_c) = 2\pi\sqrt{S_{PM}(\vec{k}_c)/\Delta S}$ is the amplitude of the sinusoidal short wave, $S_{PM}(\vec{k}_c)$ is the sea spectrum, and ΔS is the area of each facet.

We have performed simulation for an individual facet ($6\lambda \times 6\lambda$) on the sea surface (see Figure 3) to verify the correctness of the model. Consider a sinusoidal wave expressed by $\xi = 0.015 \cos(2\pi x_g/\Lambda)$, where x_g is the size of the facet and $\Lambda = \lambda/(2 \sin \theta_i)$ is the spatial wavelength satisfying the Bragg resonance. The dielectric constant of the sea surface is (71.603, 50.657) and the incident wave frequency is set to 2.0 GHz. The incident direction is set by $\theta_i = 30^\circ$, $\varphi_i = 0^\circ$. Figures 4 and 5 show numerical results of SDFM compared with those simulated by MLFMM in commercial software FEKO. Results of SDFM are consistent with those of

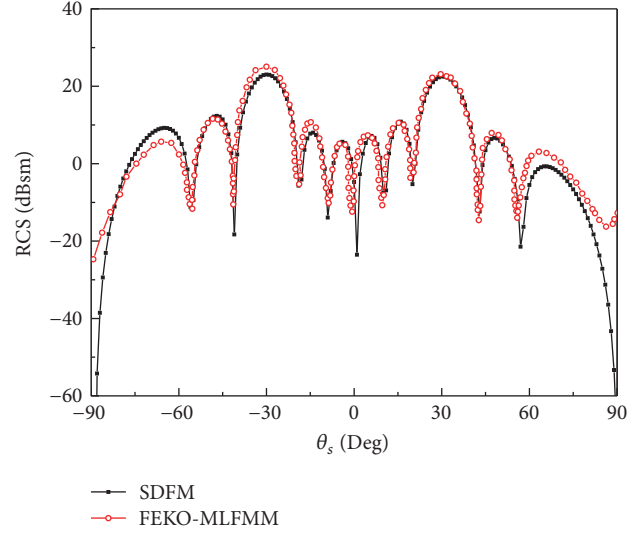


FIGURE 5: Bistatic RCS results for the facet (VV-polarization).

TABLE 1: Runtime performances of different methods.

Method	SDFM	MLFMM (FEKO)
Runtime (s)	49.864	4210.692

MLFMM. Table 1 presents the computational time of results in Figure 4. The computer configuration is Intel(R) Xeon(R) CPU (2.1 GHz, 32.0 GB).

As for the ray path sea-ship, instead of patches on the ship, patches on the sea surface illuminated directly by the incident wave will be determined first, and the ray tracing process will be implemented from sea surface to ship. Finally, scattering field of illuminated patches on the ship will be calculated by PO. Scattering field approximated by PO integral can be written as follows:

$$\begin{aligned} \vec{E}^s &= \frac{jk \exp(-jkR)}{4\pi R} \\ &\cdot \iint \eta \cdot \hat{k}_s \times (\hat{k}_s \times \vec{J}) \exp(jk\hat{k}_s \cdot \vec{r}') ds', \end{aligned} \quad (5)$$

where $\eta = (\epsilon_0/\mu_0)^{1/2}$; \vec{J} is the current density at \vec{r}' on the patch.

The high order coupling interaction of sea-ship-sea or ship-sea-ship is similar to the second-order interaction described above. The difference is that high order coupling interaction requires one more ray tracing process.

2.3. Multiple Scattering of Ship. There are some simulation results to verify the necessity of taking multiple scattering of the ship into account. Figure 6 displays dimensions of the ship. Figure 7 shows monostatic scattering results of the ship; results include both first-order scattering and second-order scattering.

Results present visible difference. When multiple scattering of the ship is considered, the backscattering field will be significantly enhanced.

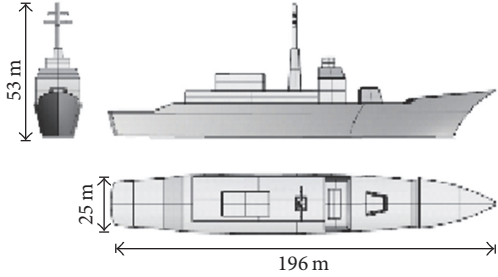


FIGURE 6: Illustration of dimensions of the ship.

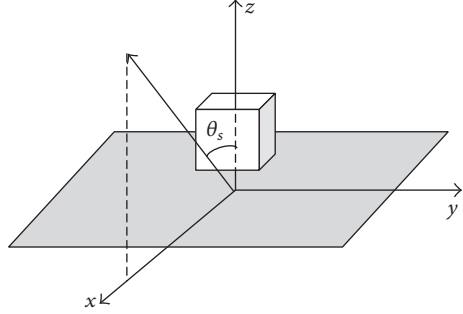


FIGURE 8: Illustration of a cube on flat plate.

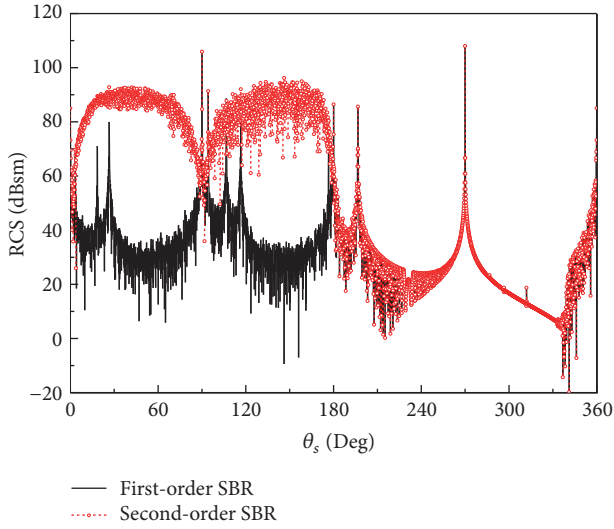


FIGURE 7: Monostatic RCS results for the ship with the incident plane at 10 GHz.

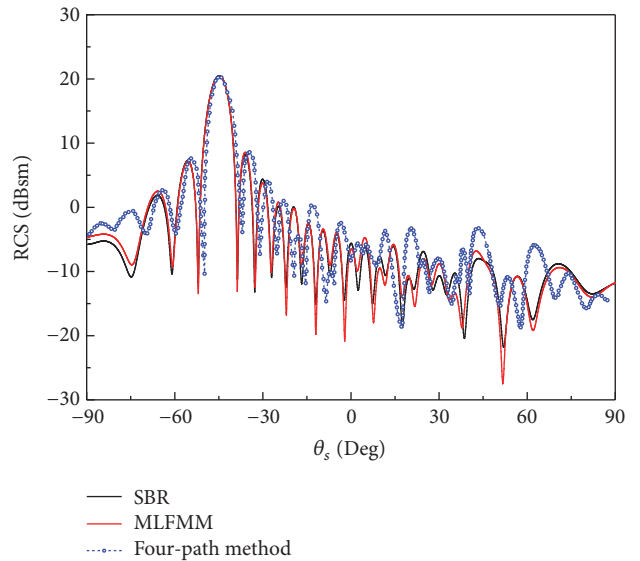


FIGURE 9: Bistatic RCS results for 0.03 m cube on flat plate.

3. Results and Discussion

3.1. Validation for the Composite Scattering Model

3.1.1. Cube on Flat Plate. The composite model of a flat plate ($0.36 \times 0.36 \text{ m}^2$) with a cube located over at height of 0.03 m is simulated at frequency of 10 GHz for HH-polarization (see Figure 8). Figure 9 shows bistatic RCS of the model when side length of the cube is 0.03 m, and the incident angles are set to $\theta_i = 45^\circ$, $\varphi_i = 0^\circ$. The monostatic RCS is shown in Figure 10. The results of SBR method agree well with results based on MLFMM. Furthermore, higher accuracy is obtained compared with the four-path model.

3.1.2. Sphere on Rough Sea Surface. The diameter of the sphere is 0.3 m and the sphere is above the sea surface by 0.15 m (see Figure 11). The sea area is $1.8 \times 1.8 \text{ m}^2$, and the wind speed is $U = 0.5 \text{ m/s}$. The incident angle is $\theta_i = 30^\circ$, whereas the frequency of the incident wave is 4 GHz. Both the sphere and sea surface are assumed to be perfect electronic conductor. Figure 12 shows the bistatic RCS results of the model for HH-polarization. The simulation results calculated by our method are in good agreement with those by FEKO-MLFMM.

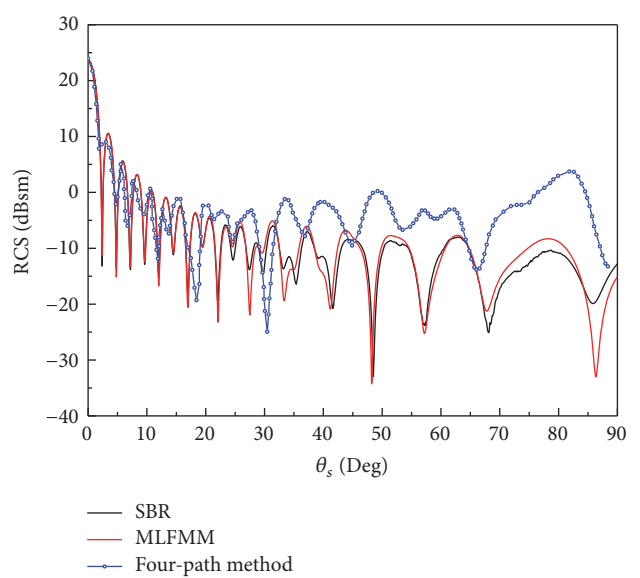


FIGURE 10: Monostatic RCS results for 0.03 m cube on flat plate.

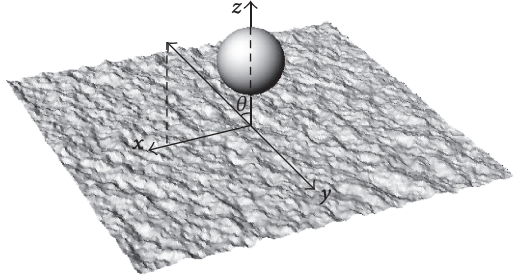


FIGURE 11: Illustration of a sphere on flat plate.

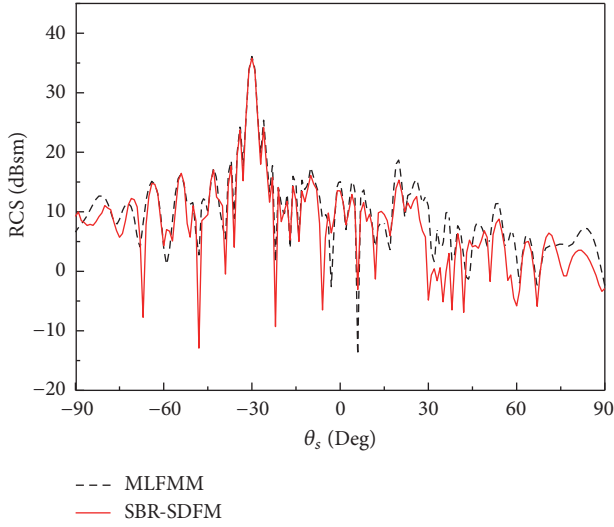


FIGURE 12: Bistatic RCS for a sphere above sea surface.

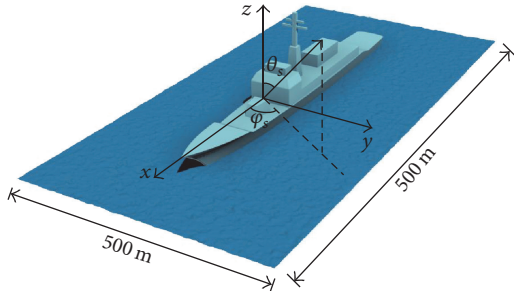


FIGURE 13: Illustration of the composite model of ship-ocean.

3.2. Composite Scattering of the Ship-Ocean. In the following, SBR-SDFM method is applied to the RCS prediction of the battle cruiser above the sea surface. As presented in Figure 13 (dimensions of the ship are the same as those in Figure 6), large size of model causes almost impossible calculation and analysis of scattering problem using numerical algorithm at high frequencies.

In our simulation, the incident wave frequency is fixed at 10 GHz. The permittivity of the sea surface is (65.4219, 34.9864). First, bistatic RCS for HH-polarization is calculated with the incident direction set at $\theta_i = 60^\circ$, $\varphi_i = 90^\circ$, and the scattering direction is $\theta_s = -90^\circ \sim 90^\circ$, $\varphi_s = 90^\circ$. The wind speed is selected by $U = 5 \text{ m/s}$. Figure 14 illustrates

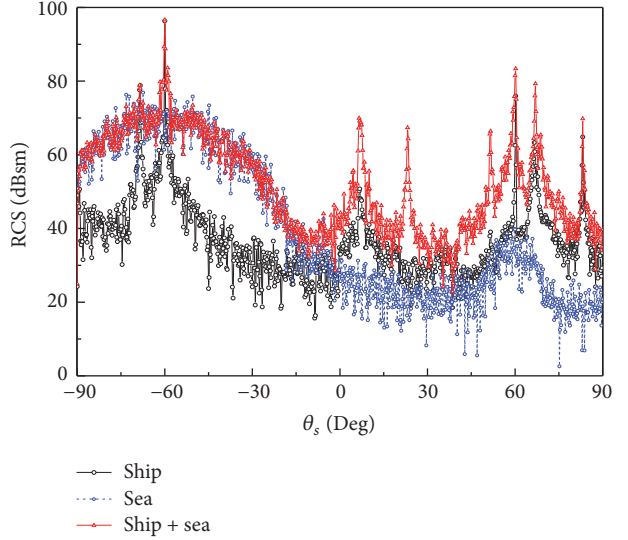


FIGURE 14: Bistatic RCS results of HH-polarization for the ship-ocean model.

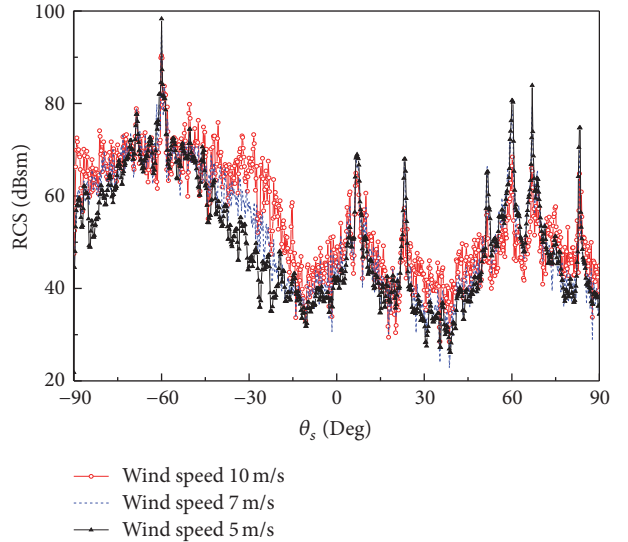


FIGURE 15: Bistatic RCS results for HH-polarization of the ship-ocean model at different wind speed.

bistatic RCS results. For this scenario, flank of the ship and the sea surface form strong coupling, which can significantly increase the backscattered field intensity. It can be seen from the results that when scattering angle varies from $\theta_s = 0^\circ$ to $\theta_s = 90^\circ$, scattering from both ship and coupling interaction preponderate in the total scattered field because of dihedral reflectors on the ship and dihedral reflectors formed by flank of the ship and the sea surface. Nevertheless, in the specular direction, scattering from the sea surface dominates the total scattering field.

As is known, the wind speed is a principal factor that influences the composite scattering field. The simulation results of bistatic RCS for the HH-polarization in different wind speeds 5 m/s, 7 m/s, and 10 m/s are shown in Figure 15. The incident wave slants at $\theta_i = 60^\circ$, $\varphi_i = 90^\circ$, and the

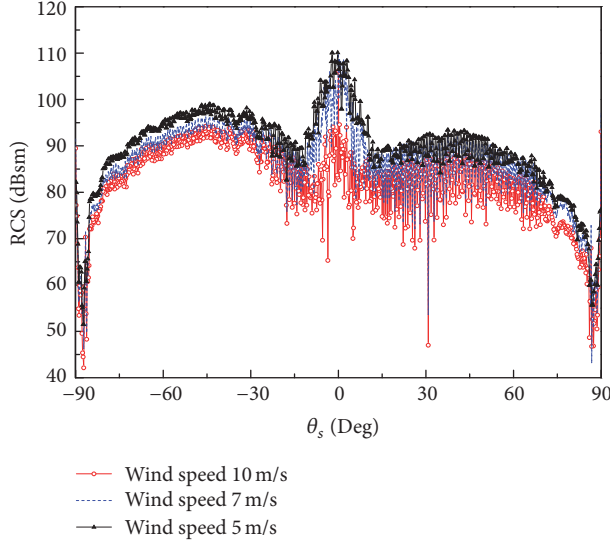


FIGURE 16: Monostatic RCS results for HH-polarization of the ship-ocean model at different wind speed.

scattering direction is $\theta_s = -90^\circ \sim 90^\circ$, $\varphi_s = 90^\circ$. As the wind speed increases, the fluctuation of sea surface becomes stronger, which can attenuate the scattering intensity in specular direction but enhance that in diffuse direction. From the comparison results in Figure 15, one can see that scattering field intensity in most diffuse directions increases and the scattering field intensity in specular direction decreases, as the wind speed increases.

Figure 16 indicates the monostatic RCS results of the ship-ocean model at different wind speed. The incident and scattering angles are set by $\theta_s = \theta_i$, $\varphi_s = \varphi_i = 90^\circ$. As the wind speed decreases, specular scattering from sea surface is enhanced. This phenomenon consequently amplifies the coupling interaction between ship and ocean, further increasing the composite scattering.

4. Conclusion

This paper proposes suitable and efficient hybrid SBR-SDFM method for calculation of composite scattering of electrically large ship above sea surface. SBR and SDFM are, respectively, applied to the ship and sea surface. For the key problem coupling interaction between the ship and the sea surface, SBR is used to provide accurate simulation. Results for the validation of the method indicate good agreement with exact numerical method of FEKO.

Conflicts of Interest

The authors declare that they have no conflicts of interest.

Acknowledgments

This work was supported in part by the National Science Foundation for Distinguished Young Scholars of China (Grant no. 61225002), the Foundation for Innovative Research Groups of the National Natural Science Foundation

of China (Grant no. 61621005), the National Natural Science Foundation of China (Grant no. 61431010), and the National Science Foundation of China (Grant no. 61501361).

References

- [1] V. Fabbro, P. F. Combes, and N. Guillet, "Apparent radar cross section of a large target illuminated by a surface wave above the sea," *Progress in Electromagnetics Research*, vol. 50, pp. 41–60, 2005.
- [2] W.-J. Ji and C.-M. Tong, "Bistatic scattering from two-dimensional dielectric ocean rough surface with a pec object partially embedded by using the G-SMC method," *Progress in Electromagnetics Research*, vol. 105, pp. 119–139, 2010.
- [3] A. Baussard, M. Rochdi, and A. Khenchaf, "PO/MEC-based scattering model for complex objects on a sea surface," *Progress in Electromagnetics Research*, vol. 111, pp. 229–251, 2011.
- [4] S. M. Rao, D. R. Wilton, and A. W. Glisson, "electromagnetic scattering by surfaces of arbitrary shape," *IEEE Transactions on Antennas and Propagation*, vol. 30, no. 3, pp. 409–412, 1982.
- [5] M. Pino, L. Landesa, J. L. Rodriguez, F. Obelleiro, and R. J. Burkholder, "The generalized forward-backward metod for analyzing the scattering from targets on ocean-like rough surfaces," *IEEE Transactions on Antennas and Propagation*, vol. 47, no. 6, pp. 961–969, 1999.
- [6] Y. Jin and Z. Li, "Numerical simulation of radar surveillance for the ship target and oceanic clutters in two-dimensional model," *Radio Science*, vol. 38, no. 3, pp. 1045–1050, 2003.
- [7] W. Yang, Z. Q. Zhao, C. H. Qi, W. Liu, and Z. P. Nie, "Iterative hybrid method for electromagnetic scattering from a 3-d object above a 2-d random dielectric rough surface," *Progress in Electromagnetics Research*, vol. 117, pp. 435–448, 2011.
- [8] O. Ergul, "Parallel implementation of mlfma for homogeneous objects with various material properties," *Progress in Electromagnetics Research*, vol. 121, pp. 505–520, 2011.
- [9] J. T. Johnson, "A study of the four-path model for scattering from an object above a half space," *Microwave and Optical Technology Letters*, vol. 30, no. 2, pp. 130–134, 2001.
- [10] F. G. Bass and I. M. Fuks, *Wave Scattering from Statistically Rough Surfaces*, Pergamon Press, 1979.
- [11] H. Ling, "Shooting and Bouncing Rays: Calculating the RCS of an Arbitrarily Shaped Cavity," *IEEE Transactions on Antennas and Propagation*, vol. 37, no. 2, pp. 194–205, 1989.
- [12] L.-X. Guo and T.-Q. Fan, "Octree based backward SBR-PO method for electromagnetic scattering of electrically large target," in *Proceedings of the 2015 1st IEEE International Conference on Computational Electromagnetics, ICCEM 2015*, pp. 300–305, hkg, February 2015.
- [13] Y. Wei, L. Guo, and J. Li, "Numerical simulation and analysis of the spiky sea clutter from the sea surface with breaking waves," *Institute of Electrical and Electronics Engineers. Transactions on Antennas and Propagation*, vol. 63, no. 11, pp. 4983–4994, 2015.
- [14] F. G. Bass, I. M. Fuks, A. I. Kalmykov, I. E. Ostrovsky, and A. D. Rosenberg, "Very high frequency radiowave scattering by a disturbed sea surface part i: scattering from a slightly disturbed boundary," *IEEE Transactions on Antennas and Propagation*, vol. AP-16, no. 5, pp. 554–559, 1968.
- [15] T.-Q. Fan, L.-X. Guo, B. Lv, and W. Liu, "An improved backward SBR-PO/PTD hybrid method for the backward scattering prediction of an electrically large target," *IEEE Antennas and Wireless Propagation Letters*, vol. 15, pp. 512–515, 2016.

Research Article

Research on Spatial Channel Model for Vehicle-to-Vehicle Communication Channel in Roadside Scattering Environment

Xin Chen,¹ Yong Fang,¹ Weidong Xiang,² and Liang Zhou³

¹Key Laboratory of Specialty Fiber Optics and Optical Access Networks, Shanghai University, Shanghai 200444, China

²Department of Electrical and Computer Engineering, University of Michigan-Dearborn, Dearborn, MI 48128, USA

³School of Communication and Information Engineering, University of Electronic Science and Technology of China, Chengdu 611731, China

Correspondence should be addressed to Yong Fang; yfang@staff.shu.edu.cn

Received 9 June 2017; Revised 2 September 2017; Accepted 19 September 2017; Published 22 October 2017

Academic Editor: Matteo Pastorino

Copyright © 2017 Xin Chen et al. This is an open access article distributed under the Creative Commons Attribution License, which permits unrestricted use, distribution, and reproduction in any medium, provided the original work is properly cited.

In this paper, an extension of spatial channel model (SCM) for vehicle-to-vehicle (V2V) communication channel in roadside scattering environment is investigated for the first time theoretically and by simulations. Subsequently, to efficiently describe the roadside scattering environment and reflect the nonstationary properties of V2V channels, the proposed SCM V2V model divides the scattering objects into three categories of clusters according to the location of effective scatterers by introducing critical distance. We derive general expressions for the most important statistical properties of V2V channels, such as channel impulse response, power spectral density, angular power density, autocorrelation function, and Doppler spread of the proposed model. The impact of vehicle speed, traffic density, and angle of departure, angle of arrival, and other statistical performances on the V2V channel model is thoroughly discussed. Numerical simulation results are presented to validate the accuracy and effectiveness of the proposed model.

1. Introduction

Vehicle-to-vehicle (V2V) communication has recently received phenomenal attention over the past few years in both automakers and academia domains as it plays a vital role in intelligent highways, collision avoidance, vehicles safety, and better traffic efficiency [1, 2]. As a new emerging communication system, V2V communication is regarded as one basic type of communications in vehicular ad hoc networks (VANET), also particularly useful in autonomous driving system. More importantly, VANET can accurately be represented by different forms of topologies: V2V and vehicle-to-roadside (V2R) [3]. VANET technology has also been hailed as a full wireless communication solution in advancing driving comfort and increasing traffic safety and ecological efficiency.

The design and deployment of the IEEE 802.11p standard, as well as alternative V2V wireless communication systems, require a deep understanding of the underlying

V2V radio propagation channel behavior to facilitate the information delivery in VANET. Due to the mobility of both transmitter (Tx) and receiver (Rx), a big challenge in V2V communications is that it is difficult for the wireless channel between vehicles to achieve accurate and effective modeling of the V2V communication channel. It is well known that the mathematical channel characteristics can provide fundamental knowledge for all communication system physical layer waveform design and analysis [4]. Reliable knowledge of the propagation channel and a corresponding realistic channel model serve as the enabling foundation for flexible and practical design and testing of V2V systems. It is worth pointing out that channel modeling is usually faced with the dilemma of capturing the maximum of true V2V dynamic processes while limiting the number of input parameters and computational cost. This underlines the importance of developing physically meaningful yet easy-to-use methods to mimic V2V channels.

It is natural to ponder the possibility that measurement campaigns at different sites representing the crossing, suburban, highway, and rural environments are the most direct strategy [5]. However, VANET research relies heavily on simulations, due to the prohibitive costs of deploying real-world testbeds. There is therefore actual motivation and interest to investigate the fact that mathematical channel characterization results provide fundamental knowledge for V2V channels. Many investigations focus on geometry-based stochastic channel model (GSCM) for its well suiting for nonstationary environments. In particular, regular shape geometry-based stochastic models (RS-GBSM) can be found in [6] (e.g., circular scattering model [7], elliptical scattering model [8], and ring model [9]). To preserve the mathematical tractability, RS-GBSMs assume that all the effective scatterers are located on a regular shape, which may not represent the practical V2V scattering environments due to the randomly distributed scatterers. In order to assess the performance of real-world V2V communication systems, it is imperative to develop a physical understanding of the V2V propagation environment in terms of the angle of departure (AoD), angle of arrival (AoA), and time of arrival (ToA) information of multipath components of the wireless propagation channel.

Due to the obvious advantages such as directly modeling the statistical characteristics of MIMO channel in the time, space, and frequency domains and being flexible in changing the various environments and simple to implement, the feasibility study of using MIMO technology and a modified spatial channel model (SCM) in V2V communication is also discussed [3]. Taking advantage of the ray tracing, SCM models the scattering environment based on the stochastic channel models, which can specify the parameters for SCM and develop a procedure for channel modeling [10, 11]. In the context of roadside scattering, SCM modeling offers a good compromise since it allows adapting location-specific and reducing computationally expensive models compared with general statistical models [4]. Motivated by these facts, this paper investigates the theoretical characteristics of SCM V2V channel model with roadside scattering scenarios to gain a better understanding of the V2V wireless channel.

Proposed Approach. SCM is a wireless propagation channel based on stochastic modeling, especially for outdoor antennas in moving conditions. In contrast to previous V2V modeling works, we recently proposed a simple geometrical SCM V2V model to encapsulate the effect of activity of clusters by introducing relatively different locations and critical distance of scatterers. In this work, we describe the SCM V2V model in detail and discuss its channel impulse response (CIR), power spectral density (PSD), angular power density, autocorrelation function (ACF), and Doppler spread.

The contributions and novelties of this paper are summarized as follows:

- (i) The SCM V2V channel model is first proposed. All scatterers are distributed along the roadside, which is a better description of the assumption that scatterers uniformly distributed around the vehicles in other geometrical models.

- (ii) Considering the relative position between scatterers and vehicles and the similarities of scatterers in a cluster, we divide the scattering objects along the roadside into three categories: "Ahead," "Between," and "Behind," which takes the advantages of GSCMs and cluster-based models.
- (iii) The CIR, PSD, angular power density, ACF, and Doppler spread are derived from the proposed new model.
- (iv) The accuracy and effectiveness of the proposed SCM V2V channel model are validated by extensive simulations.

The rest of this paper is organized as follows. After a review of prior work (Section 2), we propose the cluster-based SCM V2V channel model and derive the expression of CIR, PSD, and angular power density in Section 3. Section 4 analyzes the channel characterization of the proposed channel model. Numerical analysis and simulations are presented in Section 5, followed by the summary and concluding remarks in Section 6.

2. Related Work

In recent years, research into V2V communications has recently gained strong momentum. In particular, with the advent of VANET, efficient and accurate channel modeling is essential to evaluate and validate networking protocols under realistic propagation conditions. We briefly review related works which are closely relevant to our study.

Dedicated short range communication (DSRC) is the wireless communication protocol for the VANET, and 75 MHz of spectrum in 5.85–5.925 GHz band to be allocated for DSRC intended to provide V2V communication coverage within 300 m range has been mandated by the Federal Communications Commission (FCC) [12]. In general, there are three fundamental approaches to channel modeling: deterministic, geometry-based stochastic, and the tapped delay line (TDL) based stochastic models [8]. The author in [13] used ray-tracing software to model the deterministic environment, but its computational cost is exponentially increased with accuracy requirement. The existing GBSM can be easily adapted to diverse scenarios by predefining stochastic distribution of scatterers but yields results that are in very good agreement with the real V2V channels due to not representing the non-wide sense stationary uncorrelated scattering (non-WSSUS) properties conveniently [14]. The TDL models based measurement data may be used widely by their low complexity and extensibility [15], but time-varying tap locations and statistics need to be provided and modified to represent the non-WSSUS properties. Each of the channel modeling methods mentioned above has specific advantages and drawbacks.

In a real-world scenario, vehicle speed has a strong negative correlation with traffic density when the density exceeds a critical value, while traffic density could also be an indication of the multipath effect from signal reflection and scattering. With low elevations for both Rx and Tx antennas,

obstruction of line-of-sight (LOS) paths will be more frequent. The higher the traffic density, the more likely that the case would be non-line-of-sight (NLOS) [16]. Apart from RS-GBSMs, MIMO V2V geometry-based street channel model [17], T-junction models [18], and merging lanes on highway model [19] are proposed to study V2V communications. All the aforementioned V2V models just consider the static scatterers on both roadsides, and there are still pressing needs to model the V2V channels considering both the effect of randomly distributed scatterers and non-WSSUS property. Due to a dynamic change of speed and angle of motion for vehicles and moving scatterers the radio propagation conditions change rapidly, leading to nonstationary channel properties. For an accurate description of V2V elevation plane, 3D channel models have been proposed in [6, 8, 20, 21], for a more precise spatial and temporal description of the V2V communication links relative to that provided by 2D channel models.

The focus of our work is to model the spatiotemporal propagation characteristics of information under V2V communications. To the best of our knowledge, SCM V2V channel is not well surveyed in existing work. We will therefore give more attention to the statistical characteristics of SCM scattering channel model under the scenarios of V2V communications. The multipath components usually distribute in terms of clusters because of similar latency, AoD, AoA, and ToA, which is more close to practical V2V propagation environments [21]. Also, the cluster model is more flexible. With proper parameters setting, the cluster model can be regarded as regular-shaped models. In contrast to previous V2V models that assume that scatterers are uniformly located on either a ring or the first ellipse surrounding the vehicles, we propose a new SCM V2V model based on clusters that all the scattering objects are distributed along the roadside, which is more close to practical V2V environment. Compared with previous V2V models, the proposed SCM V2V model can offer a better tradeoff between tracking accuracy and model complexity. Even though the proposed V2V channel model is yet to be validated empirically, it gives theoretical insights into some statistical characteristics of nonstationary V2V channels.

3. SCM Model for V2V Channels

3.1. A Short Introduction to the SCM. The SCM [22, 23] can be considered as a “statistical ray-tracing method,” which is close to practical V2V environment because both of the near and far scatterers such as buildings and trees are distributed at the roadside randomly.

A simplified overview of SCM V2V scattering channel model is depicted in Figure 1. For the sake of simplicity, only two paths (LOS and NLOS) are shown in the figure. For NLOS path, the model derives the θ_t (AoD, the angle between Tx and scatterers) and the θ_r (AoA, the angle between scatterers and Rx), and, for LOS path, the ϕ_t and ϕ_r are the AoD and AoA without any obstruction between Tx and Rx, respectively.

3.2. The Proposed SCM V2V Channel Model. The main objective of this section is to model the novel V2V channel model using the SCM model. Roadside buildings and on-road obstacles create a lot of reflection making this propagation model not suitable for Rayleigh/AWNG channel model [3]. The proposed V2V channel model is an extension of SCM in roadside scattering environment. Our approach is described as follows. We first consider scatterers distributed along the roadside at different distances, and the geometrical roadside scattering V2V model encompassing fixed and moving scatterers is illustrated in Figure 2. All scatterers belonging to a given cluster have similar AoD and AoA. For one cluster, all the effective scatterers are located on regular geometric region D_c , and the dimension of D_c is far less than the distance between Tx and Rx. The AoA and the AoD are closely related due to the fact that the single-bounced scattering is assumed.

The V2V channel will be short range (1km coverage distance), employing similar low-height antennas and road units and high mobility of user terminals [24]. In agreement with the typical V2V environment in Figure 2, we divide the impulse response into two parts: LOS component and NLOS cluster (including at least two subpaths per cluster) produced from effective scatterers along the roadside. For a cluster, the AoD is referred to as θ_t , whereas the AoA is denoted by θ_r . The symbols $d_{t,i}$ and $d_{r,i}$ stand for the i th subpath from Tx to scatterers before impinging on the Rx. The transmitter and receiver are moving with the velocities v_t and v_r , equipped with N_T and N_R antenna elements. The antenna element spacing at Tx and Rx is denoted by δ_t and δ_r , respectively. The traffic density of a given cluster is referred to as ρ in meters. The distance between Tx and Rx is denoted by L (LOS).

3.3. Channel Impulse Response of SCM V2V Channel Model. In practical propagation environments, scatterers are intensively distributed in terms of clusters along the roadside, and subpaths have similar AoD, AoA, and latency in a cluster. In order to assess the performance of real-world V2V channels, we define three categories of clusters according to the specific location of clusters with respect to vehicles. The SCM V2V channel can be described by the superposition of the sum of scattered components $h_a(t)$, $h_b(t)$, and $h_c(t)$, which represent the CIR of V2V channels caused by different clusters in “Ahead,” “Between,” and “Behind” position as depicted in Figures 3(a), 3(b), and 3(c), respectively.

In this case, the mathematical CIR $h(t)$ can be expressed by the following:

$$\begin{aligned} h(t) &= h_a(t) + h_b(t) + h_c(t) \\ &= \sqrt{\frac{P_n}{M}} \sum_{m=1}^M \left\{ \left[\sqrt{A_t(\theta_{m,n,t})} \right. \right. \\ &\quad \cdot \exp(j(kd_t \sin \theta_{m,n,t} + \phi_{n,m})) \left. \right] \times \left[\sqrt{A_r(\theta_{m,n,r})} \right. \\ &\quad \cdot \exp(j(kd_r \sin \theta_{m,n,r})) \left. \right] \\ &\quad \times \exp(jk \|v\| \cos(\theta_{m,n,r} - \theta_v) t) \left. \right\}. \end{aligned} \quad (1)$$

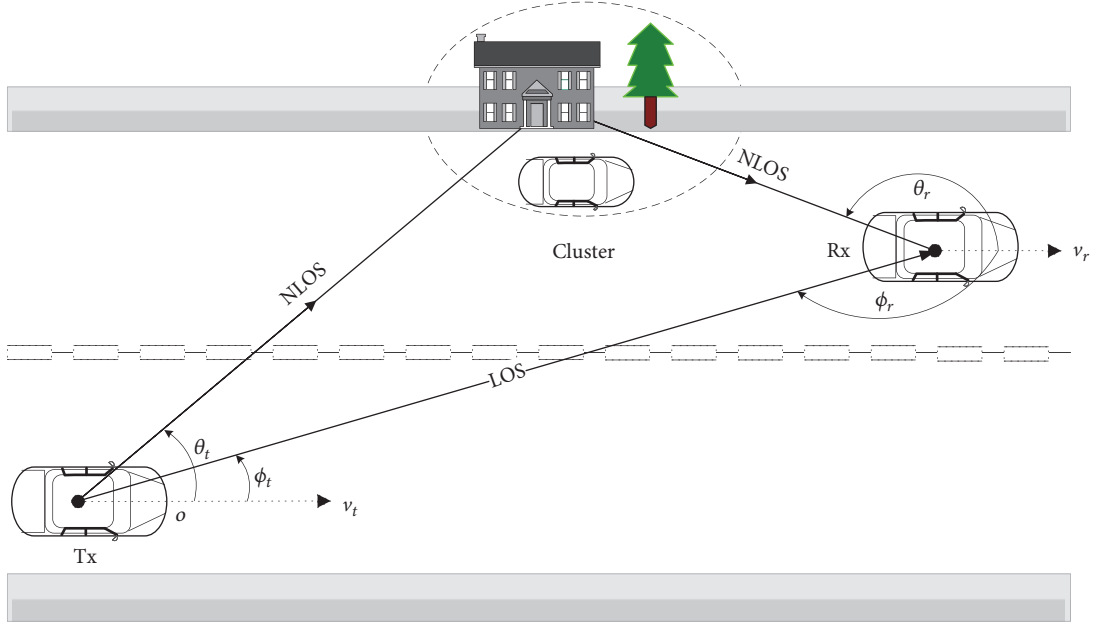


FIGURE 1: Simplified overview of SCM V2V scattering channel model.

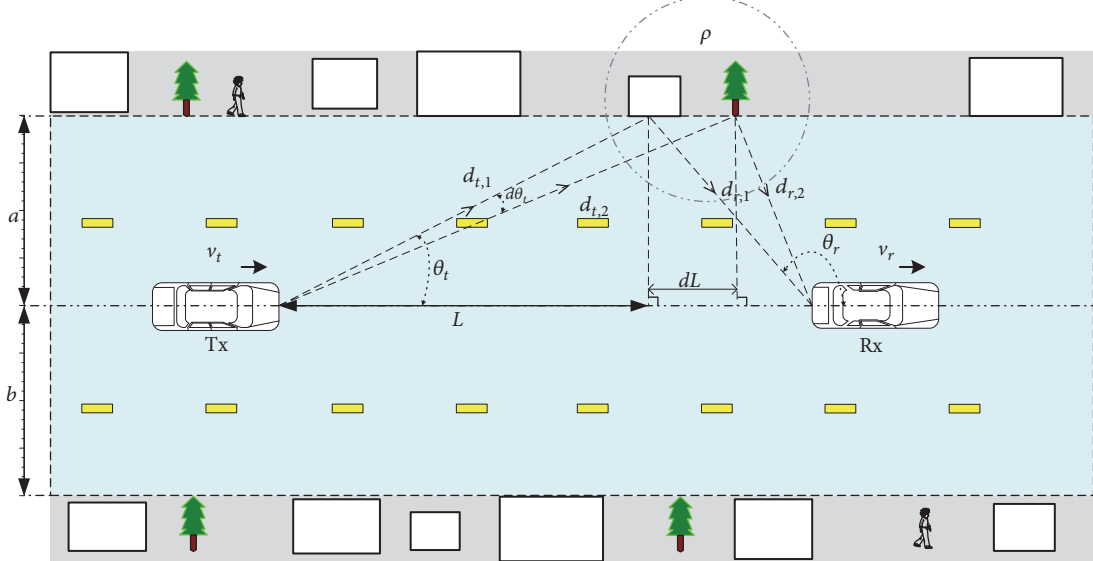


FIGURE 2: Geometrical model for V2V channel in roadside scattering environment.

The key parameters of (1) are summarized in list of model parameters in SCM-V2V model. Figure 4 shows the CIR performance of the proposed model for various transmitter speeds with respect to the receiver. Here, we assume that two vehicles are on a collision course, which are in the absence of LOS component owing to roadside infrastructures, buildings, and foliage. The phase $\phi_{n,m}$ is assumed to be an independent random variable which is uniformly distributed between 0 and 2π . Parameter values used in the calculation are as follows: $M = 20$, $d_t = 20$ m, $d_r = 30$ m, $\theta_{m,n,t} = \pi/3$, $\theta_{m,n,r} = \pi/4$, $\theta_v = \pi/6$, and $A_r = A_t = 1$. All subpaths P_n in a cluster follow a Poisson distribution. It is interesting

to note that the velocity of cluster has a significant effect on the CIR of SCM V2V channel model, and angles and phase changes in (1) have no apparent peak in the calculation of CIR.

3.4. Power Spectral Density. To practically analyze the V2V channel model, it is necessary to derive the accurate expression of PSD from ray-based models and the predefined stochastic distributions of effective scatterers by applying the fundamental laws of wave propagation. The phase offset of subpaths per cluster is omitted here owing to the similar distance of multipath components of V2V propagation channel.

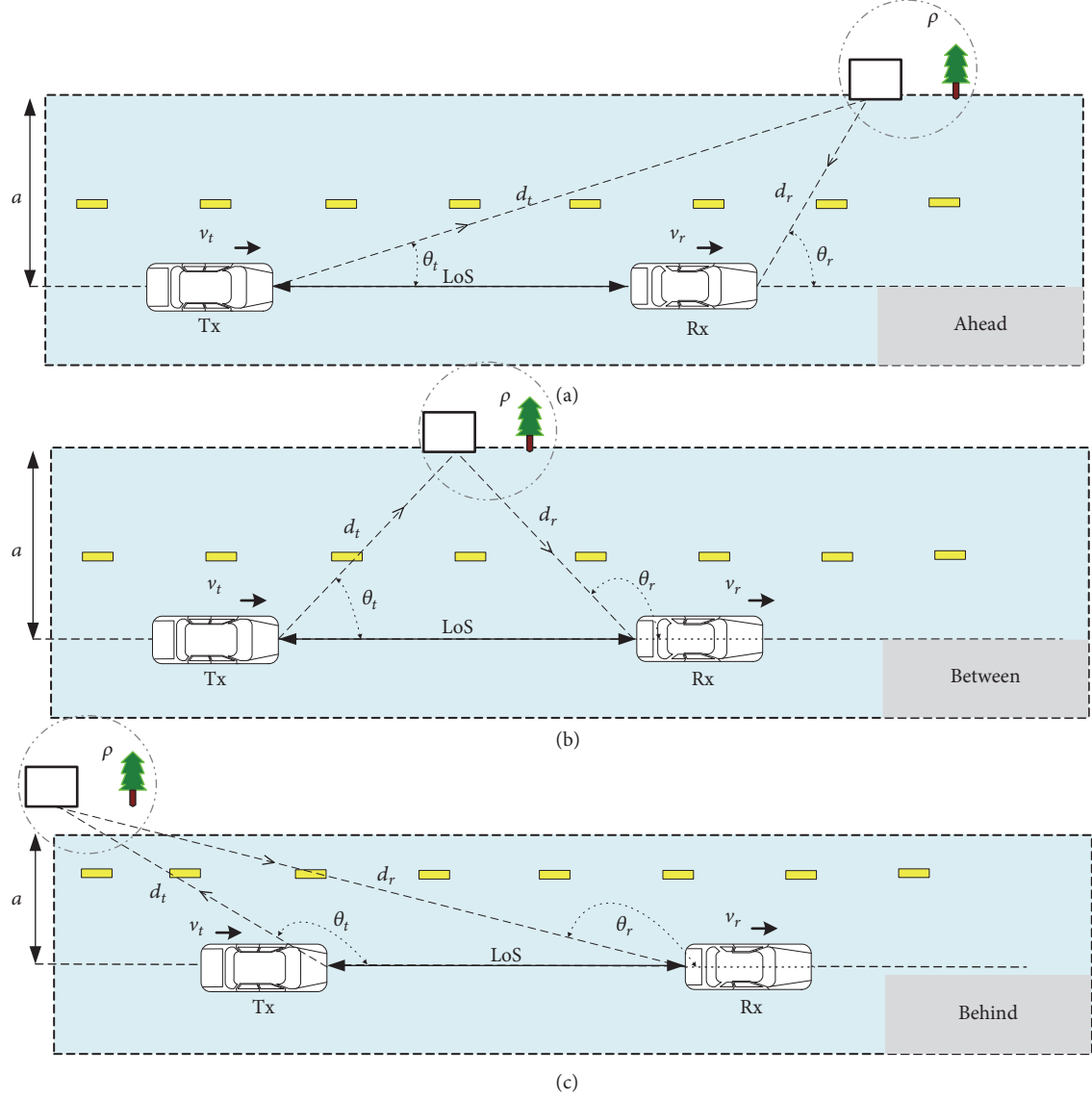


FIGURE 3: Different locations of a cluster along the roadside relative to Tx and Rx.

In agreement with the typical V2V environment in Figure 2, we assume that the amount of power P_r returning to the Rx antenna from a cluster can be described by the following radar equation:

$$P_r = \sum_{i=1}^n \frac{P_t G_t G_r \lambda^2 \sigma}{(4\pi)^3} \left(\frac{1}{d_{t,i}^2} \exp(j(kd_{t,i} \sin \theta_{t,i} + \phi_i)) \right) \cdot \left(\frac{1}{d_{r,i}^2} \exp(j(kd_{r,i} \sin \theta_{r,i})) \right), \quad (2)$$

where P_t and P_r are the transmitted and received power, respectively. G_t and G_r are the Tx and Rx antenna gain, respectively. σ is the radar cross section of the object in square meters (assumed to be isotropic). n is the number of subpaths per path (cluster). λ is the wavelength of the electromagnetic wave at 5.9 GHz. d_t and d_r are the distance from scatterers

to Tx and Rx, respectively. $\theta_{t,i}$ and $\theta_{r,i}$ are the AoD and AoA of the i th subpath, respectively. ϕ_i is the initial phase of i th subpath.

Consider scatterers within the different θ_t and θ_r with respect to the Tx-Rx route (Figure 2). For the sake of simplicity, the number of subpaths is two ($d_{t,1} \rightarrow d_{r,1}$, $d_{t,2} \rightarrow d_{r,2}$), ρ is the density of scatterers in a cluster along the roadside, and a and b are the average distance from Tx-Rx route to the left and right roadside, respectively. We denote L to be the projected distance along the road from angle θ_t , and dL is the projected subpath length change along the road from angle $d\theta_t$.

From the geometry in Figure 2 we have

$$L = \frac{a}{\tan \theta_t}. \quad (3)$$

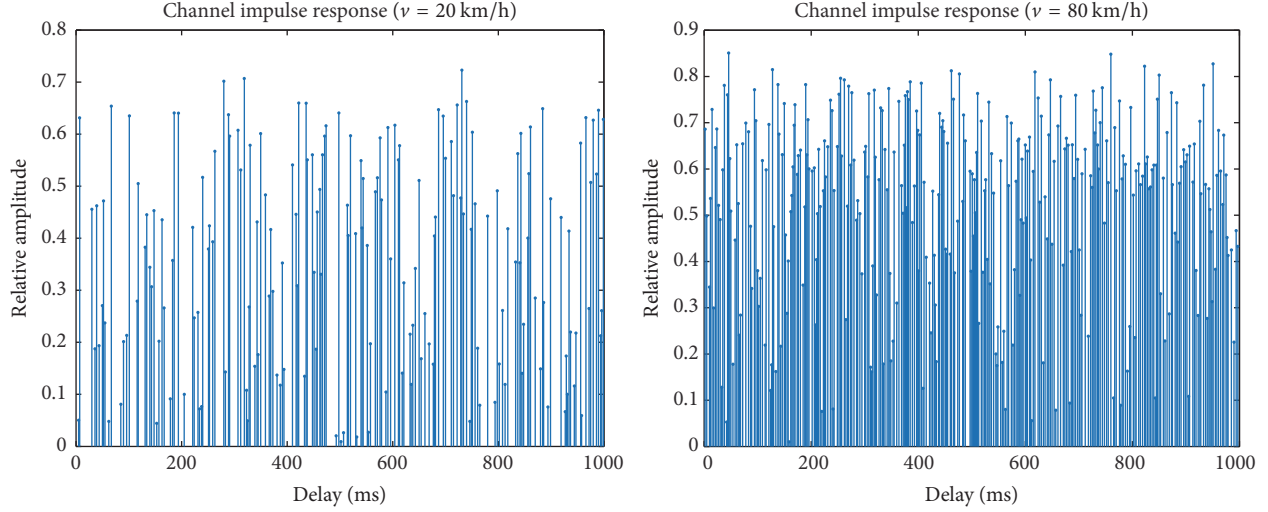


FIGURE 4: Comparison of CIR performance of different vehicle speeds for the SCM V2V channel model (CIR for vehicles speed from 20 km/h to 80 km/h, omnidirectional transmitting antenna).

Taking the derivative on (3) we have

$$dL = -a \csc^2 \theta_t d\theta_t. \quad (4)$$

For a cluster with the angular range $d\theta_t$, the number of scatterers can therefore be given by

$$\rho dL = -\rho a \csc^2 \theta_t d\theta_t. \quad (5)$$

The total power arriving within the range of angles $d\theta_t$ is given by the power from one cluster (see (2)) multiplied by the number of subpaths in the length $-dL$ from (5). Then we can get the following expressions:

$$\begin{aligned} P &= |P_r| \\ &= \sum_{i=1}^n \frac{P_t G_t G_r \lambda^2 \sigma}{(4\pi)^3} \left(\frac{1}{d_{t,i}^2} |\exp(j(kd_{t,i} \sin \theta_{t,i} + \phi_i))| \right) \\ &\quad \cdot \left(\frac{1}{d_{r,i}^2} |\exp(j(kd_{r,i} \sin \theta_{r,i}))| \right) \\ &= \sum_{i=1}^n \frac{P_t G_t G_r \lambda^2 \sigma}{(4\pi)^3} \frac{1}{d_{t,i}^2} \frac{1}{d_{r,i}^2}, \\ dP &= \sum_{i=1}^n \frac{P_t G_t G_r \lambda^2 \sigma}{(4\pi)^3} \left(\frac{1}{d_{t,i}^2} \right) \left(\frac{1}{d_{r,i}^2} \right) \rho a \csc^2 \theta_t d\theta_t. \end{aligned} \quad (6)$$

Thus, the PSD can be expressed as

$$S(f) = \frac{dP}{d\theta_t} \frac{d\theta_t}{df}. \quad (7)$$

The wave is then bounced to Tx. from the view of the scattering object, the relative speed of Tx and Rx is $v_t \cos \theta_t$ and $v_r \cos \theta_r$, respectively. The total Doppler shift is therefore

$$f = \frac{(v_t \cos \theta_t + v_r \cos \theta_r)}{\lambda}. \quad (8)$$

From (8), we obtain

$$\frac{df}{d\theta_t} = -\frac{(v_t \sin \theta_t + v_r \sin \theta_r (d\theta_r/d\theta_t))}{\lambda}. \quad (9)$$

The magnitude of the PSD can be expressed as

$$\begin{aligned} |S(f)| &= \sum_{i=1}^n \frac{P_t G_t G_r \lambda^2 \sigma}{(4\pi)^3} \left(\frac{1}{d_{t,i}^2} \right) \left(\frac{1}{d_{r,i}^2} \right) \frac{\rho a \csc^2 \theta_t}{|df/d\theta_t|} \\ &= \sum_{i=1}^n \frac{P_t G_t G_r \lambda^3 \sigma}{(4\pi)^3} \left(\frac{1}{d_{t,i}^2 d_{r,i}^2} \right) \\ &\quad \cdot \frac{\rho a \csc^2 \theta_t}{(v_t \sin \theta_t + v_r \sin \theta_r d\theta_r/d\theta_t)}. \end{aligned} \quad (10)$$

However, in practice, the dual slope model is a finer granularity fading vehicular channel, which can accurately represent the measurements of V2V modeling [25]. Within a critical distance d_c , the power is an inversely proportional function of distance d squared. Beyond this critical distance, the signal strength varies with inverse fourth power of distance for large d . To intelligently cater for the quantitative relationship, a dimensionless distance function $D(\hat{d}, \hat{d}_c)$ can be given by

$$D(\hat{d}, \hat{d}_c) = \begin{cases} \frac{1}{\hat{d}^2} & \text{if } \hat{d} \leq \hat{d}_c \\ \frac{1}{\hat{d}_c^2} \left(\frac{\hat{d}_c}{\hat{d}} \right)^4 & \text{if } \hat{d} > \hat{d}_c, \end{cases} \quad (11)$$

where $\hat{d}_c \equiv d_c/d_{tr}$ and $\hat{d} \equiv d/d_{tr}$ are normalized distances to the separation distance between Tx and Rx in a single cluster ($d_{tr} = d_{t,i} + d_{r,i}$). Here, d_c can be calculated as the first Fresnel distance $d_c = 4h_t h_r / \lambda$, where h_t and h_r are antenna heights of Tx and Rx, respectively [5, 25]. For simplicity, we assume that

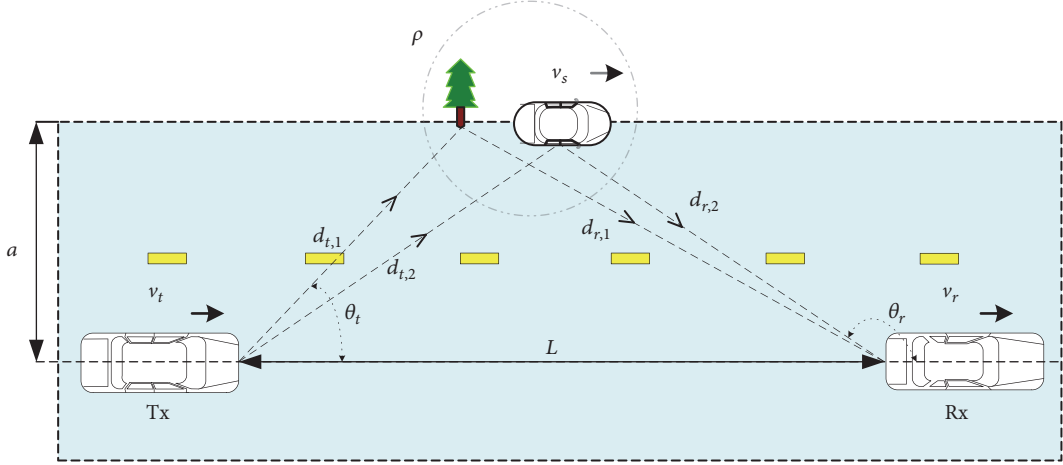


FIGURE 5: Real-world propagation scenario with one cluster between Tx and Rx.

the heights of antennas on vehicles are $h_t = h_r = 1.8$ m, giving a Fresnel distance of 255 m.

Thus, the modified PSD can be expressed as the following equation:

$$|S(f)| = \sum_{i=1}^n Q G_t(\theta_t) G_r(\theta_r) D(\hat{d}_t, \hat{d}_c) D(\hat{d}_r, \hat{d}_c) \frac{\csc^2 \theta_t}{|df/d\theta_t|}, \quad (12)$$

where $Q = P_t \lambda^2 \sigma \hat{\rho} a / (4\pi d_{tr})^3$, and $\hat{\rho} \equiv \rho/d_{tr}$ is the normalized perpendicular distance to the cluster. In addition, we can derive the angular power density from (7) as follows:

$$\begin{aligned} \frac{dP}{d\theta} &= |S(f)| \left| \frac{df}{d\theta_t} \right| \\ &= \sum_{i=1}^n Q G_t(\theta_t) G_r(\theta_r) D(\hat{d}_t, \hat{d}_c) D(\hat{d}_r, \hat{d}_c) \csc^2 \theta_t. \end{aligned} \quad (13)$$

3.5. Different Relative Locations of Clusters. Owing to the countless number of propagation environments combined with similar delays and angles, it is reasonable to describe the multipath components in terms of clusters. Since the above parameters to the geometry vary between different scenarios, it is needed to classify the V2V channels into three classes based upon the local physical environment.

(i) *Ahead*. Figure 3(a) shows the case when the cluster is ahead of both Tx and Rx. In this setting $0 < \theta_t \leq \theta_r < \pi/2$; we have

$$\hat{d}_t = \frac{\hat{a}}{\sin \theta_t}, \quad (14)$$

$$\hat{d}_r = \frac{\hat{a}}{\sin \theta_r}, \quad (15)$$

$$\hat{d}_r = \sqrt{\hat{a}^2 + (\hat{a}^2 \cot \theta_t - 1)^2}. \quad (15)$$

We can derive θ_r from Figure 3(a):

$$\theta_r = \tan^{-1} \left(\frac{\hat{a}}{\hat{a} \cot \theta_t - 1} \right). \quad (16)$$

Therefore,

$$\frac{d\theta_t}{d\theta_r} = \frac{(\hat{a}^2 \cot \theta_t - 1)^2 + \hat{a}^2}{\hat{a}^2 \csc^2 \theta_t}. \quad (17)$$

(ii) *Between*. Figure 3(b) depicts the case when the cluster is located in between Tx and Rx. In this setting $0 < \theta_t \leq \pi/2 \leq \theta_r < \pi$; θ_r can be derived from the graph as follows:

$$\theta_r = \pi - \tan^{-1} \left(\frac{\hat{a}}{1 - \hat{a} \cot \theta_t} \right). \quad (18)$$

As for the expressions of $|S(f)|$, \hat{d}_t , and \hat{d}_r , they are the same equation as in the “Ahead” setting.

(iii) *Behind*. Figure 3(c) represents the case when the cluster is behind both Tx and Rx. In this setting $\pi/2 \leq \theta_t < \theta_r < \pi$; also the expressions of $|S(f)|$, \hat{d}_t , and \hat{d}_r have the same form as in the “Ahead” setting.

4. SCM V2V Channel Characterization

Considering the geometrical model in Figure 5, scatterers are lying on the right or left side of the street. In the following part, we derive the corresponding autocorrelation function (ACF) of a cluster under the scenario of suburban roadside. Moving scatterers such as walking pedestrians and passing vehicles are unavoidable in V2V communications. In light of the real-world radio propagation environments, the complex channel gain $\mu(t)$ of SCM V2V channels can be represented

by the sum of stationary scatterers and moving scatterers located on the same clusters in the following form:

$$\begin{aligned}\mu(t) &= \sum_{i=1}^A a_i \exp [j(2\pi f_i t + \theta_i)] \\ &\quad + \sum_{n=1}^B b_n \exp [j(2\pi f_n t + \theta_n)] \\ &= \sum_{n=1}^N c_n \exp [j(2\pi f_n t + \theta_n)],\end{aligned}\quad (19)$$

where A and B are the number of stationary scatterers and moving scatterers in a cluster, respectively ($N = A + B$). a_i , b_n , and c_n designate the attenuation factors caused by the scattering objects. f_i and f_n represent the Doppler shift caused by stationary scatterers and moving scatterers, respectively. θ_i and θ_n denote the phase shift of the subpath, which is usually assumed to be uniformly distributed between 0 and 2π considering both left and right roadside. For the sake of brevity, this research only focuses on one direction only, ignoring the scenarios of opposite direction of moving vehicles. In [26], the frequency shift f_n can be written in the following compact form:

$$f_n = \frac{1}{\lambda} [\nu_t \cos \theta_t - \nu_s (\cos \theta_t + \cos \theta_r) + \nu_r \cos \theta_r]. \quad (20)$$

$$\begin{aligned}r_{\mu\mu}(\tau) &= 2\sigma_0^2 \int_0^\infty \int_0^{2\pi} \int_0^{2\pi} \exp \left\{ \frac{j2\pi\tau}{\lambda [\nu_t \cos \theta_t - 2\nu_s \cos((\theta_t + \theta_r)/2) \cos((\theta_t - \theta_r)/2) + \nu_r \cos \theta_r]} \right\} \times p_{\theta_t, \theta_r}(\theta_t, \theta_r) \\ &\quad \cdot p_{\nu_s}(\nu_s) d\theta_t d\theta_r d\nu_s.\end{aligned}$$

In [27, pp. 64], we derive the closed-form expression for the average Doppler spread $B_{\mu\mu}^{(1)}$ and Doppler spread $B_{\mu\mu}^{(2)}$, which can be derived from the first- and second-time derivative of ACF $r_{\mu\mu}(\tau)$ of the complex gain $\mu(t)$ as follows:

$$\begin{aligned}B_{\mu\mu}^{(1)} &= \frac{1}{2\pi j} \cdot \frac{\dot{r}_{\mu\mu}(0)}{r_{\mu\mu}(0)}, \\ B_{\mu\mu}^{(2)} &= \frac{1}{2\pi} \sqrt{\left(\frac{\dot{r}_{\mu\mu}(0)}{r_{\mu\mu}(0)} \right)^2 - \frac{\ddot{r}_{\mu\mu}(0)}{r_{\mu\mu}(0)}},\end{aligned}\quad (25)$$

where the $\dot{r}_{\mu\mu}(\tau)$ and $\ddot{r}_{\mu\mu}(\tau)$ indicate the first- and second-time derivative of $r_{\mu\mu}(\tau)$, respectively.

5. Simulation Results and Discussion

Having derived the basic channel characterization of the model, in this section, numerical simulation results are

Hence, the Doppler shift f_i of stationary scatterers can be obtained from (12) by setting $\nu_s = 0$. The ACF $r_{\mu\mu}(\tau)$ of V2V channel coefficient can be determined by the following definition:

$$r_{\mu\mu}(\tau) = E \{ \mu^*(t) \cdot \mu(t + \tau) \}, \quad (21)$$

where $E\{\cdot\}$ denotes the expectation operator. Substituting (19) in (21) gives us

$$\begin{aligned}r_{\mu\mu}(\tau) &= \sum_{n=1}^N \sum_{m=1}^M c_n c_m \\ &\quad \cdot E \{ \exp [j(2\pi t (f_m - f_n) + (\theta_m - \theta_n) + 2\pi f_m \tau)] \}.\end{aligned}\quad (22)$$

It is noteworthy that if the number of paths N tends to infinity, for any given isotropic scattering, hence all path gains c_n have the same fading coefficient. Regarding the fact that both random phases and Doppler frequencies are uniformly distributed with respect to $\Delta\theta \rightarrow 0$, (22) can be expressed by the following:

$$r_{\mu\mu}(\tau) = \lim_{N \rightarrow \infty} \sum_{n=1}^N c_n^2 E \{ \exp [j2\pi f_n \tau] \}. \quad (23)$$

Under the idealized assumption of isotropic scattering and AoA θ_n uniform distribution between 0 and 2π , it follows that all subpath gains $c_n = \sigma_0 \sqrt{2/N}$ have the same size [27]. In the case under consideration, the ACF of V2V channels can be represented as follows:

$$r_{\mu\mu}(\tau) = 2\sigma_0^2 \int_0^\infty \int_0^{2\pi} \int_0^{2\pi} \exp \left\{ \frac{j2\pi\tau}{\lambda [\nu_t \cos \theta_t - 2\nu_s \cos((\theta_t + \theta_r)/2) \cos((\theta_t - \theta_r)/2) + \nu_r \cos \theta_r]} \right\} \times p_{\theta_t, \theta_r}(\theta_t, \theta_r) \cdot p_{\nu_s}(\nu_s) d\theta_t d\theta_r d\nu_s. \quad (24)$$

provided to illustrate the validity of the proposed SCM V2V model.

5.1. PSD of the SCM V2V Channel. Figures 6, 7, and 8 show the PSD of the SCM V2V channel for different Tx/Rx vehicles velocity distributions. The results presented therein have been obtained by referring to (8)–(10). Parameter values used in Figures 6, 7, and 8 calculations are $P_t G_t G_r = 1$, $L = 20$ m, $a = 10$ m, $d_c = 255$ m, $\rho = 10$, $\sigma = 1$, and $f_c = 5.9$ GHz. It is needed to point out that we do not consider the speed of scatterers due to the fact that it is not a dominant source of PSD in V2V communications. As shown in Figure 6, scatterers are assumed to be in between Tx and Rx. The two vehicles are moving in the same direction. The first conclusion to this figure is that the cut-off frequency ranges of the spectrum are given by $\pm(\nu_t + \nu_r)/\lambda$, which is in agreement with the typical two-ring model and the existing literature [5]. By increasing the mean velocity of Tx/Rx vehicles, the central peak of PSD also increases by gradually approaching a delta function around the origin and decreases in tails. The

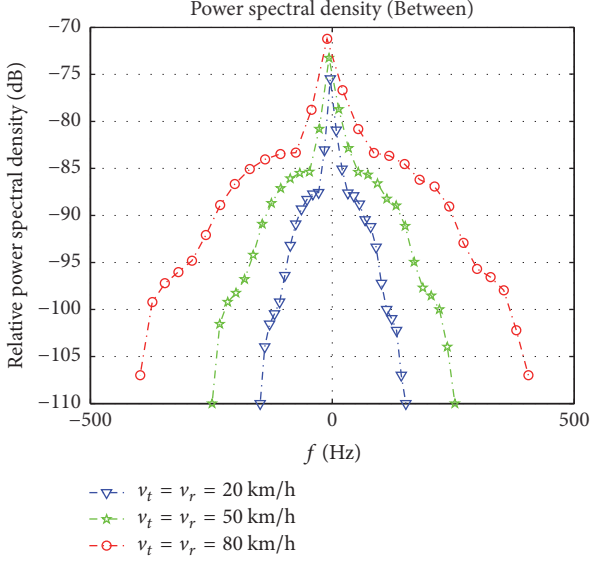


FIGURE 6: Behavior of PSD $S(f)$ presented in (10) and Figure 3(b) for V2V scenarios with different moving speeds of Tx/Rx vehicles.

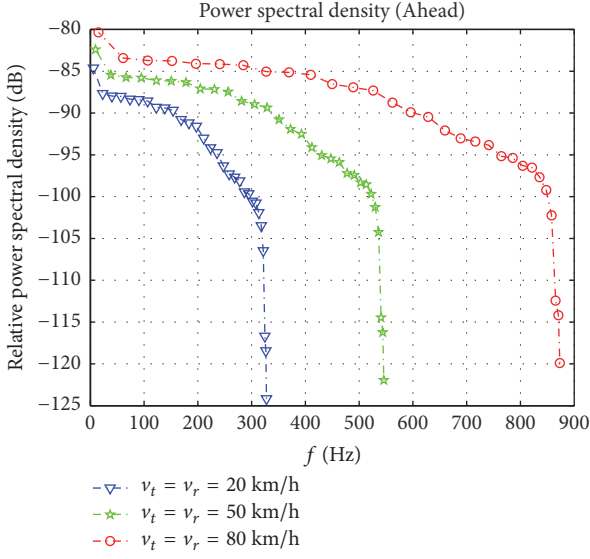


FIGURE 7: Behavior of PSD $S(f)$ presented in (10) and Figure 3(a) for V2V scenarios with different moving speeds of Tx/Rx vehicles.

spectrum is symmetric since both Tx and Rx are moving at the same speed. Furthermore, it can be observed that the Tx/Rx vehicles speed distribution has significant effect on both the magnitude and shape of the PSD in the presence of same clusters or scatterers. The PSD $S(f)$ of the proposed SCM V2V channel model is even and real, which also implies that the ACF $r_{\mu\mu}(\tau)$ is also even and real.

Figures 7 and 8 show the PSD of the proposed channel model under the scenarios of clusters located at “Ahead” and “Behind” position with respect to the Tx/Rx vehicles; it can be concluded that all spectrums become one-sided because of different distributions of AoDs θ_t and AoAs θ_r . However, the level of spectrum limits is close to the condition of “Between.”

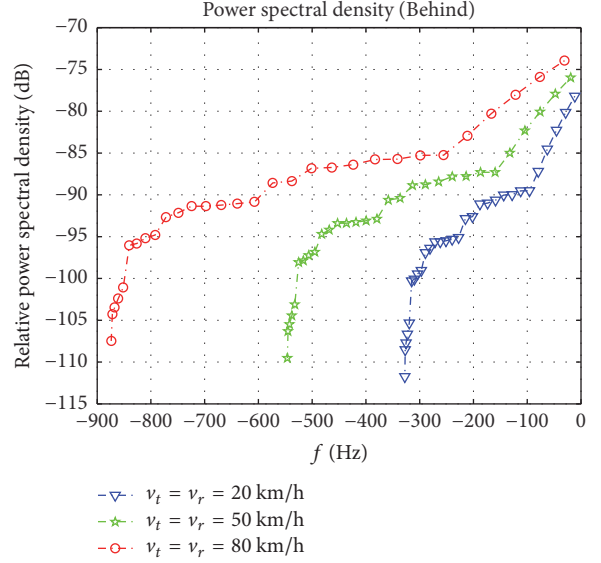


FIGURE 8: Behavior of PSD $S(f)$ presented in (10) and Figure 3(c) for V2V scenarios with different moving speeds of Tx/Rx vehicles.

Note that we have labeled the Tx/Rx physically meaningful to mimic V2V channels. One common understanding is that V2V channel is reciprocal [5]; the general shape of the spectrum between “Ahead” and “Behind” shows on a coarse symmetry regardless of which vehicle is the Tx or Rx. Compared with Figure 6, the PSD $S(f)$ of these two regions is odd and real, which is fundamentally different characteristic among Figures 6, 7, and 8. In contrast to our previous PSD, it is interesting to note that the angular power density is relatively smooth and has no apparent peak value due to the function $df/d\theta_t$ in (11).

5.2. ACF of the SCM V2V Channel. To illustrate the effect of moving scatterers and different positions of clusters on the ACF of SCM V2V channel model, 20 subpaths in each cluster are used for the simulation. The propagation environment contains moving clusters and fixed clusters, which are located in the three regions along the roadside. Both the transmitter and the receiver have the same speed in the same direction. Here, we consider the case of nonisotropic scattering conditions. The AoDs θ_t and AoAs θ_r are uniformly distributed over the three regions: “Ahead” ($0 < \theta_t \leq \theta_r < \pi/2$), “Between” ($0 < \theta_t \leq \pi/2 \leq \theta_r < \pi$), and “Behind” ($\pi/2 \leq \theta_t < \theta_r < \pi$), respectively. Consider subpaths in a cluster within the differential angle ($\Delta\theta_t \leq 1^\circ$, $\Delta\theta_r \leq 1^\circ$) about the angle θ_t and θ_r with respect to their neighbor subpaths. Each cluster has a length of 10 m and is independent with its neighbor clusters. The effective distance between scatterers and Tx/Rx is within 1 km range. For simplicity purposes, the attenuation factors c_n are all set to one.

Let us compare the effect of fixed scatterers and moving scatterers on the ACF $r_{\mu\mu}(\tau)$ illustrated in Figures 9, 10, and 11. Case 1: $v_t = v_r = 30 \text{ km/h}$, $v_s = 10 \text{ km/h}$; Case 2: $v_t = v_r = 80 \text{ km/h}$, $v_s = 30 \text{ km/h}$. It is noteworthy that as the speed of v_t and v_r increases, the coherence time of V2V

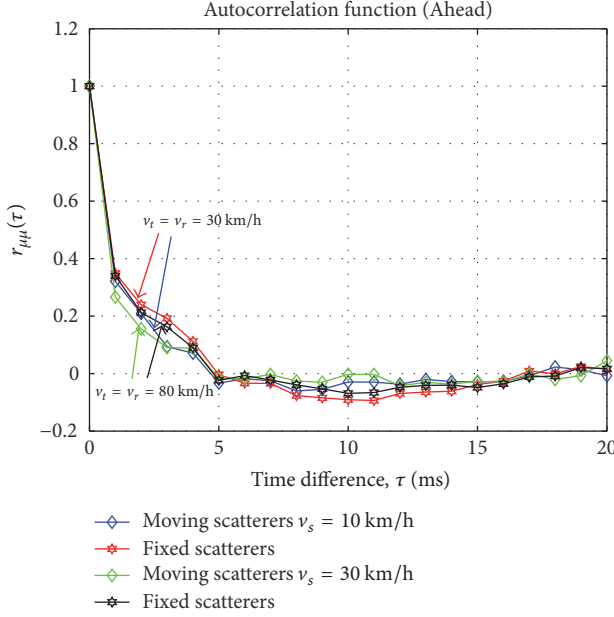


FIGURE 9: Behavior of ACF $r_{\mu\mu}(\tau)$ presented in Figure 3(a) for V2V scenarios (“Ahead” central angle: $\theta_t = 30^\circ$, $\theta_r = 60^\circ$ uniform distribution).

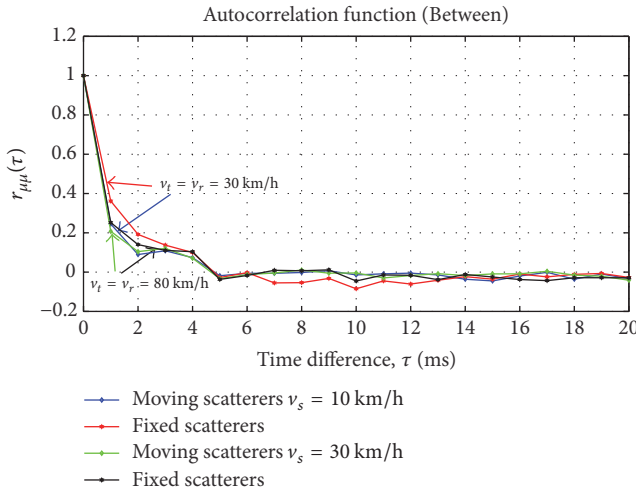


FIGURE 10: Behavior of ACF $r_{\mu\mu}(\tau)$ presented in Figure 3(b) for V2V scenarios (“Between” central angle: $\theta_t = 30^\circ$, $\theta_r = 120^\circ$ uniform distribution).

channels decreases. Figures 9, 10, and 11 also demonstrate the effect of moving scatterers on the ACF of V2V channels when the speed of Tx and Rx keeps in the same value. As the velocity of moving scatterers relatively to the Tx/Rx decreases, V2V channels change more slowly. To study the impact of slow moving scatterers, the average velocity v_s in both cases has been set to 10 km/h. Furthermore, one needs to compare the ACF in the presence of moving scatterers with that of fixed scatterers under the scenarios of clusters located at three positions. In this regard, Figure 9 shows that the ACF value of fixed scatterers of “Ahead” cluster is larger than that of

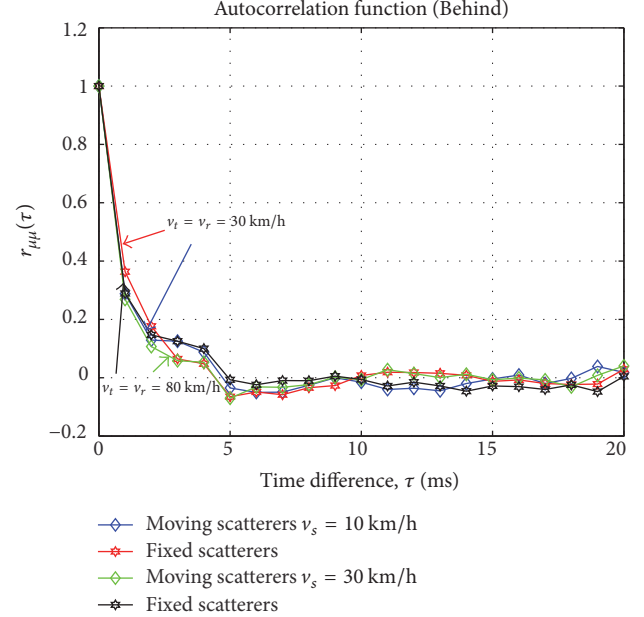


FIGURE 11: Behavior of ACF $r_{\mu\mu}(\tau)$ presented in Figure 3(c) for V2V scenarios (“Behind” central angle: $\theta_t = 120^\circ$, $\theta_r = 150^\circ$ uniform distribution).

other two regions. Figure 10 illustrates that the high speed of moving scatterers and Tx/Rx has relatively a little effect on the ACF of “Between” clusters. When the time difference τ exceeds a critical value 5 ms, the ACF values tend to be around zero. The general form of the ACF can be obtained by taking the inverse Fourier transform of the PSD in (10). Therefore, the simulation results are in very good agreement with the real world.

6. Summary and Conclusions

In this paper, a novel scattering cluster-based V2V channel model is proposed, which contributes to bridging the gap between simplified SCM models and computationally expensive geometry-based models by performing location-specific propagation modeling with respect to the moving and fixed scatterers in the vicinity of the communicating vehicles. The general PSD, angular power density, CIR, ACF, and the Doppler spread of the SCM V2V channel have been derived. Comparisons with three classes of clusters show that the proposed model describes the scattering component and properties more accurately than GBSMs (e.g., two-ring model). Furthermore, the effects of fixed scatterers and moving scatterers on the ACF of the new model have been studied. It has been shown that the moving scatterers have a relatively major impact on the V2V communication links as they can significantly affect the Doppler spread of the V2V channels. Numerical results are presented to validate the effectiveness of the proposed SCM V2V model in terms of the PSD, ACF, and CIR of the V2V channels. More investigations concerning other statistical properties of the V2V channel, for example, the influence of the opposite moving direction

of vehicles and different distributions of scatterers and the coherence time, may be addressed in future work.

List of Model Parameters in SCM-V2V Model

P_n :	Power of the n th path
N :	Number of clusters
M :	Number of subpaths per cluster
A_t :	Antenna gains of Tx
A_r :	Antenna gains of Rx
$\theta_{m,n,t}$:	AoD of the n th subpath of the m th cluster
$\theta_{m,n,r}$:	AoA of the n th subpath of the m th cluster
θ_v :	Angle of the Tx velocity vector
d_t :	Distance in meters from Tx antenna elements
d_r :	Distance in meters from Rx antenna elements
$\phi_{n,m}$:	Phase of the n th subpath of the m th cluster
k :	Wave number, $k = 2\pi/\lambda$
v :	Relative speed of the Tx.

Conflicts of Interest

The authors declare that they have no conflicts of interest.

Acknowledgments

This work is supported by the China Scholarship Council (CSC) and the National Natural Science Foundation of China under Grants nos. 61673253 and 61271213 and the Specialized Research Fund for the Doctoral Program of Higher Education of China under Grant no. 20133108110014.

References

- [1] T. Abbas, J. Nuckelt, T. Zemen, C. F. Mecklenbrauker, and F. Tufvesson, "Simulation and measurement-based vehicle-to-vehicle channel characterization: accuracy and constraint analysis," *Institute of Electrical and Electronics Engineers. Transactions on Antennas and Propagation*, vol. 63, no. 7, pp. 3208–3218, 2015.
- [2] X. Zhao, X. Liang, S. Li, and K. Haneda, "Mobile-to-Mobile Wideband MIMO Channel Realization by Using a Two-Ring Geometry-Based Stochastic Scattering Model," *Wireless Personal Communications*, vol. 84, no. 4, pp. 2445–2465, 2015.
- [3] A. B. Al-Khalil, S. Turner, and A. Al-Sherbaz, "Feasibility study of utilising SCM-MIMO channel model in V2V communication," in *Proceedings of the 2014 7th International Workshop on Communication Technologies for Vehicles, Nets4Cars-Fall 2014*, pp. 29–34, rus, October 2014.
- [4] D. W. Matolak, "Channel modeling for vehicle-to-vehicle communications," *IEEE Communications Magazine*, vol. 46, no. 5, pp. 76–83, 2008.
- [5] L. Cheng, D. D. Stancil, and F. Bai, "A roadside scattering model for the Vehicle-To-Vehicle communication channel," *IEEE Journal on Selected Areas in Communications*, vol. 31, no. 9, pp. 449–459, 2013.
- [6] A. G. Zajić and G. L. Stüber, "Three-dimensional modeling and simulation of wideband MIMO mobile-to-mobile channels," *IEEE Transactions on Wireless Communications*, vol. 8, no. 3, pp. 1260–1275, 2009.
- [7] R. B. Ertel and J. H. Reed, "Angle and time of arrival statistics for circular and elliptical scattering models," *IEEE Journal on Selected Areas in Communications*, vol. 17, no. 11, pp. 1829–1840, 1999.
- [8] S. J. Nawaz, M. Riaz, N. M. Khan, and S. Wyne, "Temporal analysis of a 3D ellipsoid channel model for the vehicle-to-vehicle communication environments," *Wireless Personal Communications*, vol. 82, no. 3, pp. 1337–1350, 2015.
- [9] X. Zhao, X. Liang, S. Li, and B. Ai, "Two-Cylinder and Multi-Ring GBSSM for Realizing and Modeling of Vehicle-to-Vehicle Wideband MIMO Channels," *IEEE Transactions on Intelligent Transportation Systems*, vol. 17, no. 10, pp. 2787–2799, 2016.
- [10] A. B. Al-Khalil, S. Turner, and A. Al-Sherbaz, "Utilising SCM – MIMO Channel Model Based on V-BLAST Channel Coding in V2V Communication," in *Communication Technologies for Vehicles*, vol. 9066 of *Lecture Notes in Computer Science*, pp. 3–11, Springer International Publishing, Sousse, Tunisia, 2015.
- [11] S. Jaeckel, K. Borner, L. Thiele, and V. Jungnickel, "A geometric polarization rotation model for the 3-D spatial channel model," *IEEE Transactions on Antennas and Propagation*, vol. 60, no. 12, pp. 5966–5977, 2012.
- [12] J. Karedal, F. Tufvesson, N. Czink et al., "A geometry-based stochastic MIMO model for vehicle-to-vehicle communications," *IEEE Transactions on Wireless Communications*, vol. 8, no. 7, pp. 3646–3657, 2009.
- [13] Y. Li, B. Ai, D. G. Michelson, S. Lin, Q. Wang, and Z. Zhong, "A method for generating correlated taps in stochastic vehicle-to-vehicle channel models," in *Proceedings of the 81st IEEE Vehicular Technology Conference, VTC Spring 2015*, 5, 1 pages, Glasgow, Scotland, May 2015.
- [14] A. Paier, T. Zemen, L. Bernadó et al., "Non-WSSUS vehicular channel characterization in highway and urban scenarios at 5.2 GHZ using the local scattering function," in *Proceedings of the 2008 International ITG Workshop on Smart Antennas, WSA 2008*, pp. 9–15, Darmstadt, Germany, February 2008.
- [15] Y. Li, B. Ai, X. Cheng, S. Lin, and Z. Zhong, "A TDL based non-WSSUS vehicle-to-vehicle channel model," *International Journal of Antennas and Propagation*, vol. 2013, Article ID 103461, 8 pages, 2013.
- [16] C.-X. Wang, X. Cheng, and D. I. Laurenson, "Vehicle-to-vehicle channel modeling and measurements: recent advances and future challenges," *IEEE Communications Magazine*, vol. 47, no. 11, pp. 96–103, 2009.
- [17] X. Liang, X. Zhao, S. Li, Q. Wang, and J. Li, "A non-stationary geometry-based scattering model for street vehicle-to-vehicle wideband MIMO channels," in *Proceedings of the 26th IEEE Annual International Symposium on Personal, Indoor, and Mobile Radio Communications, PIMRC 2015*, pp. 2239–2243, Hong Kong, China, September 2015.
- [18] Q. Fu and W. Chen, "A wideband MIMO vehicle-to-vehicle channel model in T-junction scattering environments," in *Proceedings of the in proceedings of IEEE 15th International Conference on Advanced Communications (ICACT)*, pp. 688–691, PyeongChang, Korea, 2013.
- [19] T. Abbas, L. Bernardo, A. Thiel, C. F. Mecklenbrauker, and F. Tufvesson, "Measurements based channel characterization for vehicle-to-vehicle communications at merging lanes on highway," in *Proceedings of the 2013 IEEE 5th International Symposium on Wireless Vehicular Communications, WiVeC 2013*, pp. 1–5, Dresden, Germany, June 2013.
- [20] Y. Yuan, C.-X. Wang, Y. He, M. M. Alwakeel, and E.-H. M. Aggoune, "3D Wideband Non-Stationary Geometry-Based

- Stochastic Models for Non-Isotropic MIMO Vehicle-to-Vehicle Channels,” *IEEE Transactions on Wireless Communications*, vol. 14, no. 12, pp. 6883–6895, 2015.
- [21] Y. Li, R. S. He, S. Lin et al., “Cluster-based non-stationary channel modeling for vehicle-to-vehicle communications,” *IEEE Antennas and Wireless Propagation Letters*, vol. 16, pp. 408–411, 2017.
- [22] “Spatial channel model for multiple input multiple output (MIMO) simulations, Tech. Rep.” Tech. Rep., 3GPP TR 25.996 v10.0.0, 2011.
- [23] A. F. Molisch, F. Tufvesson, J. Karedal, and C. F. Mecklenbräuker, “A survey on vehicle-to-vehicle propagation channels,” *IEEE Wireless Communications Magazine*, vol. 16, no. 6, pp. 12–22, 2009.
- [24] D. W. Matolak, “V2V Communication Channels: State of Knowledge, New Results, and What’s Next,” in *Communication Technologies for Vehicles*, vol. 7865 of *Lecture Notes in Computer Science*, pp. 1–21, Springer, Berlin, Germany, 2013.
- [25] L. Cheng, B. E. Henty, D. D. Stancil, F. Bai, and P. Mudalige, “Mobile vehicle-to-vehicle narrow-band channel measurement and characterization of the 5.9 ghz dedicated short range communication (dsrc) frequency band. Selected Areas in Communications,” *IEEE Journal on Selected Areas in Communications*, vol. 25, no. 8, pp. 1501–1516, 2007.
- [26] A. Borhani and M. Patzold, “Correlation and spectral properties of vehicle-to-vehicle channels in the presence of moving scatterers,” *IEEE Transactions on Vehicular Technology*, vol. 62, no. 9, pp. 4228–4239, 2013.
- [27] M. Pätzold, *Mobile Radio Channels*, Wiley, Chichester, UK, 2nd edition, 2011.

Research Article

An Efficient Hybrid Method for 3D Scattering from Inhomogeneous Object Buried beneath a Dielectric Randomly Rough Surface

Hong-jie He, Li-xin Guo, and Wei Liu

School of Physics and Optoelectronic Engineering, Xidian University, Xi'an 710071, China

Correspondence should be addressed to Hong-jie He; hongjiewuli2009@163.com

Received 3 May 2017; Accepted 3 July 2017; Published 28 August 2017

Academic Editor: Pasquale Imperatore

Copyright © 2017 Hong-jie He et al. This is an open access article distributed under the Creative Commons Attribution License, which permits unrestricted use, distribution, and reproduction in any medium, provided the original work is properly cited.

An efficient iterative analytical-numerical method is proposed for three-dimensional (3D) electromagnetic scattering from an inhomogeneous object buried beneath a two-dimensional (2D) randomly dielectric rough surface. In the hybrid method, the electric and magnetic currents on the dielectric rough surface are obtained by current-based Kirchhoff approximation (KA), while the scattering from the inhomogeneous object is rigorously studied by finite element method (FEM) combined with the boundary integral method (BIM). The multiple interactions between the buried object and rough surface are taken into account by updating the electric and magnetic current densities on them. Several numerical simulations are considered to demonstrate the algorithm's ability to deal with the scattering from the inhomogeneous target buried beneath a dielectric rough surface, and the effectiveness of our proposed method is also illustrated.

1. Introduction

The scattering from an object buried beneath a randomly dielectric rough surface which can be modelled as sea surface and sands is a subject of great interest in many applications, for example, geophysical exploration, buried target detection, and remote sensing. Many researchers have paid much attention to this problem and many numerical methods have been proposed in the past decades. The method of moments (MoM) was applied to discuss the scattering from a rough surface with a two-dimensional (2D) target in [1, 2]. The MoM with the dyadic Green's function of the background medium is applied in [3] to study the forward-scattering problem of three-dimensional (3D) objects buried under a 2D locally rough surface. To improve the computational efficiency and reduce the memory requirement, some asymptotic methods and hybrid methods are developed to study the scattering from a target buried beneath the rough surface. The cylindrical wave approach combined with the first-order small perturbation method (SPM) [4] was applied in [5] to study the scattering from a cylinder buried below a slightly

rough surface. The SPM was applied to study the electromagnetic scattering from a 2D dielectric cylinder buried beneath a slightly rough surface [6]. The second-order small slope approximation was used in [7] to study the scattering from one dimensional (1D) sea surface. The fields scattered by an object below a rough surface were computed by the efficient propagation-inside-layer-expansion (PILE) method combined with the physical optics approximation [8]. Hybrid KA-BIM was proposed in [9] to study the scattering from a 2D target buried beneath a rough surface. An efficient hybrid KA-MoM was proposed to analyse the electromagnetic scattering from a 3D perfectly electric conducting (PEC) object buried beneath a dielectric rough surface [10]. However, these numerical methods and hybrid methods mentioned above, for both 2D and 3D scattering problems, are applicable to PEC or dielectric objects. They all suffer the inconvenience of dealing with the scattering from inhomogeneous objects buried beneath dielectric rough surface.

For general inhomogeneous objects, the volume integral equation method is suitable. A fast volume integral equation algorithm with dyadic Green's function [11] was

developed to simulate the electromagnetic scattering from large inhomogeneous objects embedded in a planarly layered medium. The other appropriate choice for inhomogeneous objects is the finite element method (FEM) combined with the boundary integral method (BIM). The hybrid FEM/BIM method with the layered medium dyadic Green's function [12] was proposed to predict the scattering from inhomogeneous dielectric objects embedded in multilayered medium. But these methods cannot be applied to deal with the scattering from inhomogeneous object buried beneath randomly rough surface, since the analytical expression of the dyadic Green's function for the half space with rough surface can hardly be obtained. A hybrid FEM/MoM was applied in [13] to study the scattering from a 3D dielectric object above a 2D conductive rough surface. The FEM/BIM combined with KA was used in [14] to model the scattering from a 3D coated target above 2D PEC rough surface. The efficient and accurate modelling of inhomogeneous object buried beneath the randomly dielectric rough surface is still a challenging problem.

In this paper, a hybrid method is firstly designed for the fast and accurate solution of the 3D scattering problem related to a 3D inhomogeneous target buried beneath a 2D randomly dielectric rough surface. In order to achieve a significant reduction in CPU time and memory requirements, the asymptotic current-based KA is applied in the hybrid method to obtain the electric and magnetic current densities on the dielectric rough surface. To model the scattering from the buried inhomogeneous target, the powerful FEM/BIM is used in this paper. The multiple interactions between the target and rough surface are taken into account by updating the electric and magnetic fields on them. The accuracy of our hybrid method has been proven by comparing the results with that of the numerical method. And the effectiveness of our hybrid method is also discussed.

2. Hybrid Theory and Formulations

The geometry of the electromagnetic scattering problem is depicted in Figure 1. The whole space is separated into two half-spaces by the rough surface Γ_{KA} , which can be defined by a function $z = f(x, y)$ with mean $\langle f(x, y) \rangle = 0$. The rough surface generated by using the Monte-Carlo method based on the corresponding power spectrum function is confined to a square region $L = L_x = L_y$ on x - y plane of Cartesian coordinate system. The 2D Gaussian roughness spectrum used in this paper is given by

$$S(k_x, k_y) = \delta^2 \frac{l_x l_y}{4\pi} \exp\left(-\frac{k_x^2 l_x^2 + k_y^2 l_y^2}{4}\right), \quad (1)$$

where δ is the root-mean-square height of the rough surface, l_x and l_y are the correlation lengths in the \hat{x} and \hat{y} directions, respectively, and k_x and k_y are the spatial frequencies in the \hat{x} and \hat{y} directions, respectively.

The half-spaces above and below the rough surface are marked as region 1 and region 2, respectively. The permittivity and permeability of region i are ϵ_i and μ_i , respectively. The inhomogeneous target buried in region 2 is bounded by Γ_{BIM} .

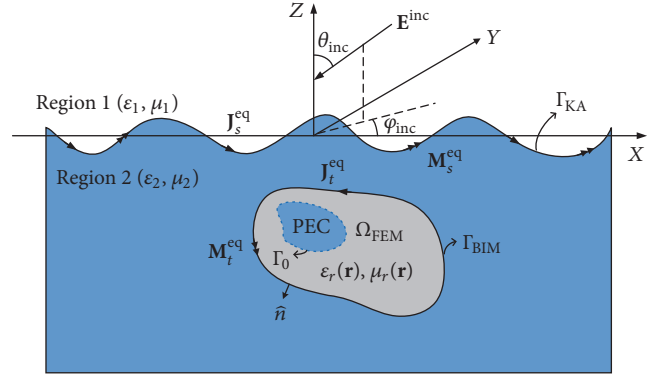


FIGURE 1: Geometry of the scattering problem of a 3D complex dielectric object buried under a 2D randomly dielectric rough surface.

The interior region Ω_{FEM} of the target can be composed of inhomogeneous dielectric objects with complex relative permittivity $\epsilon_r(\mathbf{r})$ and permeability $\mu_r(\mathbf{r})$, and PEC. To reduce the edge effects caused by the truncation of the finite surface length, the rough surface is illuminated by a TE polarized tapered wave [15] in this paper. The source of the tapered wave is in region 1 and the tapered wave can be expressed as

$$\mathbf{E}^{inc}(\mathbf{r}) = \exp[-j\mathbf{k}_1 \cdot \mathbf{r}(1+w)] \exp(-t_x - t_y), \quad (2)$$

where

$$w = \frac{1}{k_1^2} \left[\frac{2t_x - 1}{g^2 \cos^2 \theta_{inc}} + \frac{2t_y - 1}{g^2} \right]$$

$$t_x = \frac{(\cos \theta_{inc} \cos \varphi_{inc} x + \cos \theta_{inc} \sin \varphi_{inc} y + \sin \theta_{inc} z)^2}{g^2 \cos^2 \theta_{inc}} \quad (3)$$

$$t_y = \frac{(-\sin \varphi_{inc} x + \cos \varphi_{inc} y)^2}{g^2},$$

where θ_{inc} and φ_{inc} are the incident angles, g is the tapered factor, and k_1 is the wavenumber in the half space above the rough surface.

Hybrid FEM/BIM is a powerful technique to deal with the inhomogeneous media problem due to the differential equation nature. As shown in Figure 1, region 2 can be decomposed into two parts by boundary Γ_{BIM} , the interior region Ω_{FEM} , and the outer region. In FEM/BIM, the interior region Ω_{FEM} is analysed by FEM and the outer region is modelled by BIM, which naturally satisfies the radiation condition. The interior field and the outer field are coupled together via the field continuity conditions on the boundary Γ_{BIM} .

In the FEM region Ω_{FEM} , the electric field satisfies the following Helmholtz's equation:

$$\nabla \times \left(\frac{1}{\mu_r(\mathbf{r})} \nabla \times \mathbf{E}(\mathbf{r}) \right) - k_0^2 \epsilon_r(\mathbf{r}) \mathbf{E}(\mathbf{r}) = -jk_0 \eta_0 \mathbf{J}(\mathbf{r}) \quad (4)$$

$$(\mathbf{r} \in \Omega_{FEM}),$$

where k_0 is the free-space wavenumber, $\mathbf{J}(\mathbf{r})$ is the electric current in the space, η_0 is the free-space intrinsic impedance, and $\mathbf{E}(\mathbf{r})$ is the total electric field.

Based on the theory of functional analysis, the equivalent variational problem can be formulated as [16]

$$\begin{aligned} \delta F(\mathbf{E}) &= 0 \\ \hat{n} \times \mathbf{E}(\mathbf{r}) &= 0 \quad \mathbf{r} \in \Gamma_0, \end{aligned} \quad (5)$$

where

$$F(\mathbf{E}) = \frac{1}{2}$$

$$\begin{aligned} &\cdot \iiint_{\Omega_{\text{FEM}}} \left[\frac{1}{\mu_r(\mathbf{r})} (\nabla \times \mathbf{E}) \cdot (\nabla \times \mathbf{E}) - k_0^2 \epsilon_r(\mathbf{r}) \mathbf{E} \cdot \mathbf{E} \right] dV \quad (6) \\ &- jk_0 \eta_0 \oint_{\Gamma_{\text{BIM}}} \mathbf{E} \cdot (\hat{n} \times \mathbf{H}_t^{\text{scat}}) dS, \end{aligned}$$

where \hat{n} is the out-ward unit vector normal to boundary Γ_{BIM} and $\mathbf{H}_t^{\text{scat}}$ is the magnetic field scattered by the target on the boundary Γ_{BIM} . Discretizing the FEM region with tetrahedral elements, the fields can be expanded by the vector basis function [16] $\mathbf{N}_m(\mathbf{r})$:

$$\begin{aligned} \mathbf{E}(\mathbf{r}) &= \sum_{m=1}^M E_m \mathbf{N}_m(\mathbf{r}) \\ \mathbf{H}(\mathbf{r}) &= \sum_{m=1}^M H_m \mathbf{N}_m(\mathbf{r}), \end{aligned} \quad (7)$$

where M is the number of the vector bases defined in FEM region. Then the following weak form of the matrix equation can be obtained:

$$\begin{aligned} &\iiint_{\Omega_{\text{FEM}}} \left[\frac{1}{\mu_r(\mathbf{r})} (\nabla \times \mathbf{N}_i) \cdot (\nabla \times \mathbf{E}) - k_0^2 \epsilon_r(\mathbf{r}) \mathbf{N}_i \cdot \mathbf{E} \right] dV \\ &- jk_0 \eta_0 \int \int_{\Gamma_{\text{BIM}}} \mathbf{N}_i \cdot (\hat{n} \times \mathbf{H}_t^{\text{scat}}) dS = 0. \end{aligned} \quad (8)$$

The outer region can be modelled by the integral equation method. The total electric field $\mathbf{E}(\mathbf{r})$ in the outer region satisfies the following integral equation:

$$\mathbf{E}(\mathbf{r}) - \mathbf{E}_t^{\text{scat}}(\mathbf{r}) = \mathbf{E}_s^{\text{scat}}(\mathbf{r}), \quad (9)$$

where $\mathbf{E}_s^{\text{scat}}(\mathbf{r})$ is the field excited by the equivalent surface electric and magnetic currents (\mathbf{J}_s^{eq} and \mathbf{M}_s^{eq}) on the rough surface, which act as the source illuminating on the target. $\mathbf{E}_t^{\text{scat}}(\mathbf{r})$ is the field excited by the equivalent surface electric and magnetic currents (\mathbf{J}_t^{eq} and \mathbf{M}_t^{eq}) on the boundary Γ_{BIM} . The fields $\mathbf{E}_t^{\text{scat}}(\mathbf{r})$ and $\mathbf{E}_s^{\text{scat}}(\mathbf{r})$ can be obtained from the following expressions, respectively:

$$\mathbf{E}_t^{\text{scat}}(\mathbf{r}) = \eta_2 \mathbf{L}_2(\mathbf{J}_t^{\text{eq}}) - \mathbf{K}_2(\mathbf{M}_t^{\text{eq}}) \quad (10)$$

$$\mathbf{E}_s^{\text{scat}}(\mathbf{r}) = -\eta_2 \mathbf{L}_2(\mathbf{J}_s^{\text{eq}}) + \mathbf{K}_2(\mathbf{M}_s^{\text{eq}}). \quad (11)$$

The operators \mathbf{L}_i and \mathbf{K}_i are defined as

$$\begin{aligned} \mathbf{L}_i(\mathbf{X}) &= -jk_i \int \int_{\Gamma} \mathbf{X}(\mathbf{r}') G_i(\mathbf{r}, \mathbf{r}') + \frac{1}{k_i^2} \nabla' \\ &\cdot \mathbf{X}(\mathbf{r}') \nabla G_i(\mathbf{r}, \mathbf{r}') d\Gamma' \\ \mathbf{K}_i(\mathbf{X}) &= - \int \int_{\Gamma} \mathbf{X}(\mathbf{r}') \times \nabla G_i(\mathbf{r}, \mathbf{r}') d\Gamma'. \end{aligned} \quad (12)$$

The symbols η_i , k_i , and G_i are the complex impedance, the wavenumber, and Green's function associated with region i , respectively. The expression of the Green's function G_i is given by

$$G_i(\mathbf{r}, \mathbf{r}') = \frac{e^{-jk_i |\mathbf{r}-\mathbf{r}'|}}{4\pi |\mathbf{r}-\mathbf{r}'|}, \quad (13)$$

where \mathbf{r}' and \mathbf{r} are the position vectors of the source and observation points, respectively.

On the boundary Γ_{BIM} , the equivalent electric and magnetic currents (\mathbf{J}_t^{eq} and \mathbf{M}_t^{eq}) have the relation with surface fields as $\mathbf{J}_t^{\text{eq}} = \hat{n} \times \mathbf{H}_t^{\text{scat}}$ and $\mathbf{M}_t^{\text{eq}} = -\hat{n} \times \mathbf{E}_t^{\text{scat}}$, respectively. Then the electric and magnetic currents on the boundary can be discretized as

$$\begin{aligned} \mathbf{J}_t^{\text{eq}}(\mathbf{r}) &= \sum_{n=1}^{N_t} H_n \mathbf{f}_n(\mathbf{r}) \\ \mathbf{M}_t^{\text{eq}}(\mathbf{r}) &= \sum_{n=1}^{N_t} E_n \mathbf{f}_n(\mathbf{r}), \end{aligned} \quad (14)$$

where $\mathbf{f}_n(\mathbf{r})$ is the Rao-Wilton-Glisson (RWG) basis functions which have relation with $\mathbf{N}_n(\mathbf{r})$ as $\mathbf{f}_n(\mathbf{r}) = -\hat{n} \times \mathbf{N}_n(\mathbf{r})$. When MoM is applied, the following matrix equations can be obtained by discretizing (9):

$$[P] \{E\} + [Q] \{H\} = \{b\}, \quad (15)$$

where $[P]$ and $[Q]$ are the impedance matrices and $\{b\}$ is the vector related to the fields scattered from the rough surface. And they can be obtained by the following expressions:

$$P_{mn}$$

$$= \left\langle \mathbf{f}_m(\mathbf{r}), \mathbf{N}_n(\mathbf{r}) + \int_{S_n} \mathbf{f}_n(\mathbf{r}') \times \nabla' G_2(\mathbf{r}, \mathbf{r}') dS' \right\rangle$$

$$Q_{mn}$$

$$= \left\langle \mathbf{f}_m(\mathbf{r}), jk_2 \eta_2 \int_{S_n} \mathbf{f}_n(\mathbf{r}') G_2(\mathbf{r}, \mathbf{r}') dS' \right\rangle \quad (16)$$

$$+ \left\langle \mathbf{f}_m(\mathbf{r}), \frac{j\eta_2}{k_2} \int_{S_n} [\nabla' \cdot \mathbf{f}_n(\mathbf{r}')] \nabla G_2(\mathbf{r}, \mathbf{r}') dS' \right\rangle$$

$$b_m = \left\langle \mathbf{f}_m(\mathbf{r}), \mathbf{E}_s^{\text{scat}}(\mathbf{r}') \right\rangle.$$

Then we can obtain the final matrix equation for the scattering problem of the inhomogeneous target buried under the dielectric rough surface as

$$\begin{bmatrix} K_{II} & K_{IS} & 0 \\ K_{SI} & K_{SS} & C \\ 0 & P & Q \end{bmatrix} \begin{bmatrix} E_I \\ E_S \\ H_S \end{bmatrix} = \begin{bmatrix} 0 \\ 0 \\ b \end{bmatrix}, \quad (17)$$

where $[K_{II}]$, $[K_{IS}]$, $[K_{SI}]$, and $[K_{SS}]$ are the FEM matrices. The subscript I is denoting in the interior region Ω_{FEM} and subscript S is denoting on the boundary Γ_{BIM} . $[C]$ is the coupling matrix between FEM and BIM. $[K]$ and $[C]$ can be represented by the following expressions, respectively:

$$K_{mn} = \iiint_{\Omega} \frac{1}{\mu_r} (\nabla \times \mathbf{N}_m) \cdot (\nabla \times \mathbf{N}_n) - k_0^2 \epsilon_r \mathbf{N}_m \cdot \mathbf{N}_n dV \quad (18)$$

$$C_{mn} = jk_0 \eta_0 \iint_{\Gamma_m} \mathbf{N}_m \cdot (\hat{\mathbf{n}} \times \mathbf{N}_n) dS.$$

Note that the effects of the rough surface are considered in (17) as terms $[b]$. To get the field $\mathbf{E}_s^{\text{scat}}$ scattered from the rough surface, we should firstly compute the equivalent surface electric and magnetic currents (\mathbf{J}_s^{eq} and \mathbf{M}_s^{eq}) on the rough surface. They can be rigorously achieved by solving the following integral equations with MoM:

$$\begin{aligned} & -\eta_2 \mathbf{L}_2(\mathbf{J}_s^{\text{eq}}) - \eta_1 \mathbf{L}_1(\mathbf{J}_s^{\text{eq}}) + \mathbf{K}_2(\mathbf{M}_s^{\text{eq}}) + \mathbf{K}_1(\mathbf{M}_s^{\text{eq}}) \\ &= \mathbf{E}^{\text{inc}} - \mathbf{E}_t^{\text{scat}} \\ & - \mathbf{K}_2(\mathbf{J}_s^{\text{eq}}) - \mathbf{K}_1(\mathbf{J}_s^{\text{eq}}) - \frac{1}{\eta_1} \mathbf{L}_1(\mathbf{M}_s^{\text{eq}}) - \frac{1}{\eta_2} \mathbf{L}_2(\mathbf{M}_s^{\text{eq}}) \\ &= \mathbf{H}^{\text{inc}} - \mathbf{H}_t^{\text{scat}}. \end{aligned} \quad (19)$$

However, solving these integral equations with MoM is very time-consuming and requires a great amount of storage memory, especially for 3D electrically large rough surface. To reduce the computation time and memory requirement, analytical KA is a good choice.

Based on the superposition principle, the electric and magnetic currents on the rough surface can be represented by the combination of two independent parts as

$$\mathbf{J}_s^{\text{eq}} = \mathbf{J}_s^{\text{inc}} + \mathbf{J}_s^{\text{obj}} \quad (20)$$

$$\mathbf{M}_s^{\text{eq}} = \mathbf{M}_s^{\text{inc}} + \mathbf{M}_s^{\text{obj}}, \quad (21)$$

where $\mathbf{J}_s^{\text{inc}}$ and $\mathbf{M}_s^{\text{inc}}$ are the electric and magnetic currents induced by the incident wave in the absence of the buried target. $\mathbf{J}_s^{\text{obj}}$ and $\mathbf{M}_s^{\text{obj}}$ are the electric and magnetic currents generated by the fields scattered by the buried target in the absence of the incident wave source.

According to the KA theory and equivalent principle, the electric and magnetic currents ($\mathbf{J}_s^{\text{inc}}$ and $\mathbf{M}_s^{\text{inc}}$) at any point \mathbf{r} can be expressed as

$$\begin{aligned} \mathbf{J}_s^{\text{inc}} &= \hat{\mathbf{n}}_s \times \left[\frac{(1 + R_U^{\text{TM}})(\hat{\mathbf{p}}_i \cdot \mathbf{E}^{\text{inc}})}{\eta_1} \hat{\mathbf{q}}_i \right. \\ &\quad \left. - \frac{(\hat{\mathbf{q}}_i \cdot \mathbf{E}^{\text{inc}})}{\eta_1} (\hat{\mathbf{p}}_i - R_U^{\text{TE}} \hat{\mathbf{k}}_r \times \hat{\mathbf{q}}_i) \right], \end{aligned} \quad (22)$$

$$\begin{aligned} \mathbf{M}_s^{\text{inc}} &= -\hat{\mathbf{n}}_s \times \left[(1 + R_U^{\text{TE}})(\hat{\mathbf{q}}_i \cdot \mathbf{E}^{\text{inc}}) \hat{\mathbf{q}}_i \right. \\ &\quad \left. + (\hat{\mathbf{p}}_i \cdot \mathbf{E}^{\text{inc}})(\hat{\mathbf{p}}_i - R_U^{\text{TM}} \hat{\mathbf{k}}_r \times \hat{\mathbf{q}}_i) \right], \end{aligned} \quad (23)$$

where $(\hat{\mathbf{p}}_i, \hat{\mathbf{q}}_i, \hat{\mathbf{k}}_{\text{inc}})$ is a local orthonormal basis established at any point \mathbf{r} on the rough surface. The symbol $\hat{\mathbf{k}}_{\text{inc}}$ is the unit incident wave vector. The unit vectors $\hat{\mathbf{p}}_i$ and $\hat{\mathbf{q}}_i$ are the local perpendicular and parallel polarization vectors, respectively, which can be defined as

$$\begin{aligned} \hat{\mathbf{q}}_i(\mathbf{r}) &= \frac{\hat{\mathbf{k}}_{\text{inc}} \times \hat{\mathbf{n}}_s(\mathbf{r})}{\|\hat{\mathbf{k}}_{\text{inc}} \times \hat{\mathbf{n}}_s(\mathbf{r})\|} \\ \hat{\mathbf{p}}_i(\mathbf{r}) &= \hat{\mathbf{q}}_i(\mathbf{r}) \times \hat{\mathbf{k}}_{\text{inc}}. \end{aligned} \quad (24)$$

The symbol $\hat{\mathbf{k}}_r$ is the unit local reflection direction vector. Based on the tangent plane approximation, $\hat{\mathbf{k}}_r = \hat{\mathbf{k}}_{\text{inc}} - 2\hat{\mathbf{n}}_s(\hat{\mathbf{n}}_s \cdot \hat{\mathbf{k}}_{\text{inc}})$. R_U^{TE} and R_U^{TM} are the local Fresnel reflection coefficients of TE polarization and TM polarization, respectively, which can be expressed as

$$\begin{aligned} R_U^{\text{TE}} &= \frac{\cos \theta_{li} - \sqrt{\varepsilon_{2r} - \sin^2 \theta_{li}}}{\cos \theta_{li} + \sqrt{\varepsilon_{2r} - \sin^2 \theta_{li}}} \\ R_U^{\text{TM}} &= \frac{\varepsilon_{2r} \cos \theta_{li} - \sqrt{\varepsilon_{2r} - \sin^2 \theta_{li}}}{\varepsilon_{2r} \cos \theta_{li} + \sqrt{\varepsilon_{2r} - \sin^2 \theta_{li}}}, \end{aligned} \quad (25)$$

where θ_{li} is the local incident angle on the rough surface which satisfies $\cos \theta_{li} = -\hat{\mathbf{n}}_s \cdot \hat{\mathbf{k}}_i$ and ε_{2r} is the relative permittivity of region 2.

Similarly, the electric and magnetic currents ($\mathbf{J}_s^{\text{obj}}$ and $\mathbf{M}_s^{\text{obj}}$) generated by the fields scattered by the buried target can be expressed as

$$\begin{aligned} \mathbf{J}_s^{\text{obj}} &= \hat{\mathbf{n}}_s \times \left[\frac{(1 + R_D^{\text{TM}})(\hat{\mathbf{p}}_s \cdot \mathbf{E}_t^{\text{scat}})}{\eta_2} \hat{\mathbf{q}}_s \right. \\ &\quad \left. - \frac{(\hat{\mathbf{q}}_s \cdot \mathbf{E}_t^{\text{scat}})}{\eta_2} (\hat{\mathbf{p}}_s - R_D^{\text{TE}} \hat{\mathbf{k}}_{rs} \times \hat{\mathbf{q}}_s) \right], \end{aligned} \quad (26)$$

$$\begin{aligned} \mathbf{M}_s^{\text{obj}} &= -\hat{\mathbf{n}}_s \times \left[(1 + R_D^{\text{TE}})(\hat{\mathbf{q}}_s \cdot \mathbf{E}_t^{\text{scat}}) \hat{\mathbf{q}}_s \right. \\ &\quad \left. + (\hat{\mathbf{p}}_s \cdot \mathbf{E}_t^{\text{scat}})(\hat{\mathbf{p}}_s - R_D^{\text{TM}} \hat{\mathbf{k}}_{rs} \times \hat{\mathbf{q}}_s) \right], \end{aligned} \quad (27)$$

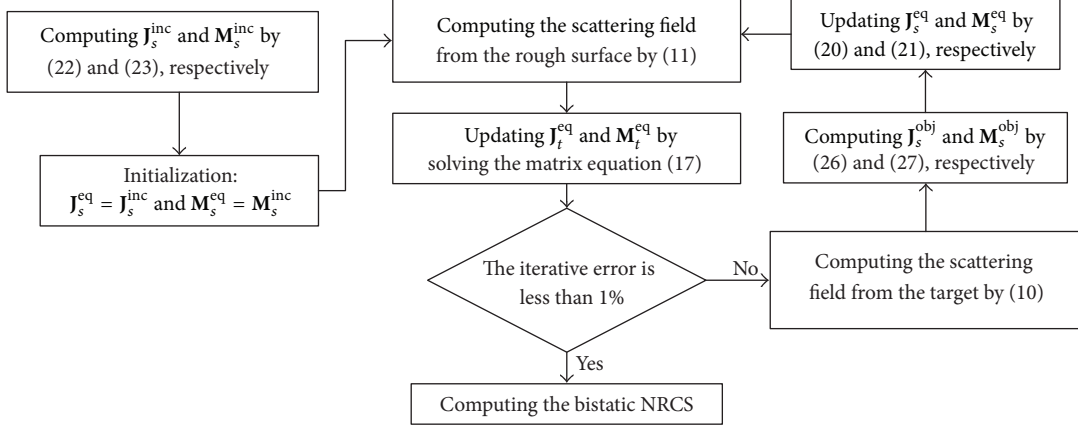


FIGURE 2: The flowchart of the iterative method.

where $(\hat{p}_s, \hat{q}_s, \hat{r}_s)$ is a local orthonormal basis established at any point \mathbf{r} on the rough surface. \hat{r}_s is the unit vector from the source point \mathbf{r}' on the target to the field point \mathbf{r} on the rough surface, which satisfies $\hat{r}_s = (\mathbf{r} - \mathbf{r}')/\|\mathbf{r} - \mathbf{r}'\|$. The unit vectors \hat{p}_s and \hat{q}_s are the local perpendicular and parallel polarization vectors, respectively, which can be defined as

$$\begin{aligned}\hat{q}_s(\mathbf{r}) &= \frac{\hat{r}_s \times \hat{n}_s(\mathbf{r})}{\|\hat{r}_s \times \hat{n}_s(\mathbf{r})\|} \\ \hat{p}_s(\mathbf{r}) &= \hat{q}_s(\mathbf{r}) \times \hat{r}_s,\end{aligned}\quad (28)$$

where \hat{k}_{rs} is the unit local reflection direction of the wave induced by the electric and magnetic currents on the target, which act as another incident source illuminating on the rough surface from the bottom. R_D^{TE} and R_D^{TM} are the local Fresnel reflection coefficients of TE polarization and TM polarization, respectively, which can be expressed as

$$\begin{aligned}R_D^{\text{TE}} &= \frac{\sqrt{\varepsilon_{2r}} \cos \theta_{ls} - \sqrt{1 - \varepsilon_{2r} \sin^2 \theta_{ls}}}{\sqrt{\varepsilon_{2r}} \cos \theta_{ls} + \sqrt{1 - \varepsilon_{2r} \sin^2 \theta_{ls}}} \\ R_D^{\text{TM}} &= \frac{\cos \theta_{ls} - \sqrt{\varepsilon_{2r}} \sqrt{1 - \varepsilon_{2r} \sin^2 \theta_{ls}}}{\cos \theta_{ls} + \sqrt{\varepsilon_{2r}} \sqrt{1 - \varepsilon_{2r} \sin^2 \theta_{ls}}},\end{aligned}\quad (29)$$

where θ_{ls} is the local incident angle and satisfies $\cos \theta_{ls} = \hat{n}_s(\mathbf{r}) \cdot \hat{r}_s$.

Then the scattering information from the rough surface can be obtained by (20), (22), and (26), if the scattering field $\mathbf{E}_t^{\text{scat}}$ from the target is calculated beforehand. It should be pointed out that, since the scattering from the rough surface is considered by KA, the limitation of KA [17] should be taken into account in our hybrid method; namely, the curvature radius ρ of the rough surface should be very large compared to the wavelength of the incident wave, $\rho \gg \lambda$.

The multiple interaction between the rough surface and the buried target can be taken into account by an iterative approach. To give a clearer depiction, the iterative process in

our method is shown in Figure 2. The iterative error at the i th iteration is defined as

$$\gamma_i = \frac{\|\mathbf{J}_t^i - \mathbf{J}_t^{i-1}\|}{\|\mathbf{J}_t^i\|}. \quad (30)$$

Once the scattering information from the rough surface is obtained, the bistatic normalized radar cross-section (NRCS) can be calculated by

$$\text{NRCS} = \lim_{r \rightarrow \infty} r^2 \frac{\|\mathbf{E}^{\text{scat}}\|^2}{P_{\text{inc}}}, \quad (31)$$

where \mathbf{E}^{scat} is the field scattered by the rough surface at any point \mathbf{r} in the region 1, which can be obtained with the following expression:

$$\mathbf{E}^{\text{scat}} = \eta_1 \mathbf{L}_1(\mathbf{J}_s^{\text{eq}}) - \mathbf{K}_1(\mathbf{M}_s^{\text{eq}}). \quad (32)$$

The symbol P^{inc} is the incident beam power which can be given by

$$P^{\text{inc}} = \frac{\pi}{2} g^2 \cos \theta_{\text{inc}} \left[1 - \frac{1 + \cos^2 \theta_{\text{inc}} + 2 \tan^2 \theta_{\text{inc}}}{2 k_1^2 g^2 \cos^2 \theta_{\text{inc}}} \right]. \quad (33)$$

3. Numerical Results

In this part, several numerical simulations are considered to demonstrate the algorithm's ability to deal with the scattering from the inhomogeneous target buried beneath a dielectric rough surface. The effectiveness of our proposed method is also illustrated. In all examples, the region 1 is considered as free space. In addition, all sizes are given in terms of free-space wavelength λ which is equal to 1 m in this paper unless otherwise specified. Finally, the relative permittivity of region 2 is $\varepsilon_{2r} = (2.0, -0.01)$.

Our numerical code is firstly applied to calculate the bistatic NRCS of a 3D PEC sphere buried under a Gaussian dielectric rough surface. The radius of the sphere is 0.5 m and the burial depth is 4.0 m. The incident angles are $\theta_{\text{inc}} = 0^\circ$ and $\varphi_{\text{inc}} = 0^\circ$. The length of the truncated rough surface is $L =$

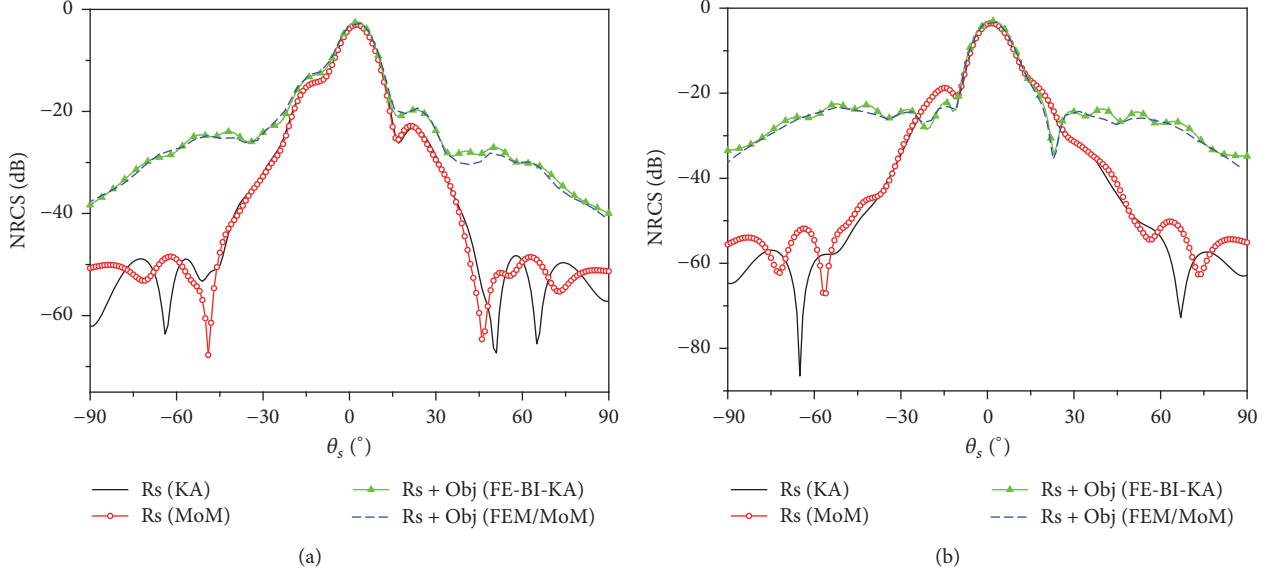


FIGURE 3: Bistatic NRCS of a 3D PEC sphere buried under dielectric rough surface: (a) X-Z Plane and (b) Y-Z Plane.

TABLE 1: Comparisons of the computing resource for different methods.

Method	Number of unknowns	Memory requirement (G)	Solving time (s)
FEM/MoM	83836	107.34	3807
New method	12186	1.43	127

Calculated by a computer with a 2.8 GHz processor (AMD Opteron™ Processor 4280), RAM 128 GB.

9.0 m. The tapering parameter of the tapered incident wave is $g = L/4$. The root-mean-square height and the correlation length of the rough surface are $\delta = 2.0$ m and $l_x = l_y = l = 0.1$ m, respectively.

Figures 3(a) and 3(b) show the bistatic NRCS as a function of scattering angle θ_s in X - Z and Y - Z planes, respectively. And the results are obtained with single rough surface sample. In the legends, “Rs + Object” denotes the model of an object buried under the rough surface. “Rs” denotes the model of the rough surface only. Figure 3 shows that the results obtained by our method agree with solutions of FEM/MoM very well. It can also be observed that the total NRCS is mainly contributed by the rough surface within the scattering angles $\theta_s \in (-15^\circ, 15^\circ)$, while in other scattering angles, the total NRCS is mainly contributed by the buried target.

Table 1 shows the comparisons of the computing resource for a single rough surface sample for different methods. The matrix of FEM/BIM is stored with compress sparse row format, and the parallel LU decomposition is used to solve the matrix equation. Table 1 indicates that the number of unknowns in our method is reduced to 14.5% of that in FEM/MoM, and the memory requirement and solving time are reduced to 1.3% and 3.3%, respectively. The result shows that our method is exact and efficient in dealing with the scattering from the target buried beneath rough surface.

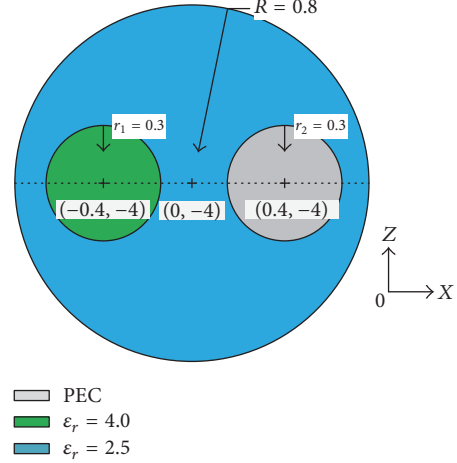


FIGURE 4: Cross-section of an inhomogeneous sphere.

To further demonstrate the ability of our method to deal with the composite scattering from the inhomogeneous target buried under rough surface, the scattering from a 3D inhomogeneous sphere buried under a dielectric rough surface, as shown in Figure 4, is calculated. The default parameters are set as follows: the incident angles are $\theta_{\text{inc}} = 15^\circ$ and $\varphi_{\text{inc}} = 0^\circ$, the truncated length of the rough surface is $L = 10.5$ m, and the root-mean-square height and the correlation length of the rough surface are $\delta = 1.5$ m and $l_x = l_y = l = 0.1$ m, respectively.

Figures 5(a) and 5(b) show the bistatic NRCS as a function of scattering angle θ_s in X-Z and Y-Z planes, respectively. And the results are obtained with single rough surface sample. It can be seen from Figure 5 that the results obtained by our hybrid method agree with solutions of FEM/MoM very

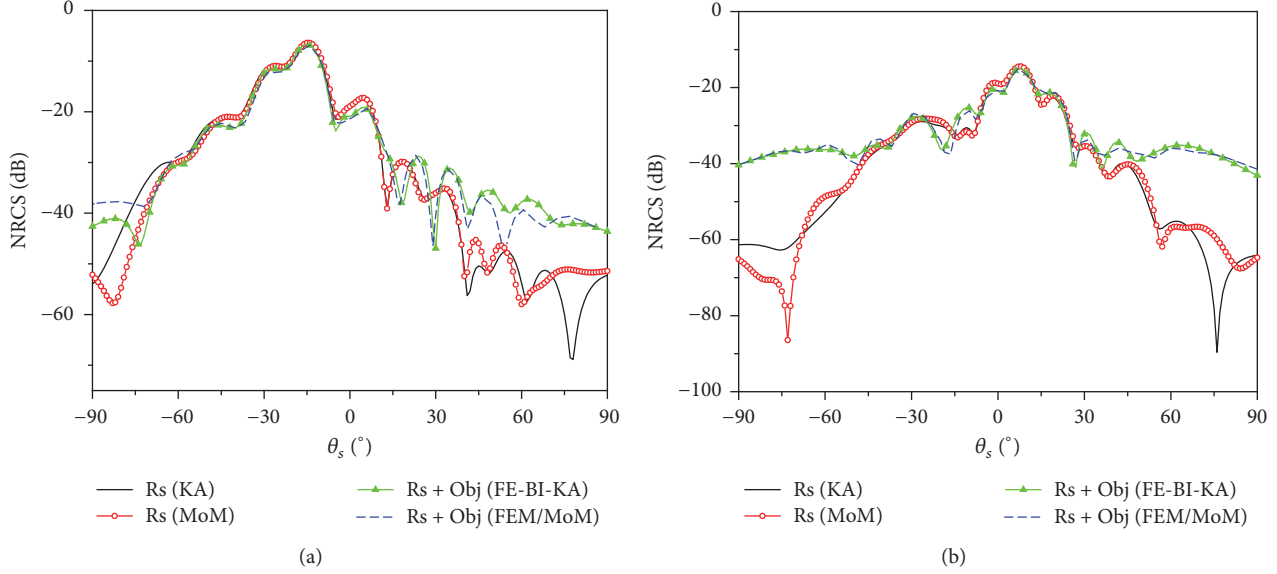
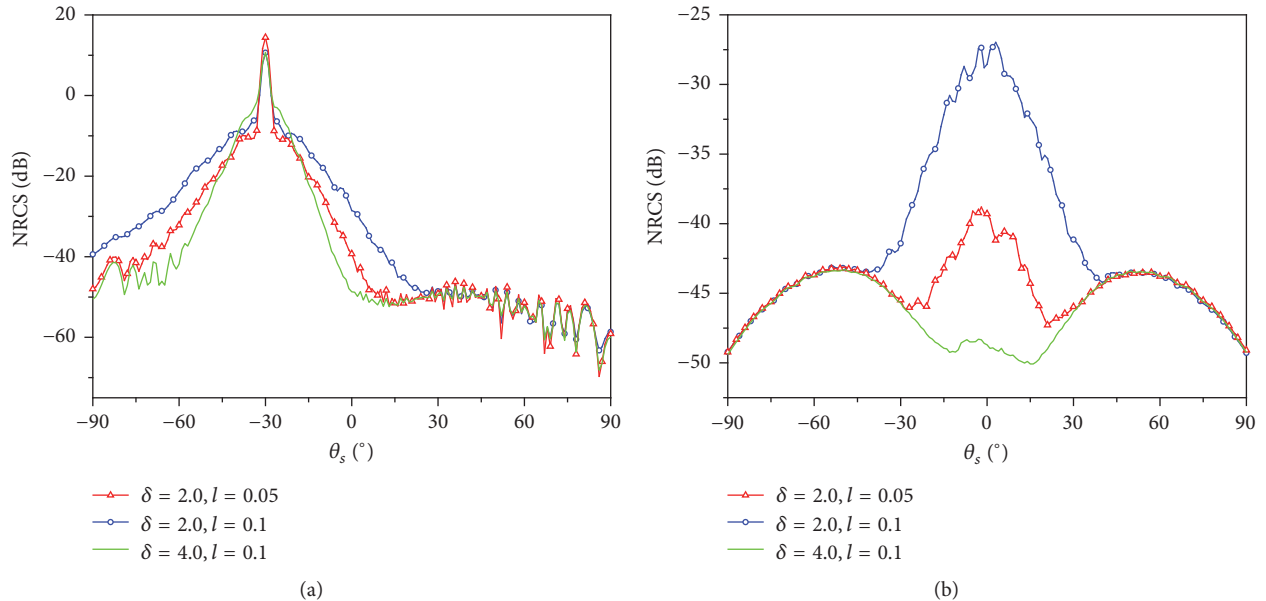


FIGURE 5: Bistatic NRCS of a 3D inhomogeneous sphere buried under dielectric rough surface: (a) X-Z Plane and (b) Y-Z Plane.

FIGURE 6: Scattering results of a 3D inhomogeneous sphere buried under dielectric rough surface with different δ and l : (a) X-Z Plane and (b) Y-Z Plane.

well, demonstrating the ability of our method to deal with the scattering from inhomogeneous target.

In the third example, the influence of the surface roughness on the scattering properties of the inhomogeneous sphere buried under dielectric rough surface is studied. The parameters of the inhomogeneous sphere are shown in Figure 4. The other parameters are set as follows: the length of the rough surface is $L = 50$ m, the incident angles are $\theta_{\text{inc}} = 30^\circ$ and $\varphi_{\text{inc}} = 0^\circ$. The parameters of the root-mean-square height δ and the correlation length $l_x = l_y = l$ of the rough surface can be found in the Figure 6.

The curves in Figure 6 present the influence of the surface roughness on the scattering properties of the inhomogeneous sphere buried under dielectric rough surface. The results are obtained by taking the average of 50 rough surface realizations. It can be seen from Figure 6(a) that the scattering coefficients have a small change with the change of the roughness in the scattering directions defined by $\theta_s \in [30^\circ, 90^\circ]$. Within the scattering angles $\theta_s \in [-90^\circ, 30^\circ]$, the scattering coefficient decreases in the specular direction with the increase in the root-mean-square height of the rough surface but increases in other scattering directions in the X-Z

Plane. In the Y - Z Plane, the NRCS increase evidently with the increase in the root-mean-square height of the rough surface in the scattering directions defined by $\theta_s \in [-45^\circ, 45^\circ]$. The increase in the correlation length weakens the NRCS in the scattering directions $\theta_s \in [-30^\circ, 30^\circ]$ in the Y - Z Plane.

4. Conclusions

In this paper, an efficient hybrid method has been presented to study the scattering from a 3D inhomogeneous object buried beneath a 2D dielectric rough surface. The electric and magnetic currents on the rough surface are analytically obtained by KA, which can greatly reduce the computing resource. The hybrid vector FEM/BIM, a powerful technique to model complex dielectric problem, is chosen to calculate the electric and magnetic currents on the inhomogeneous object. The matrix of FEM/BIM is stored with compress sparse row format, and the parallel LU decomposition is used to solve the matrix. The validity of our hybrid method is verified by numerical method. The effectiveness of our method is also illustrated. The results show that the memory requirement in our hybrid method is greatly reduced compared with the numerical method, and the computational time is also greatly reduced. The ability of our method to deal with the scattering inhomogeneous object buried beneath rough surface is also demonstrated.

Conflicts of Interest

The authors declare that they have no conflicts of interest.

Acknowledgments

This work was supported by the National Natural Science Foundation for Distinguished Young Scholars of China (Grant no. 61225002) and the Foundation for Innovative Research Groups of the National Natural Science Foundation of China (Grant no. 61621005).

References

- [1] W. Xande, G. Yow-Beng, and L. Le-Wei, "TE scattering from PEC object partially embedded at dielectric rough surface interface," in *Proceedings of The Fifth International Kharkov Symposium on Physics and Engineering of Microwaves, Millimeter, and Submillimeter Waves (IEEE Cat. No.04EX828)*, vol. 1, pp. 287–289, Kharkov, Ukraine, 2004.
- [2] A.-Q. Wang, L.-X. Guo, and C. Chai, "Application of a multi-region model to the em scattering from a rough surface with or without a target above it," *Chinese Physics B*, vol. 20, no. 5, Article ID 050201, 2011.
- [3] Y. Altuncu, "A numerical method for electromagnetic scattering by 3-D dielectric objects buried under 2-D Locally rough surfaces," *Institute of Electrical and Electronics Engineers. Transactions on Antennas and Propagation*, vol. 63, no. 8, pp. 3634–3643, 2015.
- [4] X.-C. Ren and L.-X. Guo, "Investigation on electromagnetic scattering from rough soil surface of layered medium using the small perturbation method," *Chinese Physics B*, vol. 17, no. 7, pp. 2491–2498, 2008.
- [5] M. A. Fiaz, F. Frezza, C. Ponti, and G. Schettini, "Electromagnetic scattering by a circular cylinder buried below a slightly rough Gaussian surface," *Journal of the Optical Society of America A: Optics and Image Science, and Vision*, vol. 31, no. 1, pp. 26–34, 2014.
- [6] D. E. Lawrence and K. Sarabandi, "Electromagnetic scattering from a dielectric cylinder buried beneath a slightly rough surface," *Institute of Electrical and Electronics Engineers. Transactions on Antennas and Propagation*, vol. 50, no. 10, pp. 1368–1376, 2002.
- [7] Y.-M. Zhang, Y.-H. Wang, and L.-X. Guo, "Study of scattering from time-varying Gerstners sea surface using second-order small slope approximation," *Chinese Physics B*, vol. 19, no. 5, pp. 0541031–0541039, 2010.
- [8] C. Bourlier, N. Pinel, and G. Kubické, "Propagation-inside-layer-expansion method combined with physical optics for scattering by coated cylinders, a rough layer, and an object below a rough surface," *Journal of the Optical Society of America A: Optics and Image Science, and Vision*, vol. 30, no. 9, pp. 1727–1737, 2013.
- [9] R.-W. Xu, L.-X. Guo, and R. Wang, "An iterative analytic - Numerical method for scattering from a target buried beneath a rough surface," *Chinese Physics B*, vol. 23, no. 11, Article ID 114101, 2014.
- [10] S. Bellez, C. Bourlier, and G. Kubické, "3-D scattering from a PEC target buried beneath a dielectric rough surface: an efficient PILE-ACA algorithm for solving a hybrid KA-EFIE formulation," *Institute of Electrical and Electronics Engineers. Transactions on Antennas and Propagation*, vol. 63, no. 11, pp. 5003–5014, 2015.
- [11] X. Millard and Q. H. Liu, "A fast volume integral equation solver for electromagnetic scattering from large inhomogeneous objects in planarly layered media," *Institute of Electrical and Electronics Engineers. Transactions on Antennas and Propagation*, vol. 51, no. 9, pp. 2393–2401, 2003.
- [12] Y. Ren, Q. H. Liu, and Y. P. Chen, "A hybrid FEM/MoM Method for 3-D electromagnetic scattering in layered medium," *Institute of Electrical and Electronics Engineers. Transactions on Antennas and Propagation*, vol. 64, no. 8, pp. 3487–3495, 2016.
- [13] R.-W. Xu, L.-X. Guo, H.-J. He, and W. Liu, "A Hybrid FEM/MoM Technique for 3-D Electromagnetic Scattering from a Dielectric Object above a Conductive Rough Surface," *IEEE Geoscience and Remote Sensing Letters*, vol. 13, no. 3, pp. 314–318, 2016.
- [14] H.-J. He and L.-X. Guo, "A Multihybrid FE-BI-KA Technique for 3-D Electromagnetic Scattering from a Coated Object above a Conductive Rough Surface," *IEEE Geoscience and Remote Sensing Letters*, vol. 13, no. 12, pp. 2009–2013, 2016.
- [15] H. Ye and Y.-Q. Jin, "Parameterization of the tapered incident wave for numerical simulation of electromagnetic scattering from rough surface," *IEEE Transactions on Antennas and Propagation*, vol. 53, no. 3, pp. 1234–1237, 2005.
- [16] J. M. Jin, *The Finite Element Method in Electromagnetics*, Wiley, New York, NY, USA, 1993.
- [17] L. Tsang, T. H. Kong, and K. H. Ding, *Scattering of Electromagnetic Waves: Numerical Simulations*, Wiley, New York, NY, USA, 2001.

Research Article

Modeling and Characterization of the Uplink and Downlink Exposure in Wireless Networks

Anis Krayni,^{1,2} Abdelhamid Hadjem,² Günter Vermeeren,³ Alain Sibille,¹ Christophe Roblin,¹ Wout Joseph,³ Luc Martens,³ and Joe Wiart¹

¹Telecom ParisTech, Paris, France

²Whist Lab Common Laboratory of Orange Labs and Institut Telecom, Paris, France

³Ghent University, Ghent, Belgium

Correspondence should be addressed to Anis Krayni; anis.krayni@gmail.com

Received 4 January 2017; Revised 14 April 2017; Accepted 3 May 2017; Published 11 June 2017

Academic Editor: Antonio Iodice

Copyright © 2017 Anis Krayni et al. This is an open access article distributed under the Creative Commons Attribution License, which permits unrestricted use, distribution, and reproduction in any medium, provided the original work is properly cited.

This paper deals with a new methodology to assess the exposure induced by both uplink and downlink of a cellular network using 3D electromagnetic simulations. It aims to analyze together the exposure induced by a personal device (uplink exposure) and that induced by a base station (downlink exposure). The study involved the major parameters contributing to variability and uncertainty in exposure assessment, such as the user's posture, the type of wireless device, and the propagation environment. Our approach is relying basically on the modeling of the power radiated by the personal device and the ambient electric field, while taking into account the effects of human body shadowing and the propagation channel fluctuations. The exposure assessment as well as the human-wave interactions has been simulated using the finite difference in time domain method (FDTD). In uplink scenarios, four FDTD simulations were performed with a child model, used in two postures (sitting and standing) and in two usage scenarios (voice and data), which aimed to examine the exposure induced by a mobile phone and a tablet emitting, respectively, at 900 MHz and 1940 MHz. In the downlink scenario, a series of FDTD simulations of an exposure to a single plane wave and multiplane waves have been conducted, and an efficient metamodeling of the exposure using the Polynomial Chaos approach has been developed.

1. Introduction

The rapid developments in wireless network technology have strengthened the presence of electromagnetic waves in our everyday lives. Hence, the exposure to near and far electromagnetic fields is becoming increasingly a matter of public concern. The exposure is determined by the SAR (*Specific Absorption Rate*) (W/Kg), which quantifies the power absorbed by human tissues from electromagnetic radiations. Several studies have been conducted to characterize, on one hand, the exposure induced by the base stations (downlink exposure) [1] and, on the other hand, that induced by wireless devices (uplink exposure) [2]. In most of these studies, both types of exposure were studied separately. However, in the context of wireless networks that are now so widely present in everyone's environment, a reliable characterization of exposure requires taking into account both uplink and

downlink radio waves. Basically, for a given duplex communication, these waves are not independent and involve a power management protocol [3]. The downlink radiation is mainly impacted by the propagation environment, particularly through the attenuation suffered by the signal wave before arriving at the receiver [4]. In the other side, other than the propagation environment, the uplink radiation is dependent on the user's activity, on the network (e.g., the rate and the QoS), and fundamentally on the performance of the device's antenna [5]. Actually, the wireless devices are often placed in the proximity of the user's body, which is a conducting system. Accordingly, a strong coupling effect takes place between the human tissues and the antenna [6]. These interactions can affect severely the antenna radiation properties, which are strongly involved in adjusting the uplink power [7]. The purpose of this paper is to discuss a numerical approach to characterize the variability associated

with both links radiations as well as the resulting exposure, using electromagnetic simulations and statistical analysis.

Compared to previous research [8, 9], this work involves the use of an anatomic child model under various postures, including standing and sitting position. Furthermore, it aims at introducing a methodology for characterizing the uplink power fluctuations as a function of shadowing effects caused by the human body and the multipath fading. In the downlink, this study deals with a metamodeling approach allowing prediction analytically of the exposure induced by a complex propagation environment.

In fact, a FDTD simulation incorporating a human body with a resolution of 1-2 mm is very expensive in time calculation and resources, which often impedes the study of a large number of exposure configurations. Our proposed method consists of extracting an input-output transfer function, linking the exposure induced by multiple plane waves to the parameters contributing in the variability of their total electric field, using a regression metamodel approach in the postprocessing of a finite subset of FDTD simulations.

This study is a part of an European project called LEXNET [10], supported by the European Commission under the FP7, was established to minimize the exposure induced by wireless systems. The rest of this paper is organized as follows. The second section presents the methodology used in the modeling of the uplink power and the electric field received from a fixed base station. The third section illustrates the materials used to prepare the simulations. Section 4 is reserved to discuss the results as well as the statistical analysis of the uplink exposure variability. Section 5 focuses on the investigation of the exposure to single and multiple plane waves. In this section, we discuss the use of Polynomial Chaos (PC) [11] approach in the metamodeling of the multipath exposure. In the last section, we apply the proposed results to realistic traffic measurements. A global conclusion is drawn in the end of the paper.

2. Exposure Assessment

In wireless systems, the total exposure induced by such a radio communication is given as the sum of the uplink exposure and the downlink exposure. Two quantities are often used to characterize such exposure: the local SAR and the global SAR. The first is defined as the power absorbed over a cube of 10 g, whose peak value is denoted by $\text{SAR}_{10\text{g}}^{\text{peak}}$. The second is the whole-body average SAR_{WB} , well known as the ratio of the absorbed power to the whole-body weight.

During a radio communication, the global induced exposure can be deduced from the following system of equations:

SAR:

$$\text{SAR}_{10\text{g}}^{\text{peak}} = \max \{\Lambda\},$$

$$\text{where } \Lambda = P_r \text{SAR}_{10\text{g}}^{\text{UL}*} + E_a^2 \text{SAR}_{10\text{g}}^{\text{DL}*}, \quad (1)$$

$$\text{SAR}_{\text{WB}} = P_{\text{in}} \text{SAR}_{\text{WB}}^{\text{UL}*} + E_a^2 \text{SAR}_{\text{WB}}^{\text{DL}*},$$

where $\text{SAR}_{10\text{g}}^{\text{UL}*}$ and $\text{SAR}_{\text{WB}}^{\text{UL}*}$ are, respectively, the $\text{SAR}_{10\text{g}}^{\text{peak}}$ and SAR_{WB} induced by a fixed uplink power of 1 W, respectively. $\text{SAR}_{10\text{g}}^{\text{DL}*}$ and $\text{SAR}_{\text{WB}}^{\text{DL}*}$ are, respectively, the $\text{SAR}_{10\text{g}}$ matrix and SAR_{WB} induced by an ambient electric field of 1 V/m, respectively. It should be mentioned that the $\text{SAR}_{10\text{g}}$ matrix is used to regroup all $\text{SAR}_{10\text{g}}$, those calculated over the whole body, in a 3D matrix whose dimensions are equal to the dimensions of the user's body [12, 13]. P_{in} (W) and E_a (V/m) represent the input power delivered to the personal device and the ambient electric field, respectively.

In both above relationships, the exposure level is calculated using the proportional relationship between the absorbed power and the electromagnetic radiation, which is considered as an unknown time-varying parameter.

2.1. Power Radiated by a Personal Device. This part is devoted to the modeling of the input power delivered to the personal device during an uplink communication. Obviously, this quantity depends on various parameters, including the antenna losses, the propagation channel (shadowing effects, multipath fluctuations), and the network's requirements in terms of the signal to-noise-ratio (SNR), especially when using a power management protocol [14]. Several studies have been performed to model the uplink power on a wireless network [15]. The vast majority of these studies were largely based on the use of statistical models for multipath channel to characterize the power fluctuations in different propagation scenarios. Among the famous models, we can mention the WINNER II project [16], which provides the main propagation characteristics of a set of specific environments, such as rural, urban, and semiurban regions. For each environment, it gives a prediction of the number of paths existing between any system "transmitter-receiver" as well as their amplitudes, phases, and arrivals and departures directions. In a typical multipath propagation channel, the P_{in} power should satisfy the following equation:

$$P_{\text{in}} \sum_{n=0}^{N_p} a_n^2(\tau_n) G_e(\phi_n, \theta_n) = \alpha, \quad (2)$$

where α is the power radiated by the personal device, which takes into account the user-induced losses and the fluctuations of the radio link. Otherwise, P_{in} is the antenna input power. This unknown quantity is given as the sum of the power absorbed by the users body and the useful power, which can be used to ensure the radio communication. The consideration of this basic relation is justified by the fact that the antenna is assumed well matched (without losses).

To focus only on the impact of the propagation environment and antenna performances, without taking into account the network requirements, the power α is kept constant and equal to 1 mW. G_e is the effective gain, which is the gain of the couple "user-antenna." This couple is considered invariant. In fact, the position of the device with respect to the user's body is assumed fixed during this study. N_p denotes the total number of paths, including the direct path Line-of-Sight (LOS) and non-line-of-sight (NLOS) path. Each path is parametrized by two angles: an azimuth angle ϕ_n and

an elevation angle θ_n . These angles are assumed to follow a discrete uniform distribution between 0° and 360° and a normal distribution with a mean of 0° and a standard deviation of 0° , respectively. The elevation 0° is associated with the horizontal plane.

To model the losses induced by the distance, we have intervened an attenuation coefficient a_n . This parameter is generated using an exponential function that depends on the delay spread $\tau_n(s)$.

$$a_n^2(\tau_n) \propto e^{-\tau_n/\sigma_s}, \quad (3)$$

where τ_n represents the time delay between transmission and reception of a signal. This time parameter is assumed to be uniformly distributed and increasingly arranged between 0 and τ_N . 0 is associated with the first path, which is often the LOS. σ_s is the root mean square (rms) delay spread.

Three propagation scenarios have been considered:

- (i) *Line-of-Sight scenario (LOS)*: a very typical propagation of a low probability of occurrence.
- (ii) *Non-Line-Of-Sight Scenario (NLOS)*: common scenario, such as indoor scenarios.
- (iii) *Combined LOS/NLOS*: common scenario (e.g., urban scenarios).

In the first case, we recall that the radio transmission can take place only under the LOS path, while in the second scenario we assume the existence of only indirect paths (NLOS) between the user and the base station. The last scenario assumes the existence of both types of paths together during the communication.

To separate mappings between these different scenarios, we note that the first component in (2), $a_0^2(\tau_0)G_e(\phi_0, \theta_0)$, is associated with the LOS path. In LOS environment, a_0 takes 1 by assuming a constant path loss normalized to be one.

In pure NLOS scenario, a_0 is chosen equal to 0, while in mixed LOS/NLOS scenario a_0 is subject to the Rice factor (K), which is given as follows:

$$K = \frac{a_0^2(\tau_0)}{\sum_{n=1}^{N_p} a_n^2(\tau_n)}. \quad (4)$$

All attenuation coefficients $a_{k \geq 0}$ are normalized so that the total sum is equal to one.

The main characteristics of each propagation scenario are illustrated in Table 1. A detailed explanation of the proposed methodology as well as considered assumptions is offered in [17].

2.2. The Ambient Electric Field. Turning to the downlink radiations, throughout this study we assume that the electric field emitted by the base station is considered as a uniform plane wave. Similarly to the uplink case, the ambient electric field can be composed of single or multiple plane waves arriving from random directions, with various propagation

TABLE 1: Propagation environment parameters.

	LOS	NLOS	LOS/NLOS
θ_n	Gaussian	N (0, 30)	N (0, 30)
ϕ_n	Uniform	U [0, 360]	U [0, 360]
K	Log-normal		LN (6, 7)
N_p	Gaussian		N (6, 3.5)
a_k	σ_s (ns)		N (10, 6)
		55	22

characteristics. Briefly, in a given location r , the total ambient field \vec{E}_a can be expressed as the following sum:

$$\vec{E}_a = \sum_{n=1}^{N_p} \vec{E}_n^{(V)}(\alpha_n, \phi_n, \theta_n) + \vec{E}_n^{(H)}(\alpha_n, \phi_n, \theta_n), \quad (5)$$

where N_p is the number of waves. $\vec{E}_n^{(V)}$ and $\vec{E}_n^{(H)}$ are, respectively, the vertical and horizontal polarized components of the n th incident plane wave. α_n , ϕ_n , and θ_n are the phase angle, the azimuth angle of arrival, and the elevation angle of arrival, respectively.

The first two angles are assumed to follow a uniform distribution between 0° and 360° , whereas the third angle (θ_n) is assumed to obey a normal distribution with a mean μ of 0° and a standard deviation σ of 20° .

Assuming that the original wave emitted from the base station is vertically polarized, the power received at this polarization can be described by a decreasing exponential function depending on the time parameter described above (τ_n, σ_s):

$$\|E_n^{(V)}\|^2 = \frac{P_0}{N_p} e^{-\tau_n/\sigma_s}, \quad (6)$$

where P_0 is the power associated with the original wave emitted from the base station. As a result of multiple scattering and reflection, the original signal can undergo modification of its polarization. Hence, the signal arriving at the receiver is mostly composed from vertically and horizontally polarized waves. The ratio of the power received in the vertical polarization to that received in the horizontal polarization is given by the cross polarization ratio XPR _{n} :

$$\text{XPR}_n = \left\| \frac{E_n^{(V)}}{E_n^{(H)}} \right\|^2. \quad (7)$$

This parameter is assumed to obey a log-normal distribution with a mean 0 and standard deviation 7 [18].

The squares of all vertical and horizontal polarized components are normalized to their total sum. We have always

$$\sum_{n=1}^{N_p} \|E_n^{(V)}\|^2 + \|E_n^{(H)}\|^2 = 1. \quad (8)$$

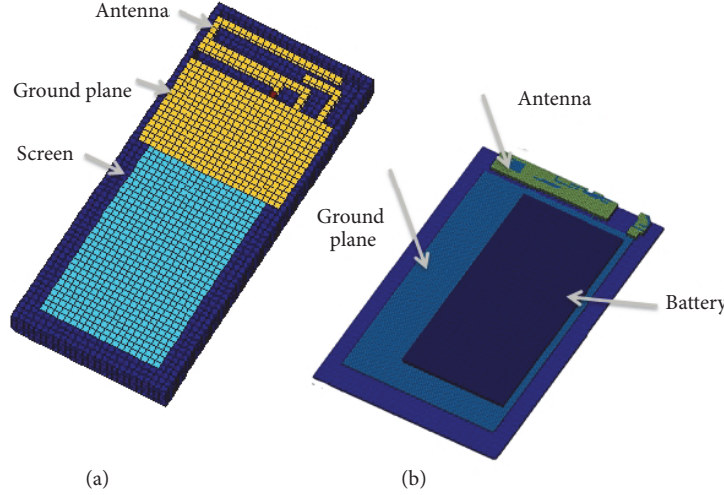


FIGURE 1: Wireless devices developed using MATLAB: (a) a mobile phone and (b) a tablet.

3. Materials

3.1. Realistic Human Phantom. To model the user body, we use an anatomically realistic human phantom *Earth*, an 8-year-old child selected from the Virtual Family [19]. This phantom is represented by a 3D heterogeneous matrix having 77 different labels, which are devoted to label the various child tissues. Using a deformation tool (EMPIRE Poser) [20], we made many elastic deformations on the standard model whose goal is to create realistic postures of the different wireless device usage, including mainly voice calling (in standing and sitting posture) and web browsing with a tablet (standing and sitting). All of these models are designed with a resolution of 2 mm. The dielectric properties of various tissues are assigned according to the data available in [21].

Concerning the radiation sources, we developed simplified numerical models for a mobile phone and a tablet operating at 900 MHz and 1940 MHz (see Figure 1).

Different antennas were then validated using FDTD simulations (in free space). As regards the reflection coefficient S_{11} , the obtained results can be considered acceptable. As presented in Figure 2, the S_{11} graph shows a significant resonance at the frequency of simulation, with a return loss below -10 dB with both antennas.

3.2. Exposure Simulations. We distinguish two types of FDTD simulations: simulations with personal devices and simulations with Huygens box. To study the exposure induced by a personnel device, the developed wireless devices are positioned close to the numerical phantom depending on usage scenario, as illustrated in Figure 3. Each uplink simulation starts with injecting an electric signal in the antenna to create an electric field near to the child phantom. Then, we integrate the iterative FDTD process to compute the electric field inside the child body. In the downlink simulation, we use the Huygens box excited by a plane wave [22].

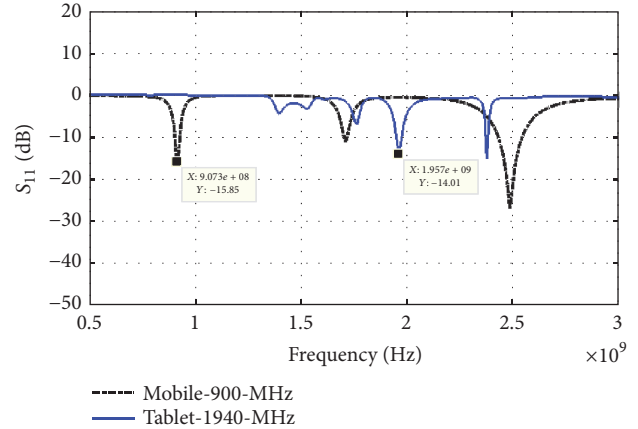


FIGURE 2: Reflection coefficient S_{11} obtained from FDTD simulations in “free space.”

4. Uplink Exposure: Results and Analysis

We begin by presenting the results obtained with the mobile phone at 900 MHz and the tablet at 1940 MHz. Table 2 gives values of the radiation efficiency, the power absorbed by the child’s body, the SAR_{WB} , and the $\text{SAR}_{10g}^{\text{peak}}$. All of these values are normalized to an input power of 1 W. The results show that almost 90% of the input power is absorbed by the child in either sitting or standing postures. Most of the power is absorbed by the head and the left hand (that holds the mobile phone).

In the case of the tablet, the power absorbed by the child was around 35% (standing) and 45% (sitting). Figure 4 shows the sagittal yz plane distribution of the power absorbed by the whole phantom. As shown, the level of the power absorbed reached its maximum peak in the location of the personal device.

Basically, in the case of an exposure to a personnel device, the exposure dose and especially the $\text{SAR}_{10g}^{\text{peak}}$ are very

TABLE 2: The absorbed power and the SAR_{WB} normalized to an input power of 1 W.

	Radiation efficiency (%)	Absorbed power (%)	SAR_{WB} $\text{W}\cdot\text{kg}^{-1}$	$\text{SAR}_{10\text{g}}^{\text{peak}}$ $\text{W}\cdot\text{kg}^{-1}$
Voice-standing	10	90	0.029	3.61
Voice-sitting	10	90	0.029	4.7
Tablet-standing	65	35	0.011	3.67
Tablet-sitting	65	35	0.014	4.44

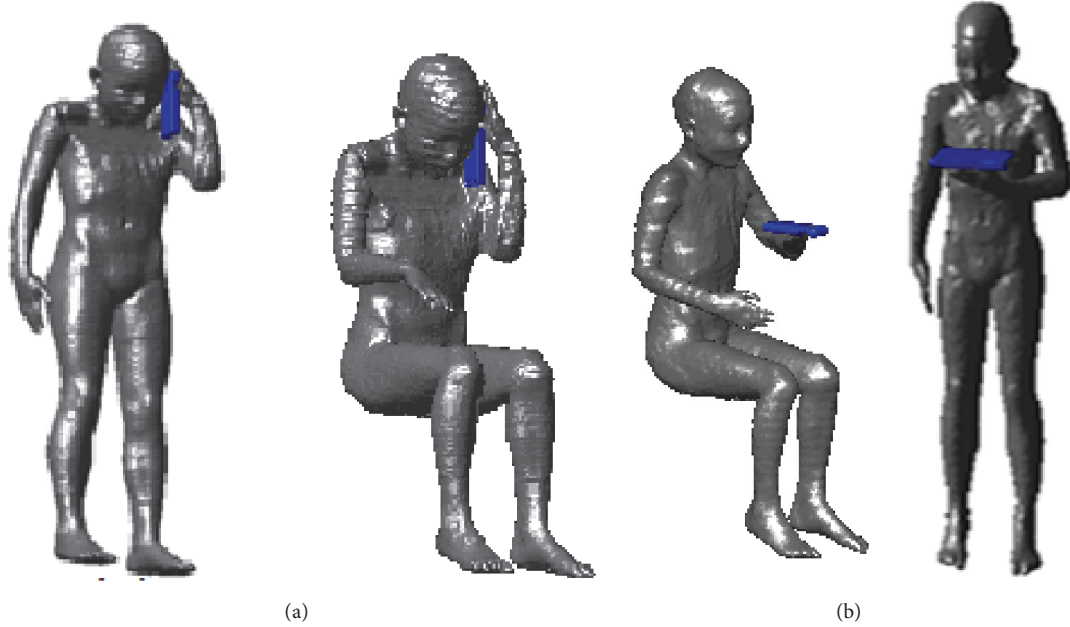


FIGURE 3: Different postures: (a) voice-standing and sitting and (b) data-standing and sitting.

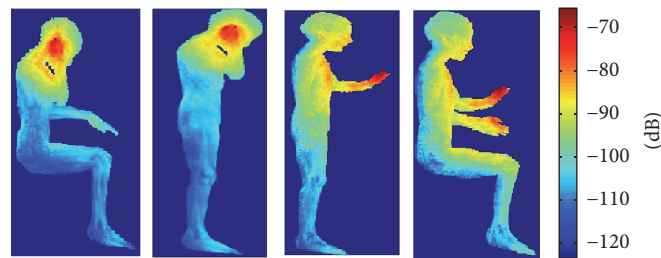


FIGURE 4: Distribution of the absorbed power (db) inside the numerical phantom for an input power of 1 W.

sensitive to the positioning of the antenna with respect to the user's body. For instance, a small change in the position of the mobile phone has led to a variation of 30% between both $\text{SAR}_{10\text{g}}^{\text{peak}}$ obtained with standing and sitting postures.

Turning to the converse effect, we noticed that the user's proximity caused a considerable degradation of the radiation pattern of the device's antenna. Figure 5 shows a comparison between the radiation pattern obtained with the mobile phone in the presence of the child (in a standing posture) and that calculated in free space. Briefly, we can see that a large part of the radiation pattern has been distorted by the left hand and the head, which caused the modification of the

directivity of the antenna (becomes more directional in the opposite direction of the head).

Given these effects, such a characterization of the antenna gain is considered an essential step in predicting the uplink power while relying on the power fluctuation model given in the Section 2.1. For full clarity, we again stress that the variation in T_x power stems from the power control, which is enforced by the base station according to its received power, sensitively determined by the radio channel.

A summary of the methodology is given in the diagram displayed in Figure 6. To sum up, this approach uses a FDTD simulation for characterizing the antenna's gain (in

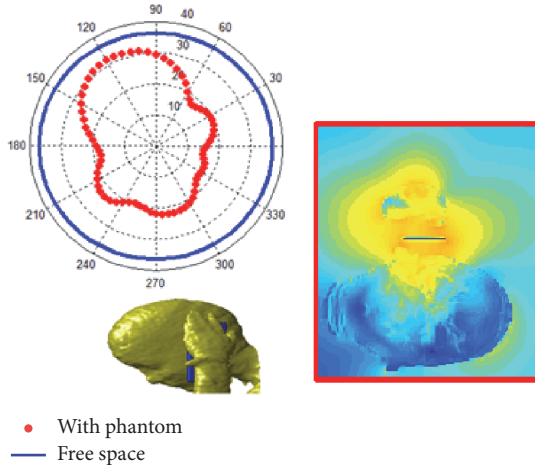


FIGURE 5: Effects of the head on the radiation pattern of the mobile phone at 900 MHz.

the presence of the user's body) as well as the induced exposure. The antenna gain obtained is then combined with a propagation model, whose aim is to analyze the variability of the input power.

To characterize the variability of the input power, a set of 10^4 values has been randomly generated for each propagation scenario (LOS, NLOS/LOS, and NLOS). With the different scenarios propagation, the statistical adjustment of obtained values showed that the distribution of the input power can be fitted by a log-normal distribution, whose parameters (mean and standard deviation) depend on the propagation scenario. Due to limited space, we illustrate a few results.

As an example of results, Figure 7 shows a comparison between the log-normal distribution and the empirical distribution of a set of 10^4 values of the input power obtained with the posture *voice-standing-900 MHz*, under a NLOS scenario.

As can be seen, the log-normal distribution suitably models the power fluctuations in this case. Similar results have been obtained with tablet at 1940 MHz. The log-normal distribution describes the shadowing/masking effects in propagation.

Turning to the exposure investigation, by relying on the proportional relationship between the input power and the induced exposure, Figures 8 and 9 illustrate the cumulative distribution functions (CDF) of the $\text{SAR}_{10g}^{\text{peak}}$, induced by the input power in the posture *voice-standing-900 MHz* and in the case of posture *data-standing-1940 MHz*, respectively.

With both postures, the $\text{SAR}_{10g}^{\text{peak}}$ is varied logarithmically over the ranges 0 and 1 W/kg.

A similar study was done for the SAR_{WB} . The parameters of obtained distributions are shown in Tables 2 and 3.

It is of practical interest to notice that, by setting α equal to 1 mW, virtually all $\text{SAR}_{10g}^{\text{peak}}$ and SAR_{WB} values induced by the mobile phone and the tablet are less than thresholds required by ICNIRP [23]: 2 W/kg for $\text{SAR}_{10g}^{\text{peak}}$ and 0.08 W/kg for SAR_{WB} .

TABLE 3: Characteristic of the distribution of exposure values at 900 MHz.

	μ (dB) $\mu_{\text{SAR}_{10g}}/\mu_{\text{SAR}_{\text{WB}}}$	σ	CV (%) $\text{CV}_{\text{SAR}_{10g}}/\text{CV}_{\text{SAR}_{\text{WB}}}$
NLOS	-3.18/-8.00	0.41	42/42
LOS+NLOS	-2.95/-7.77	0.77	92/92
Only LOS	-0.28/-5.10	0.92	112/112

TABLE 4: Characteristic of the distribution of exposure values at 1940 MHz.

	μ (dB) $\mu_{\text{SAR}_{10g}}/\mu_{\text{SAR}_{\text{WB}}}$	σ	CV (%) $\text{CV}_{\text{SAR}_{10g}}/\text{CV}_{\text{SAR}_{\text{WB}}}$
NLOS	-4.67/-10.67	0.32	36/36
LOS+NLOS	-4.45/-10.45	0.8	125/125
LOS	-4.32/-10.3251	1.03	178/178

To evaluate the impact of the propagation scenario on the variability of the input power, we focused on the assessment of the coefficient of variation (CV), given as the ratio of the standard deviation to the mean multiplied by 100%. As shown in Tables 3 and 4, this statistical indicator increases from one scenario to another in the following increasing order: NLOS, NLOS+NLOS, and LOS.

In a LOS scenario, the input power is strictly depending on the antenna gain in the LOS direction, which can vary as a function of the user's orientation with respect to the base station. In such scenario, the large fluctuations of the input power are explained by the nonuniformity of the antenna's gain.

In a pure NLOS scenario, the contribution of various paths, characterized by a significant diversity, reduces the impact of the radiation pattern nonuniformity. Briefly stated, a certain averaging of the antenna gain is established by the random combinations of NLOS path, which allows reducing accordingly the variability of the input power. In a LOS and NLOS mixture, this multipath adjustment remains valid, but it is limited by the Rice factor K . With a higher K value, the case is similar to a pure LOS scenario.

$\mu(\log(\cdot))$ and σ are the mean (dB) and the standard deviation, respectively.

5. Downlink Exposure: Simulations Results and Statistical Analysis

The downlink exposure is firstly investigated using a Huygens's box excited by a single plane arriving from different directions. In fact, the first simulations are devoted to assess the exposure induced by the LOS scenario, by assuming that most of the power emitted by the base station arrived from a single dominant direction.

In such case, for a given user's posture, three parameters have been considered: the direction of arrival (both azimuth and elevation angles), the polarization, and the amplitude.

Due to the resource constraints and computing time limitations, a spatial discretization of the arrival directions

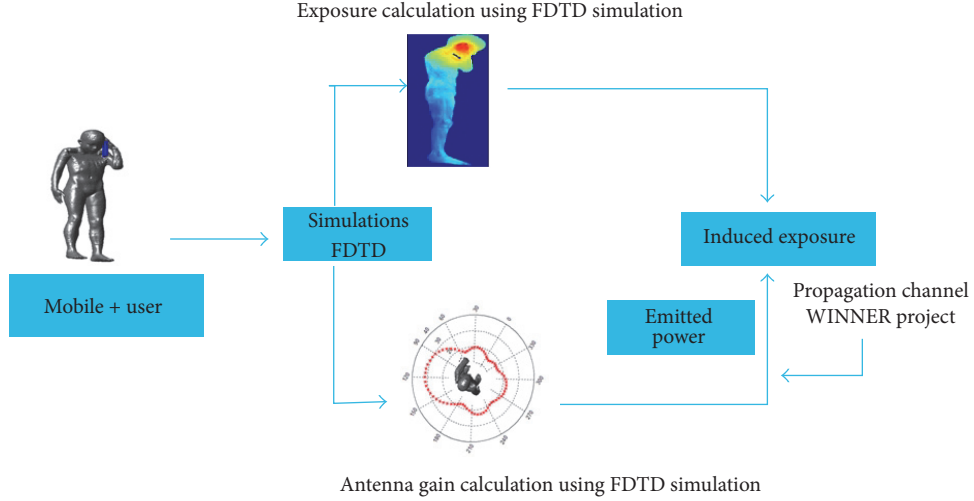


FIGURE 6: Flowchart of the subroutine for the characterization of the uplink exposure.

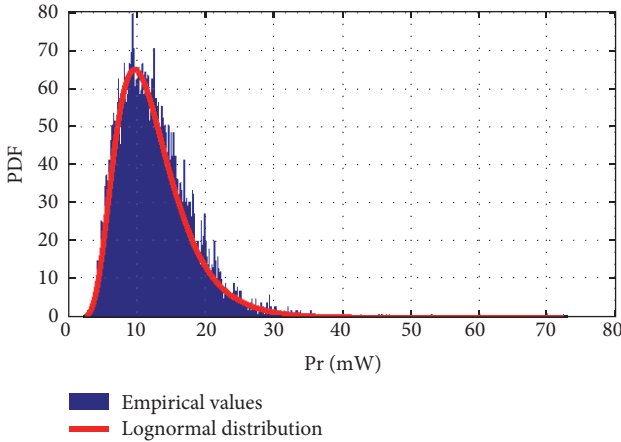
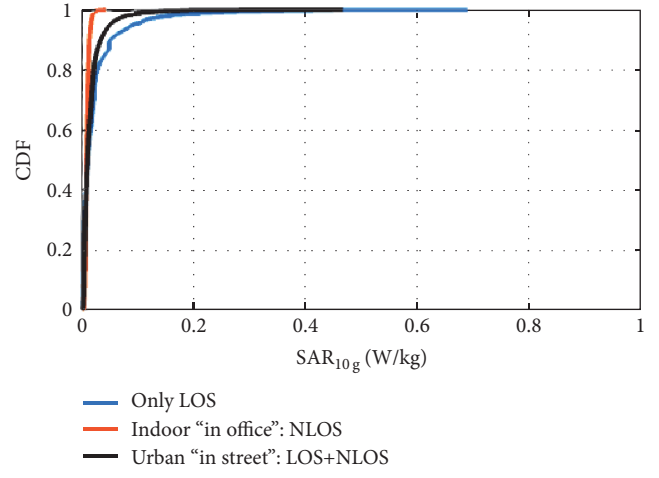
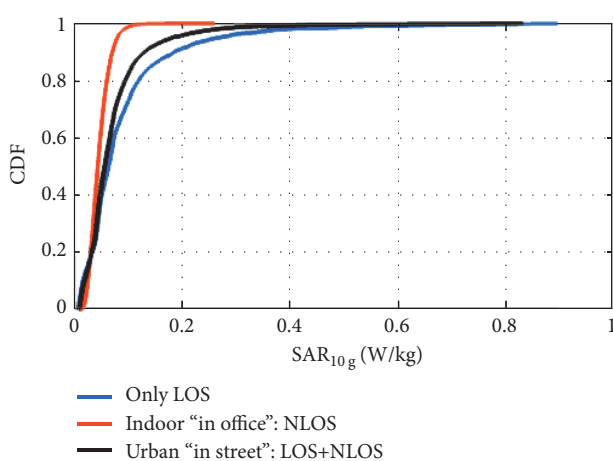


FIGURE 7: Comparison between empirical distribution of the input power delivered to the mobile phone during pure NLOS scenario and a log-normal distribution.

FIGURE 9: SAR_{10g} induced by the tablet at 1940 MHz.FIGURE 8: SAR_{10g} induced by the mobile phone at 900 MHz.

was refined, so as to reduce the number of simulations. Therefore, the azimuth angle ϕ has been discretized into 12 angles, uniformly spaced with a gap of 30 and the elevation angle θ ranged from -20 to 110 with a step width of 20 (3 angles). Both vertical (V) and horizontal (H) polarization have been considered during each configuration, which increased the number of simulations to 72 for each posture. All parameters used in simulations are illustrated in Figure 10.

Figures 11 and 12 illustrate, respectively, the variation of SAR_{WB} as a function of the elevation angle, azimuth angle, and the polarization for the postures *voice-standing-900 MHz* and *data-standing-1940 MHz*. These results are obtained with an electric field of 1 V/m. In these figures, we can see that SAR_{WB} is very sensitive to the azimuth angle ϕ . Various curves of SAR_{WB} show some sinusoidal behavior. As was mentioned in the research of Conil et al. [24], the power absorbed by the user's body is proportional to the exposed

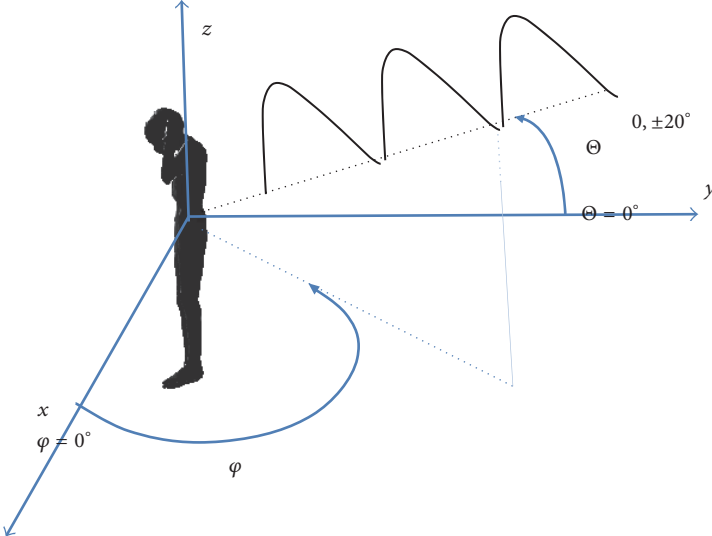


FIGURE 10: Definition of the parameters involved in the study of the exposure to a single plane wave.

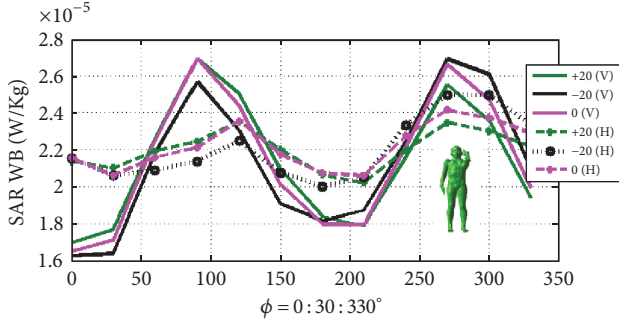


FIGURE 11: Variation of SAR_{WB} obtained with the posture *voice-standing-900 MHz* after an exposure to a plane wave coming from three elevations, from azimuth from 0 to 360 and in both V-polarization and H-polarization.

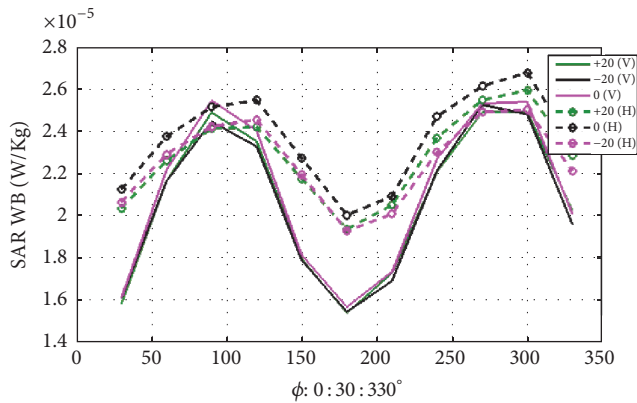


FIGURE 12: Variation of SAR_{WB} obtained with the posture *data-standing-1940 MHz* after an exposure to a plane wave coming from three elevations, from azimuth from 0 to 360 and in both V-polarization and H-polarization.

surface, at least for the frequencies here considered. This explains the origin of two peaks obtained at $\phi = 270$ (frontal wave) and $\phi = 90$ (back wave).

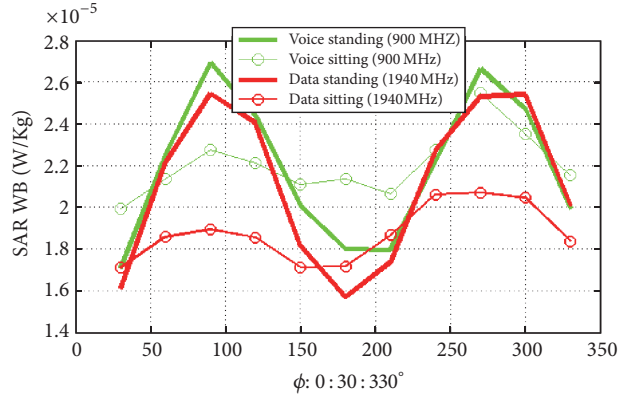


FIGURE 13: Comparison between the SAR_{WB} induced in voice and data configurations (standing and sitting postures) at 900 MHz and 1940 MHz, respectively. Results obtained after an exposure to plane wave vertically polarized at zero elevation.

The SAR_{WB} also varies from one posture to another, which is basically due to the effective exposed surface of the body to the incoming wave. Figure 13 deals with a simple comparison between four specific postures: voice at (standing/sitting) and data (standing and sitting). The results show that, depending on the azimuth angle, the exposure obtained with a standing posture is almost always higher than that induced in a sitting posture. In fact, the SAR_{WB} obtained with a sitting posture exceeds that induced in a standing posture only when the plane wave is coming from the left side of the phantom. This can be explained by the fact that a large part of the power is absorbed by the arms and the legs.

As regards the impact of polarization, for the frequency 900 MHz, the SAR_{WB} induced by a plane wave vertically polarized (VP) is higher than that induced by horizontally polarized (HP) in the case of a back/frontal plane wave. Figure 14 illustrates the distribution of the power absorbed inside the child's body after an exposure to a frontal wave at

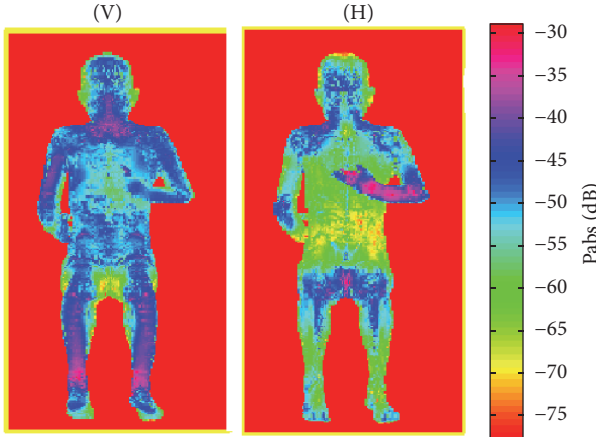


FIGURE 14: Distribution of the absorbed power inside the phantom after an exposure to a vertical/horizontal plane waves of 1V/m.

900 MHz with both vertical and horizontal polarization. The exposure induced by HP becomes higher than that caused by VP on the side of phantom.

According to results given in [25, 26], this tendency must be true only with the frequencies below 1 GHz [25, 26].

In fact, for the frequency 900 MHz, the wavelengths (0.33 m) are, respectively, equal to the user's width and 1/4 of its height. Hence, the user's body acts as a receiving antenna that favors wave absorption in both vertical and horizontal polarization. This is valid in, so far as the frequency is lower than 1 GHz, that when increasing the frequency, the exposure induced by horizontally polarized waves becomes higher than that induced by vertically polarized waves.

More clearly, for higher frequencies, the user's height begins larger than the wavelength (8 times higher at 1940 MHz), while the user's width remains relatively close to this value (twice higher at 1940 MHz). Consequently, the user's body becomes more sensitive to horizontally polarized waves. As shown in Figure 12, the SAR_{WB} obtained at 1940 MHz with horizontal polarization is higher than that obtained with vertical polarization.

Regarding the local exposure, we noticed that the SAR_{10 g}^{peak} is sensitive to the dielectric properties of the tissues as well as the emitting frequency. However, the variation of SAR_{10 g}^{peak} depending on the azimuth arrival angle does not exhibit a remarkable visual behavior.

Consequently, the efforts were concentrated only to identify the location of the peak value.

In this context, Figure 15 deals with the locations of various peaks in the postures *voice-standing-900 MHz*, *voice-sitting-900 MHz*, and *data-sitting-1940 MHz*. With both voice postures, the maximum is reached at the arms and feet, while with the *data-sitting-1940 MHz* the peak is located at the arms and the head. In fact, the exposure peaks depend basically on tissue types as well as the electromagnetic resonance. Particularly, at 900 MHz, this resonance occurs close to the ground. This may explain the presence of several peaks of exposure at the feet.

The motivation behind the peak identification is to predict if some accumulation of the local exposure in a given position can be expected, especially when the phantom is exposed to the plane wave and the wireless device together. Simultaneous uplink/downlink exposure is highly frequent in the context of wireless networks. In fact, it is important to anticipate if the peak induced by a multiple-exposure can be higher than that induced by each path separately. A graphic illustration of all local maximum allows evoking the possibility of accumulation of both peaks associated with both links in the same location. In such case, the local exposure may exceed the limit imposed by the ICNIRP. However, Figure 15 confirms that the probability of such superposition is always negligible.

5.1. Metamodeling Approach for Exposure Assessment. The single-wave exposure remains a singular case that does not reflect all of reality, which is often characterized by various multipath configurations. For that reason, we address in this section the exposure resulting from multiple plane waves having random propagation characteristics. In such scenario, the exposure assessment could be much costly in computation time and resources than that conducted with personal devices. In fact, contrary to the uplink case, where we were only interested in modeling the variability of the input power during the postprocessing of FDTD simulations, the evaluation of the downlink exposure requires performing a large number of simulations to examine all possible multipaths configurations. Even if a suitable discretization of the spatial domain can largely reduce the number of simulations [27, 28], this technical approach cannot be applied to some propagation scenarios, particularly in the presence of diffuse scattering components. Therefore, the numerical calculation process requires a very fine angular grid of arrival angles, which can increase dramatically the number of FDTD simulations.

To cope with this constraint, we propose to use a statistical approach through an input-output metamodel allowing approximating analytically the SAR_{WB} induced by a given propagation scenario. The determination of this transfer function requires firstly performing an initial set of FDTD simulations, whose input parameters are generated using various probability distributions.

The obtained results are then used to extract an input-output function allowing to characterize all interactions suffered by input parameters as well as their relationship with the output quantity (SAR_{WB}).

We rely on classical regression techniques to compute this transfer function which will be exploited to predict analytically the SAR_{WB}.

Among the most popular methods used in such problems, we mention the Polynomial Chaos (PC) expansion, well known for its simplicity and efficiency.

In essence, this method involves determining the transfer function by expanding it over an orthogonal polynomial basis, such as the Legendre polynomials.

Its principle consists in determining a transfer function between the output (SAR_{WB}) of the FDTD simulations and all

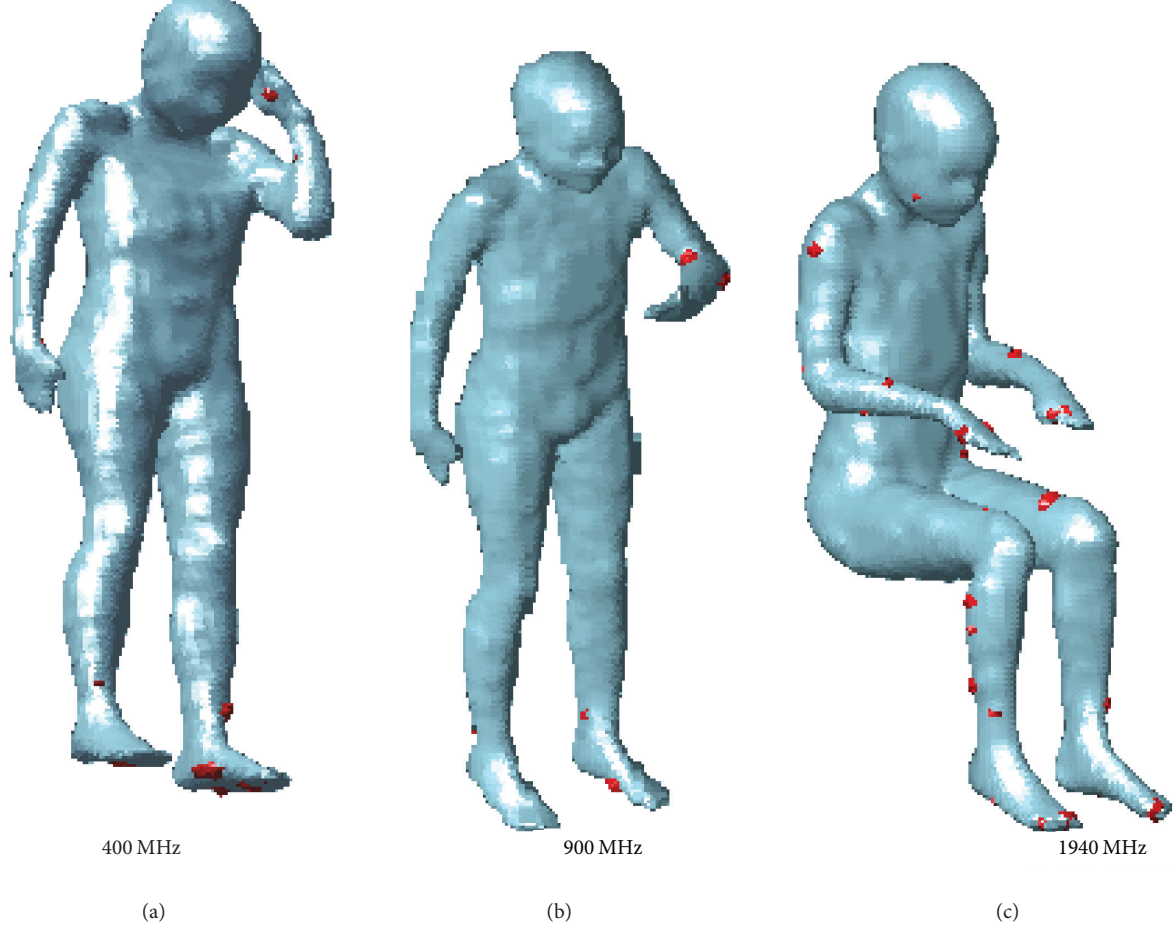


FIGURE 15: Identification of SAR_{10 g} peak locations. (a) *Voice-standing-900 MHz*, (b) *voice-sitting-900 MHz*, and (c) *data-sitting-1940 MHz*.

input parameters by expansion in an orthogonal polynomial basis, such as the Legendre polynomials.

Derived from this algebra approach, the obtained SAR_{WB} should be written as

$$\text{SAR}_{\text{WB}}^{\text{PC}} = \sum_{k=1}^M \beta_k \Psi_k(X), \quad (9)$$

where $\beta = \{\beta_1, \dots, \beta_M\}$ are unknown determinist coefficients and $\Psi(\cdot)$ are the multivariate orthogonal polynomials, which are chosen to be the Legendre polynomials. $X = \{X_1, \dots, X_N\}$ is the input vector that regroups all parameters involved in the formulation of the ambient electric field (see (5)), including the amplitude E_n , the azimuth angle ϕ_n , the elevation angle θ_n , the phase α_n , and the cross polarization ratio XPR_n.

For ensuring a good spatial coverage of the experimental region with a finite number of samples, we relied on the Latin hypercube sampling (LHS) [29] to generate all parameters values. The various values provided by LHS are probabilities $p_{X_{i,i \in [1,N]}}$ that range from zero to one. Hence, to use these probability values in FDTD simulations, we need to calculate the realization associated with each probability using the

inverse cumulative distribution function (ICDF) related to each propagation parameter.

In order to achieve the interorthogonality of the polynomials, especially when using the Legendre polynomials, it is necessary to translate the probabilities given by LHS into new variables varying between -1 and $+1$. To ensure this constraint, we apply the linear transformation that associates a probability p_{X_i} with the value $2p_{X_i} - 1$.

It is clear that the key step in this approach is the determination of weighting coefficients β_i . To do this, we use the regression approach to estimate the coefficients that minimize the Mean Squared Distance (MSD) between the analytic approximation SAR_{WB}^{PC} and the empirical value SAR_{WB}^{FDTD} .

$$\{\beta_{i,i \in [1,M]}\} = \arg \min \{A\}, \quad (10)$$

where

$$A = \left\{ \sum_{j=1}^{N_{\text{sim}}} \left\| \text{SAR}_{\text{WB}}^{\text{FDTD}}(X^{(j)}) - \text{SAR}_{\text{WB}}^{\text{PC}}(X^{(j)}) \right\|^2 \right\}, \quad (11)$$

where N_{sim} and $X^{(j)}$ are, respectively, the total number of simulations and the input vector used in the j th simulation.

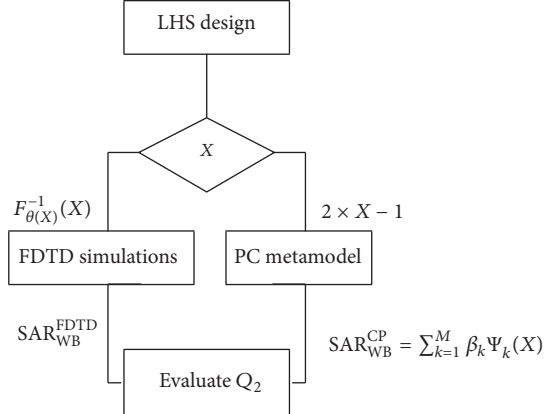


FIGURE 16: Flowchart of the proposed approach.

To judge the fidelity and the performance of the final metamodel, we conducted a certain number of validation tests by relying on the leave-one-out (LOO) approach [30]. This technique consists of removing one simulation from the total number of simulations and approximating a new surrogate model using only $N_{\text{sim}} - 1$ simulations. The novel surrogate model should be used then to reestimate analytically the output of the removed simulation as well as the induced error with respect to the empirical result (given by the FDTD computation).

The average error ϵ is given as follows:

$$\epsilon = \frac{1}{N_{\text{sim}}} \sum_{j=1}^{N_{\text{sim}}} \| \text{SAR}_{\text{WB}}^{\text{FDTD}}(X^{(j)}) - \text{SAR}_{\text{WB}}^{\text{PC},j}(X^{(j)}) \|^2, \quad (12)$$

where $\text{SAR}_{\text{WB}}^{\text{PC},j}$ is the analytic model, obtained without considering the j th simulation. In what follows, we use the error coefficient Q^2 as a quality criterion, which is calculated as follows:

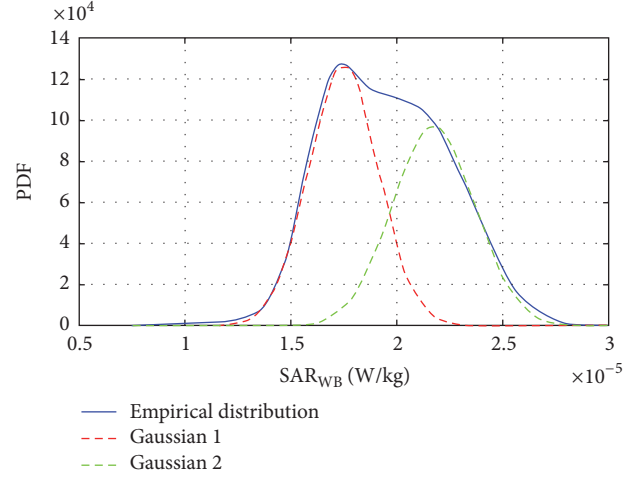
$$Q^2 = 1 - \frac{\epsilon}{E\{\|\text{SAR}_{\text{WB}}^{\text{FDTD}}\|\}}. \quad (13)$$

A coefficient Q^2 of 1 indicates a perfect metamodeling. Figure 16 shows a flowchart illustrating the process of the exposure metamodeling.

To simplify the notation, the input vector \mathbf{X} is arranged in the following order:

- (i) $X_{1,j}$ is the amplitude $\|E_n^{(\text{V})}\|$.
- (ii) $X_{2,j}$ is the azimuth ϕ_n .
- (iii) $X_{3,j}$ is the elevation θ_n .
- (iv) $X_{4,j}$ is the phase α_n .
- (v) $X_{5,j}$ is the cross polarization XPR_n .

It should be noted that the number of input parameters (size of \mathbf{X}) is some multiple N_p (number of plane waves). To ensure a fast convergence of the regression algorithm, with a reasonable number of simulations, N_p is assumed to be 5, which remains a very reasonable choice [31].

FIGURE 17: Fit of the SAR_{WB} distribution with a Gaussian mixture.

Due to a limited time budget, we are interested only in the exposure induced in both models *voice-standing-900 MHz* and *data-standing-1940 MHz*.

A set of 1000 FDTD simulations are performed with each model whose obtained results are discussed below.

Beginning with the *voice-standing-900 MHz*, Figure 17 shows the SAR_{WB} distribution obtained from 1000 simulations. The drawn distribution resembles a Gaussian mixture (GM), which represents two significant “shoulders.” On the other hand, the distribution width is too narrow, with a coefficient of variation of 14%. Unlike the results obtained with a single plane wave, the SAR_{WB} converged to an “average configuration” having poor sensitivity to the arrival directions of the electromagnetic waves. We also found that the exposure induced by 5 waves is often lower than that induced by a single frontal plane wave (considered as a worst case), when considering the same incident electric field (1 V/m). The number of cases where the exposure exceeds the classical worst case is less than 5% (see the colored region in Figure 18).

Turning to the metamodeling process, Figure 18 presents a graphical comparison between the empirical distribution SAR_{WB} and that generated by the analytic metamodel when using the same input vector \mathbf{X} .

As regards the metamodeling fidelity, it was needed to increase the degree and the number of Legendre polynomials up 15 to obtain a Q_2 of 0.86. This can be explained by the higher-order interactions existing between various input parameters.

The final step in the exposure metamodeling process is the prediction of the SAR_{WB} for other multiple-waves realizations having similar propagation characteristics.

Figure 19 illustrates the distribution obtained from 10^5 random configurations. The resulting distribution does not display two bumps (shown previously), but it gets close to a Gaussian distribution with a mean of 2.10^{-5} (W/kg) and a standard deviation of 15%. It should be noted, however, that the mean and standard deviation of this distribution are similar to the results obtained with the empirical distribution.

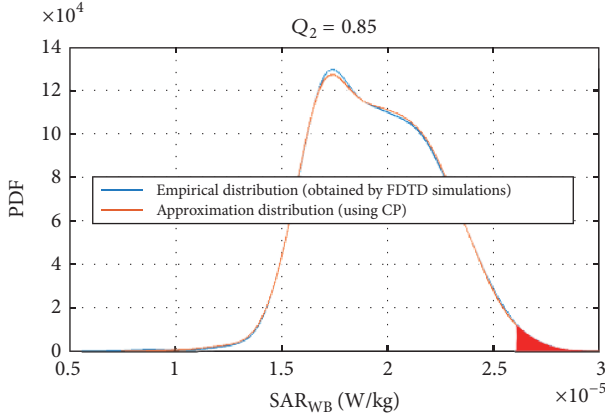


FIGURE 18: Comparison between the approximate and the empirical distribution.

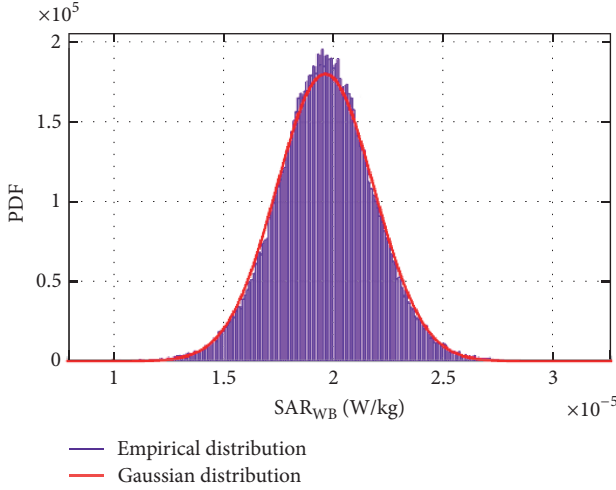


FIGURE 19: Distribution of the SAR_{WB} induced by 10^5 realizations.

This confirms the fact that the considered number of simulations, even if it makes to predict the “skeleton” of the transfer function (with a certain level of fidelity), remains insufficient to illustrate the final distribution as well as all interactions between 25 input parameters.

Similar results have been obtained with the *data-standing-1940 MHz* posture. An exposure metamodel derived from 1000 simulations is used to generate the SAR_{WB} induced by 10^5 random realizations. The obtained CDF is shown together with that calculated with *data-standing-900 MHz* in Figure 20.

Similar results are obtained with the posture *data-standing-1940 MHz*. An approximated metamodel of the exposure induced by random propagation scenarios was designed from 1000 FDTD simulations. This model was used to generate the SAR_{WB} induced by 10^5 different configurations. The obtained CDF is shown together with that calculated with *voice-standing-900 MHz* in Figure 20.

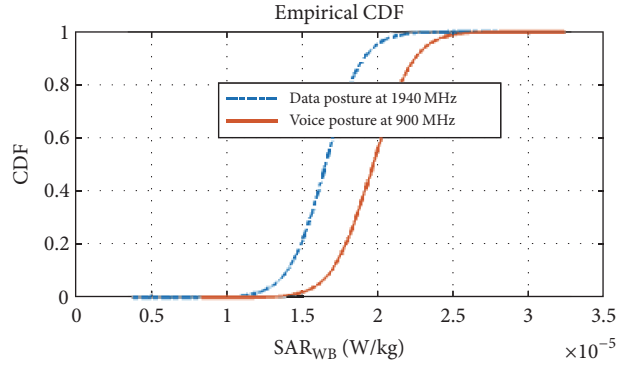


FIGURE 20: CDFs of the SAR_{WB} obtained at 900 MHz and 1940 MHz.

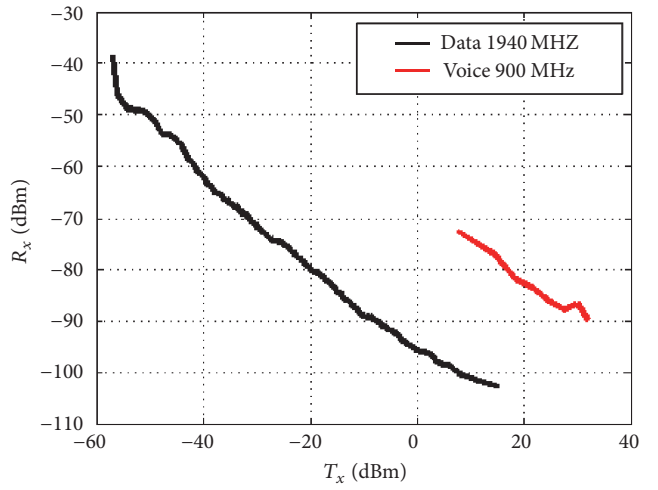


FIGURE 21: Variation of R_x power as a function of T_x power for 2G (900 MHz) and 3G systems (1940 MHz).

6. Statistical Modeling of a Realistic Exposure Scenario

This section is devoted to applying the methodologies presented as well as the obtained results to a real network. For this reason, various measurements of the uplink power T_x (the power emitted by the user system) and the downlink power R_x (the power received at the user system) are performed inside the Lyon city (France) and its surroundings cities, including basically NLOS scenarios. We note that the user system is the couple composed by the human body and the personal device. For emissions at 900 MHz, a hand-held probe connected to various base stations is configured to measure the radio traffic in both uplink and downlink paths. Concerning the tarfics at 1940 MHz, the data are taken from a measuring campaign conducted using two mobile phone trackers. A detailed description of measurement campaigns and an analysis of obtained results are given in [32].

As an example of results, Figure 21 illustrates the variation of the R_x power as a function of the T_x power. We can clearly see that the uplink power varies inversely as the downlink power, which can be explained by the use of advanced power management techniques in both GSM and 3G technologies.

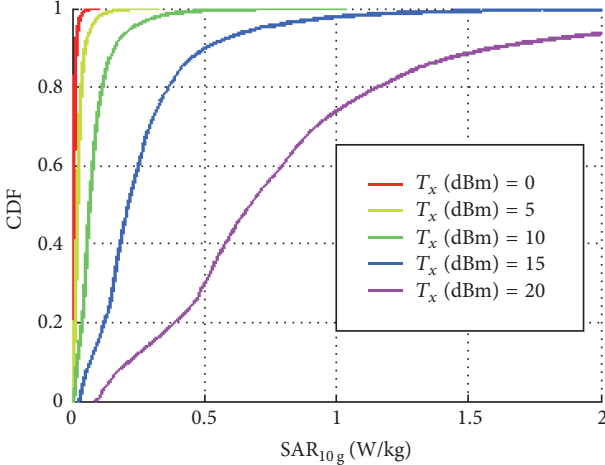


FIGURE 22: CDFs of SAR_{10g}^{peak} induced by the mobile phone at 900 MHz for various values of T_x .

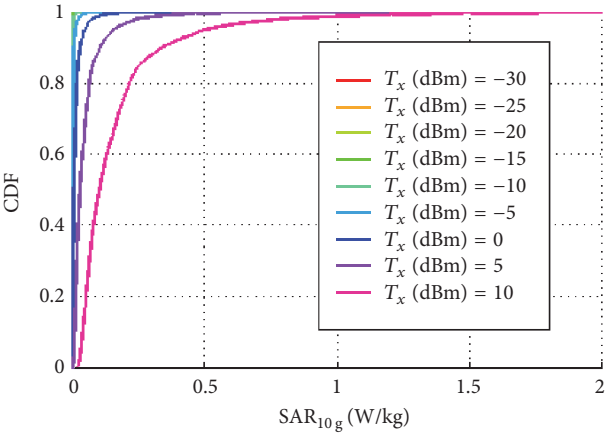


FIGURE 23: CDFs of SAR_{10g}^{peak} induced by the tablet at 1940 MHz for various values of T_x .

We recall that all T_x/R_x values are harvested in the presence of the user's body, whether using a trace mobile or a probe connected to the network. In both cases, the measured power remains uncertain, which depends largely on the losses induced by the users body. Otherwise, the T_x power can be considered as the given parameter α in (2) (Section 2). Hence, the exposure induced by varying T_x values is not constant, but it follows a log-normal distribution, according to the fluctuations of the input power delivered to the mobile phone tracker. Therefore, the uplink exposure characterization process consists in extracting the exposure CDF for each T_x power.

In what follows, we limit ourselves to the case of a pure NLOS scenario. As an example, Figures 22 and 23 show, respectively, the CDFs of the SAR_{10g}^{peak} induced at 900 MHz and 1940 MHz. We note that the SAR_{10g}^{peak} is generally lower than 2 W/kg. In fact, in the case of the mobile phone, the time-averaged input power must not exceed 250 mW (for technical considerations). Consequently, the maximum of the resulting

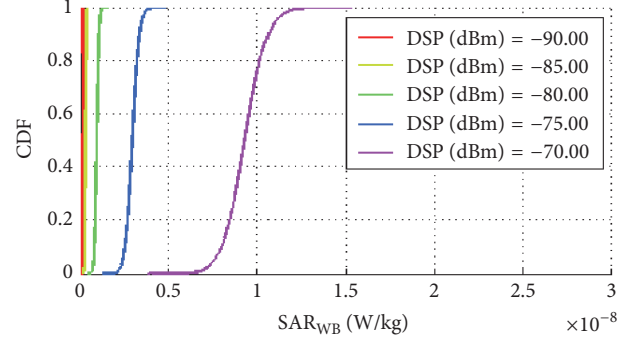


FIGURE 24: CDFs of SAR_{WB} induced by the downlink (5 plane waves) at 900 MHz for various values of DSP.

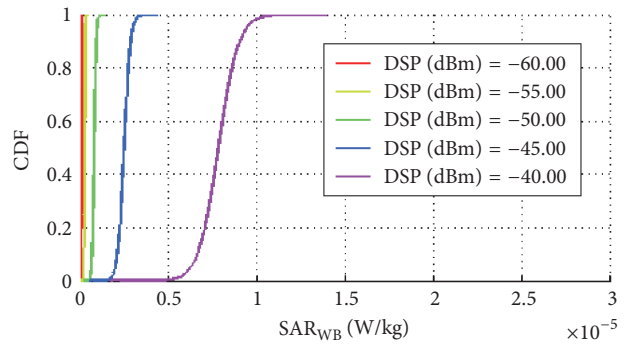


FIGURE 25: CDFs of SAR_{WB} induced by the downlink (5 plane waves) at 1940 MHz for various values of DSP.

SAR_{10g}^{peak} remains below 0.9 W/kg. Similar results are obtained for the SAR_{WB}.

Turning to the downlink case, we draw attention to the fact that the power density DSP (W/m²) and the square of the ambient electric field E_a^2 can be calculated from the received power R_x using the following mathematical relations:

$$\text{DSP} = \frac{1}{C_i} 10^{(R_x-30)/10}, \quad (14)$$

$$E_a^2 = \frac{377}{C_i} 10^{(R_x-30)/10},$$

where C_i is the aperture of a lossless isotropic antenna, which is equal to $\lambda^2/4\pi$. In fact, we consider here that the received system (the user's body + device) is a perfectly matched isotropic antenna, without considering the gain of the personal device. The objective of such hypothesis is to simplify the assessment of the downlink exposure (far-field) without taking into account the mobile phone mode (active/sleep). The evaluation of this quantity consists in using the analytic metamodel associated with the multiwave exposure (Section 5). Indeed, the electric field received is assumed to be a superposition of 5 plane waves. The rest of the downlink exposure characterization process consists in deducing the SAR_{WB} CDF using the proportional relationship between the exposure dose and the electric field.

As a preliminary result, Figures 24 and 25 illustrate the CDFs of the SAR_{WB} obtained from various values of DSP

for each of the following scenarios: voice at 900 MHz and data at 1940 MHz. Both figures indicate that the SAR_{WB} is not significant, whose majority of values are less than 10^{-8} W/kg (900 MHz) and 10^{-5} W/kg (1940 MHz).

The last part of this paper deals with the assessment of the total exposure which is given as the sum of both the uplink and downlink exposure (system of (1)). Due to the fact that the variation coefficient of the exposure is insignificant in the case of NLOS scenario, the contribution of each link (personnel devices/plane waves) can be simplified to the average of its associated distribution.

As regards the exposure at 900 MHz, the results show that the total exposure induced at 900 MHz is largely dominated by the mobile phone radiation. This is partly due to the fact that the measured power R_x is relatively low.

On the other side, three exposure cases have been observed with the tablet at 1940 MHz. In fact, we show that the levels of the local/global exposure are largely due to the downlink radiation, particularly when the T_x power is below 40 dB. Near this value, the resulting exposure is shared equally between the two paths. By increasing the T_x power, the contribution of the tablet becomes significant.

7. Summary and Conclusions

This paper addresses the evaluation of both global and local radio wave exposure induced by a wireless network, based on FDTD simulations, on a simplified model of the propagation and on measurements. Beyond the sole examination of a few exposure configurations, it highlights that suitable methodological approaches as well as statistical techniques allow characterizing the variability of exposure, in relation to the characteristics of the radio channel. In the case of an exposure to a personal device, the use of a statistical propagation channel combined with shadowing effects induced by the user proximity allowed us to characterize the variability of the input antenna power as well as the resulting exposure. The results obtained showed that both quantities are log-normally distributed, regardless of the propagation scenario. Concerning the exposure induced by a superposition of plane waves, the application of metamodeling to the exposure via the CP method allowed consolidating the validity of the obtained statistical distributions with a limited number of realizations, namely, of greedy FDTD simulations. Even though the total exposure is often dominated by either uplink or downlink, we found out that the local exposure requires taking care of both radiation sources, especially in cases for which the difference is not enormous. Future studies will focus on the analysis of the exposure induced by other anatomical models, including babies and a pregnant women, under various propagation scenarios (in car, at smart home, femtocell, and so on).

Conflicts of Interest

The authors declare that they have no conflicts of interest.

References

- [1] P. Gajšek, P. Ravazzani, J. Wiart, J. Grellier, T. Samaras, and G. Thuróczy, "Electromagnetic field exposure assessment in Europe radiofrequency fields (10 MHz–6 GHz)," *Journal of Exposure Science and Environmental Epidemiology*, vol. 25, pp. 37–44, 2013.
- [2] M. A. Jensen, "Application of FDTD and RGFM to EM interaction with biological tissue: a comparison," in *Proceedings of the IEEE Antennas and Propagation Society International Symposium*, vol. 4, pp. 1972–1975, Atlanta, Ga, USA, 1998.
- [3] S. Tabbane, *Handbook of Mobile Radio Networks*, Artech House Publishers, London, UK, 2000.
- [4] W. A. Shittu, B. G. Bajoga, F. Anwar, and M. J. E. Salami, "Prediction of received signal power and propagation path loss in open/rural environments using modified free-space loss and Hata models," in *Proceedings of the IEEE International RF and Microwave Conference (RFM '08)*, pp. 126–130, Kuala Lumpur, Malaysia, December 2008.
- [5] A. Sibille, "Statistical modeling of the radio-electric properties of wireless terminals in their environment," *IEEE Antennas and Propagation Magazine*, vol. 54, no. 6, pp. 117–129, 2012.
- [6] Z. Wang, X. Chen, and C. G. Parini, "Effects of the ground and the human body on the performance of a handset antenna," *IEE Proceedings: Microwaves, Antennas and Propagation*, vol. 151, no. 2, pp. 131–134, 2004.
- [7] Z. Wang, X. Chen, and G. C. Parini, "Body channel characterisation using dual band button antennas," *Antennas and Propagation*, pp. 958–961, 2009.
- [8] M. A. Stuchly, A. Kraszewski, and S. S. Stuchly, "Exposure of human models in the near and far field—a comparison," *IEEE Transactions on Biomedical Engineering*, vol. 32, no. 8, pp. 609–616, 1985.
- [9] O. Lauer, P. Frei, M.-C. Gosselin, W. Joseph, M. Röösli, and J. Fröhlich, "Combining near- and far-field exposure for an organ-specific and whole-body RF-EMF proxy for epidemiological research: a reference case," *Bioelectromagnetics*, vol. 34, no. 5, pp. 366–374, 2013.
- [10] EU FP7 LEXNET (low EMF exposure future networks) project, <http://www.lexnet-project.eu/>.
- [11] G. Blatman and B. Sudret, "Adaptive sparse polynomial chaos expansion based on least angle regression," *Journal of Computational Physics*, vol. 230, no. 6, pp. 2345–2367, 2011.
- [12] D. Plets, W. Joseph, K. Vanhecke et al., "Joint minimization of uplink and downlink whole-body exposure dose in indoor wireless networks," *BioMed Research International*, vol. 2015, Article ID 943415, 2015.
- [13] M. Tesanovic, E. Conil, A. De Domenico et al., "The LEXNET project: wireless networks and EMF: paving the way for low-EMF networks of the future," *IEEE Vehicular Technology Magazine*, vol. 9, no. 2, pp. 20–28, 2014.
- [14] J. Liu, D. Wang, J. Wang et al., "Uplink power control and interference coordination for heterogeneous network," in *Proceedings of the IEEE 23rd International Symposium on Personal, Indoor and Mobile Radio Communications (PIMRC '12)*, pp. 519–523, Sydney, Australia, September 2012.
- [15] A. Sibille, "Taking into account variability in wireless communication devices performance," in *Proceedings of the 1st URSI Atlantic Radio Science Conference (URSI AT-RASC '15)*, Las Palmas, Spain, May 2015.

- [16] P. Kysti, "WINNER II channel models," IST-4-027756 WINNER II Deliverable D1.1.2, V1.2.4.2, 2008, http://projects.celtic-initiative.org/winner+/phase_2_model.html.
- [17] A. Krayni, A. Hadjem, A. Sibille, C. Roblin, and J. Wiart, "A novel methodology to evaluate uplink exposure by personal devices in wireless networks," *IEEE Transactions on Electromagnetic Compatibility*, vol. 58, no. 3, pp. 896–906, 2016.
- [18] A. Thielens, G. Vermeeren, W. Joseph, and L. Martens, "Stochastic method for determination of the organ-specific averaged SAR in realistic environments at 950 MHz," *Bioelectromagnetics*, vol. 34, no. 7, pp. 549–562, 2013.
- [19] A. Christ, W. Kainz, E. G. Hahn et al., "The virtual family—development of surface-based anatomical models of two adults and two children for dosimetric simulations," *Physics in Medicine and Biology*, vol. 55, no. 2, pp. N23–N38, 2009.
- [20] IMST GmbH, *User and Reference Manual for the 3D EM Time Domain Simulator*, Empire, 2004, <http://www.empire.de/page11.html>.
- [21] C. Gabriel, "Compilation of the dielectric properties of body tissues at RF and microwave frequencies, Brooks Air Force Base," Tech. Rep. AL/OE-TR-1996-0037, Brooks Air Force Base, Brooks, Tex, USA, 1996.
- [22] S. Benkler, N. Chavannes, and N. Kuster, "New powerful FDTD source based on huygens surface: highly complex EM simulations performed on an ordinary PC," in *Proceedings of the 31th Annu. Meeting Bioelectromagn. Soc.*, vol. 2009, pp. 14–19, Davos, Switzerland.
- [23] ICNIRP, "Guidelines for limiting exposure to time-varying electric, magnetic and electromagnetic fields (up to 200 GHz)," *Health Physics*, vol. 74, no. 4, pp. 494–522, 1998.
- [24] E. Conil, A. Hadjem, A. Gati, M.-F. Wong, and J. Wiart, "Influence of plane-wave incidence angle on whole body and local exposure at 2100 MHz," *IEEE Transactions on Electromagnetic Compatibility*, vol. 53, no. 1, pp. 48–52, 2011.
- [25] R. P. Findlay and P. J. Dimbylow, "Effects of posture on FDTD calculations of specific absorption rate in a voxel model of the human body," *Physics in Medicine and Biology*, vol. 50, no. 16, pp. 3825–3835, 2005.
- [26] A. Hirata, N. Ito, and O. Fujiwara, "Influence of electromagnetic polarization on the whole-body averaged SAR in children for plane-wave exposures," *Physics in Medicine and Biology*, vol. 54, no. 4, pp. N59–65, 2009.
- [27] T. Kientega, E. Conil, A. Hadjem et al., "A surrogate model to assess the whole body SAR induced by multiple plane waves at 2.4 GHz," *Annals of Telecommunications*, vol. 66, no. 7, pp. 419–428, 2011.
- [28] G. Vermeeren, W. Joseph, and L. Martens, "Statistical multi-path exposure method for assessing the whole-body SAR in a heterogeneous human body model in a realistic environment," *Bioelectromagnetics*, vol. 34, no. 3, pp. 240–251, 2013.
- [29] M. D. McKay, R. J. Beckman, and W. J. Conover, "A comparison of three methods for selecting values of input variables in the analysis of output from a computer code," *Technometrics*, vol. 21, no. 2, pp. 239–245, 1979.
- [30] T. Kientega, E. Conil, A. Gati et al., "Analysis of the distribution of specific absorption rate induced by five plane waves with a fast and new method in visible human," in *Proceedings of the 30th URSI General Assembly and Scientific Symposium (URSIGASS '11)*, Istanbul, Turkey, August 2011.
- [31] P. Refaeilzadeh, L. Tang, and H. Liu, "Cross validation," in *Encyclopedia of Database Systems*, pp. 532–538, Springer, New York, NY, USA, 2009.
- [32] A. Gati, E. Conil, M.-F. Wong, and J. Wiart, "Duality between uplink local and downlink whole-body exposures in operating networks," *IEEE Transactions on Electromagnetic Compatibility*, vol. 52, no. 4, pp. 829–836, 2010.